nature metabolism

Article

https://doi.org/10.1038/s42255-024-01121-9

Organization of a functional glycolytic metabolon on mitochondria for metabolic efficiency

Received: 15 September 2023

Accepted: 2 August 2024

Haoming Wang[1], **John W. Vant**[2], **Andrew Zhang**[1], **Richard G. Sanchez**[1], **Youjun Wu**[3], **Mary L. Micou**[1,8], **Vincent Luczak**[1,9], **Zachary Whiddon**[1], **Natasha M. Carlson**[1], **Seungyoon B. Yu**[1,10], **Mirna Jabbo**[1], **Seokjun Yoon**[1,11], **Ahmed A. Abushawish**[1], **Majid Ghassemian**[4], **Takeya Masubuchi**[5], **Quan Gan**[6], **Shigeki Watanabe**[6], **Eric R. Griffis**[7,12], **Marc Hammarlund**[3], **Abhishek Singharoy**[2] & **Gulcin Pekkurnaz**[1] ✉

Glucose, the primary cellular energy source, is metabolized through glycolysis initiated by the rate-limiting enzyme hexokinase (HK). In energy-demanding tissues like the brain, HK1 is the dominant isoform, primarily localized on mitochondria, and is crucial for efficient glycolysis–oxidative phosphorylation coupling and optimal energy generation. This study unveils a unique mechanism regulating HK1 activity, glycolysis and the dynamics of mitochondrial coupling, mediated by the metabolic sensor enzyme O-GlcNAc transferase (OGT). OGT catalyses reversible O-GlcNAcylation, a post-translational modification influenced by glucose flux. Elevated OGT activity induces dynamic O-GlcNAcylation of the regulatory domain of HK1, subsequently promoting the assembly of the glycolytic metabolon on the outer mitochondrial membrane. This modification enhances the mitochondrial association with HK1, orchestrating glycolytic and mitochondrial ATP production. Mutation in HK1's O-GlcNAcylation site reduces ATP generation in multiple cell types, specifically affecting metabolic efficiency in neurons. This study reveals a previously unappreciated pathway that links neuronal metabolism and mitochondrial function through OGT and the formation of the glycolytic metabolon, providing potential strategies for tackling metabolic and neurological disorders.

In cellular environments, metabolic reactions are more complex than a simple cascade of enzymes and metabolites operating within diffusion limits. Rather, an advanced level of organization leverages the compartmentalization of metabolic enzymes to organelles such as mitochondria and other subcellular structures to optimize biochemical transformations[1–5]. This complex spatial organization, often referred to as a 'metabolon', delineates the physical boundaries of metabolic fluxes within the cytoplasm[4,6,7]. Metabolons enhance metabolic efficiency by co-compartmentalizing enzymes with their sequential substrates, thereby minimizing diffusional transit times, promoting metabolite channelling, providing an optimized microenvironment for individual pathways and limiting counterproductive metabolite–enzyme interactions. Despite the pivotal role of this spatial organization in ensuring efficient substrate channelling and metabolic flux regulation, our mechanistic insight into the regulation of metabolon formation, particularly within key metabolic pathways like glycolysis, remains sparse[8,9].

A full list of affiliations appears at the end of the paper. ✉e-mail: gpekkurnaz@ucsd.edu

Glycolysis mediates the conversion of glucose to pyruvate, which is then further metabolized to generate ATP. A key enzyme in this process is hexokinase (HK), which catalyses the initial, rate-limiting step of phosphorylating glucose into glucose-6-phosphate (G6P). Importantly, this step consumes ATP. Hexokinase 1 (HK1), one of the distinct isoforms of HK expressed in metabolically demanding cells such as neurons, is predominantly localized on the outer mitochondrial membrane[10–12]. This subcellular proximity to mitochondria implies a role for HK1 in modulating metabolic efficiency[13]. Although previous studies have explored the role of HK1 in glycolysis, the specific molecular pathway that dictates HK1 activity, its mitochondrial localization and its potential involvement in the glycolytic metabolon assembly remains elusive.

This study investigates a molecular mechanism that modulates the activity and mitochondrial localization of HK1 through the action of the metabolic sensor enzyme O-GlcNAc transferase (OGT). OGT catalyses a unique post-translational modification, O-GlcNAcylation, by attaching a GlcNAc sugar moiety to serine and threonine residues on proteins. Intracellular UDP-GlcNAc concentrations, modulated by glucose flux through the hexosamine biosynthetic pathway, regulate this process[14–16]. Our findings reveal that HK1 undergoes dynamic O-GlcNAcylation at its regulatory domain when OGT activity is elevated. This modification enhances the localization of HK1 to the mitochondria, leading to increased rates of both glycolytic and mitochondrial ATP production. This is achieved by facilitating the formation of a glycolytic metabolon on the mitochondrial outer membrane. By contrast, mutations at the O-GlcNAcylation site of HK1 result in reduced ATP production rates and dysregulation of the energy-demanding process of presynaptic vesicle recycling in neurons. In summary, our study uncovers a previously unappreciated molecular pathway linking neuronal metabolism to mitochondrial function through OGT-mediated modulation of HK1. We identify HK1 O-GlcNAcylation as a fundamental mechanism regulating glycolysis and metabolon formation that is critical for metabolic efficiency, offering potential implications for the development of targeted interventions for metabolic and neurological disorders.

Results

Glucose modulates mitochondrial localization of HK1

To characterize HK1 localization at the subcellular level, we carried out immunofluorescence analysis in disassociated rat hippocampal neurons. Using hippocampal neurons transfected with Mito-DsRed as a mitochondrial marker, we observed that over 80% of endogenous HK1 resided alongside mitochondria within the soma, dendrites and axon (Fig. 1a), as previously reported[17].

Given that glucose serves as the substrate for HK1, and glucose phosphorylation consumes ATP, coupled with the fact that mitochondria are ATP-rich and mitochondrial oxidative phosphorylation depends on ADP, we reasoned that glucose flux could be a key regulator of the mitochondrial positioning of HK1 (Fig. 1b). To test the effect of glucose flux on HK1 positioning, we cultured primary neurons in media containing 5 mM glucose. These neurons were then subjected to a 72 h glucose reduction to 1 mM, followed by a subsequent increase back to 5 mM before imaging (Extended Data Fig. 1a)[18]. We also established a system for live imaging of HK1 and mitochondria using neurons co-expressing Mito-DsRed and short hairpin RNA (shRNA)-resistant HK1–GFP, together with a shRNA designed to deplete endogenous HK1. The efficacy of this shRNA had already been validated in Neuro-2a cells (Extended Data Fig. 1b,c). By using this approach, we ensured that the HK1 level remained consistent with endogenous levels (Extended Data Fig. 1c, and as detailed in Extended Data Fig. 4f,g). Our results revealed a direct response to glucose flux: an increase in extracellular glucose prompted mitochondrial enrichment of HK1 in neurons (Fig. 1b–e). To further examine the role of glucose flux, we subjected the neurons to a 2 h glucose-deprivation period followed by an immediate reintroduction of glucose to 5 mM before imaging (Extended Data Fig. 1d–f). Pyruvate (1 mM) was present throughout these experiments as an alternate fuel source. Remarkably, a transient decrease in extracellular glucose led to the downregulation of mitochondrial HK1. However, upon reintroduction of glucose to 5 mM, we observed rebound recruitment of HK1 to the mitochondria within the same neuron (Extended Data Fig. 1d–f). Under physiological conditions, extracellular glucose concentration in the mammalian brain ranges from 2–5 mM glucose[19]. Instead of complete glucose deprivation, we cultured neurons for 2 h in 2 mM glucose and then immediately restored glucose to 5 mM. This resulted in a similar enrichment of mitochondrial HK1 (Extended Data Fig. 1g,h).

Feeding state influences HK1 positioning in vivo

Expanding our investigation in vivo, we performed feeding and fasting experiments with mice (Fig. 1f–h). We confirmed that fluctuations in blood glucose levels mirrored the feeding cycles, as previously reported[18]. Mice subjected to 24 h fasting exhibited a drop in blood glucose, which normalized upon a subsequent 24 h feeding period (Extended Data Fig. 1i). Upon examining HK1 localization within the CA3 region of the hippocampus in ad libitum fed, fasted and refed mice, we found a clear correlation with blood glucose levels (Fig. 1f–i). Fasting, and the consequent drop in blood glucose, resulted in a downregulation of mitochondrial HK1. These patterns of mitochondrial HK1 downregulation were consistently observed under both 24 h (Fig. 1i) and 6 h fasting conditions (Extended Data Fig. 1j,k). By contrast, refeeding, and the subsequent rise in blood glucose, led to an upregulation of mitochondrial HK1 compared to ad libitum conditions (Fig. 1i). Importantly, neither feeding nor fasting altered overall HK1 expression levels (Fig. 1i).

OGT promotes HK1 recruitment to mitochondria

The hexosamine biosynthetic pathway integrates glucose flux signals, culminating in the production of UDP-GlcNAc, an essential substrate

Fig. 1 | Glucose-dependent regulation of HK1 localization. **a**, Immunofluorescence staining of hippocampal neurons for endogenous HK1 (green) and mitochondria (Mito-DsRed; grey), illustrating subcellular localization of HK1 in the somatodendritic region, axon and dendrites (three independent experiments). **b**, Hippocampal neurons cultured in 5 mM glucose, expressing Mito-DsRed (grey), WT human HK1 tagged with eGFP and rat shRNA-HK1 to achieve an endogenous level of HK1 (pseudocolour, fire), then transferred to 1 mM glucose for 72 h. **c**, Representative axonal images following a 2 h exposure to 5 mM glucose or at 1 mM glucose, as in **b**. Scale bar, 5 µm; pseudocolour scale indicates low to high intensity. **d**, Quantification of mitochondrial (Mito) and cytoplasmic (Cyto) HK1 intensity ratios along axons. Data are presented as a violin plot with individual data points and associated *P* value. $n = 102–117$ mitochondria, 9–10 axons from three independent experiments (unpaired two-tailed *t*-test). **e**, Spatiotemporal changes of HK1 measured by live-cell imaging for 10 min along the axon within cytoplasmic (Cyto; blue intensity plot) and mitochondrial (Mito; orange intensity plot) compartments during a medium switch from 1 to 1 mM or 5 mM glucose. Scale bar, 2 µm. **f**, Immunofluorescence staining of mouse brain coronal slices (−2 mm from bregma) with antibodies against HK1 (pseudocolour, fire), mitochondrial marker pyruvate dehydrogenase (PDH; grey) and neuronal marker NeuN (green). The hippocampal section in the ad libitum fed state. Scale bar, 100 µm. **g**, Enlarged images of white dashed boxes in **f**, displaying the HK1 distribution in the CA3 region of the hippocampus in ad libitum, fasted and refed states. Scale bar, 10 µm. **h**, Schematic illustration of the experiment for altering blood glucose levels through fasting and refeeding in mice, used to compare HK1 localization in the brain. **i**, Co-localization analysis to measure the per cent intensity of HK1 on mitochondria and mitochondrial HK1, the Pearson's correlation coefficient (*R*-value) and quantification of HK1 level for each condition. Data are presented as violin plots with individual data points and associated *P* values; $n = 3$ mice and biological replica per condition (one-way ANOVA with post hoc Holm–Šídák's multiple comparison test). See also Extended Data Fig. 1.

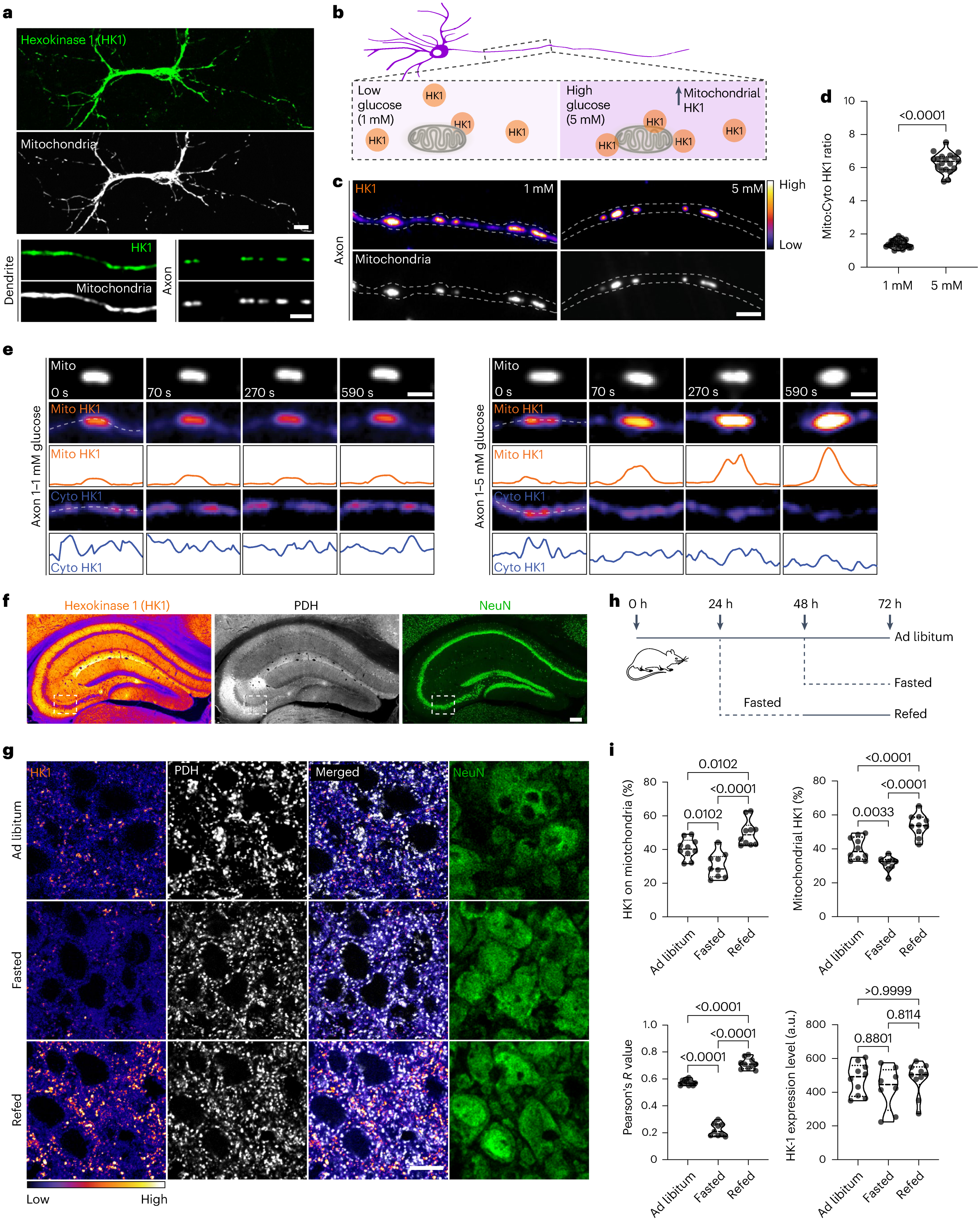
a
Hexokinase 1 (HK1)
Mitochondria
Dendrite
HK1
Mitochondria
Axon
b
Low glucose (1 mM)
HK1
High glucose (5 mM)
↑Mitochondrial HK1
c
HK1
1 mM
5 mM
High
Low
Axon
Mitochondria
d
Mito:Cyto HK1 ratio
<0.0001
0
2
4
6
8
10
1 mM
5 mM
e
Mito
0 s
70 s
270 s
590 s
Mito HK1
Cyto HK1
Axon 1–1 mM glucose
Axon 1–5 mM glucose
f
Hexokinase 1 (HK1)
PDH
NeuN
g
HK1
PDH
Merged
NeuN
Ad libitum
Fasted
Refed
Low
High
h
0 h
24 h
48 h
72 h
Ad libitum
Fasted
Fasted
Refed
i
HK1 on miotchondria (%)
0.0102
<0.0001
0.0102
Mitochondrial HK1 (%)
<0.0001
<0.0001
0.0033
Pearson's R value
<0.0001
<0.0001
<0.0001
HK-1 expression level (a.u.)
>0.9999
0.8114
0.8801
Ad libitum
Fasted
Refed

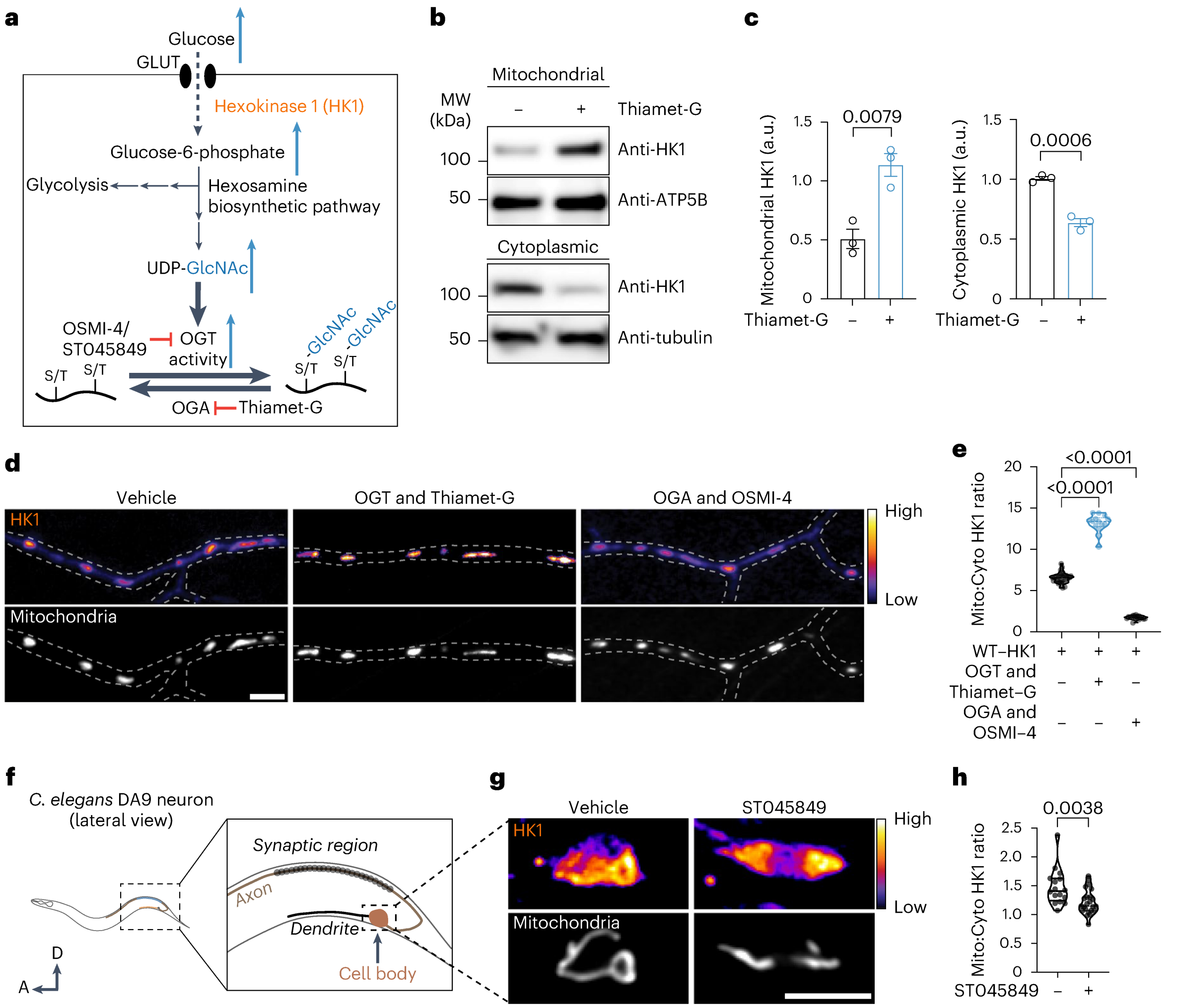

Fig. 2 | O-GlcNAcylation regulates mitochondrial localization of HK1. **a**, Schematic representation of glucose metabolism via the hexosamine biosynthetic pathway. Rate-limiting steps and inhibitors used in this study are also indicated. Increased glucose flux upregulates the hexosamine biosynthetic pathway, UDP-GlcNAc synthesis and OGT activity. **b**, Mitochondrial and cytoplasmic fractions, obtained from rat cortical neurons treated overnight with OGA inhibitor Thiamet-G to enrich neuronal O-GlcNAcylation or vehicle (DMSO), were separated by SDS gel electrophoresis and probed with anti-HK1, anti-ATP5B (mitochondrial marker) and anti-tubulin (cytoplasmic marker). **c**, Quantification of HK1 bands normalized to the intensity of ATP5B (mitochondrial fraction) or tubulin (cytoplasmic fraction) for each condition. *n* = 3 independent experiments (all values are shown as mean ± s.e.m.; unpaired two-tailed *t*-test). **d**, Manipulating O-GlcNAcylation affects HK1 localization in neurons. Axonal segments of hippocampal neurons cultured in 5 mM glucose, co-transfected with Mito-DsRed (grey), rat shRNA-HK1 and WT human HK1 tagged with eGFP (pseudocolour, fire) to achieve endogenous expression level of HK1. O-GlcNAcylation level was upregulated by ectopic expression of OGT and Thiamet-G treatment, and downregulated by expression of OGA and OSMI-4 treatment. Scale bar, 5 μm. **e**, Quantification of mitochondrial (Mito) and cytoplasmic (Cyto) HK1 intensity ratios along axons. Data are presented as a violin plot with individual data points and associated *P* values; *n* = 83–120 mitochondria from 11–13 axons across conditions, three independent experiments (one-way ANOVA with post hoc Tukey's multiple comparison test). **f**–**h**, In vivo imaging of endogenously GFP-tagged HK1 in *C. elegans* neurons. **f**, Schematic representation of the DA9 neuron cell body in *C. elegans* nervous system. **g**, DA9 neurons expressing (hxk-1) HK1-7xSplitGFP (pseudocolour, fire) and mito-TagRFP (grey) following vehicle (DMSO) or OGT inhibitor ST045849 treatments. Scale bar, 5 μm. **h**, Mitochondrial and cytoplasmic HK1-7xSplitGFP ratios were quantified from DA9 neuron cell bodies for each condition. Data are presented as a violin plot with individual data points and associated *P* values; *n* = 16–23 cell bodies, three independent experiments (unpaired two-tailed *t*-test). See also Extended Data Fig. 2.

for O-GlcNAcylation. Acting as a metabolic sensor that reflects the nutritional status of the cell, this pathway dynamically regulates O-GlcNAc addition by OGT. This addition is counterbalanced by its removal through the enzyme O-GlcNAcase (OGA) (Fig. 2a). Given the previously recognized role of the pathway in mitochondrial anchoring, we reasoned that OGT and OGA might collaboratively dictate the positioning of HK1 on the mitochondria in response to glucose flux changes to enhance metabolic efficiency[18,20]. To determine whether OGT and OGA activity influences HK1 localization in hippocampal neurons, we pharmacologically and genetically manipulated this enzyme pair and modulated O-GlcNAcylation levels (Extended Data Fig. 2a–c). Both biochemical analysis of mitochondrial fractions (Fig. 2b,c) and imaging data suggested (Fig. 2d,e) that enhancing O-GlcNAcylation increased mitochondrial HK1, whereas reducing O-GlcNAcylation decreased mitochondrial HK1 in neurons. Glucose flux-dependent recruitment of HK1 to mitochondria was also diminished in the presence of an OGT inhibitor (Extended Data Fig. 1g,h). Importantly, mitochondrial size remained unaffected by O-GlcNAcylation level fluctuations (Extended Data Fig. 2b). This phenotype was also observed in HEK293T cells, a cell type expressing HK1 as the predominant HK isoform, further confirming our findings (Extended Data Fig. 2d,e).

OGT modulates HK1 positioning in vivo in *Caenorhabditis elegans*

Building on our findings that O-GlcNAcylation has a key role in controlling the mitochondrial localization of HK1 in mammalian cells, we expanded our inquiry to *Caenorhabditis elegans*. Given the conservation of OGT and HK1 in *C. elegans*, we investigated whether O-GlcNAcylation could regulate HK1 positioning in vivo. We engineered *C. elegans* to express HK1 endogenously tagged with 7xSplitGFP in the DA9 neuron (Extended Data Fig. 2f). To attenuate O-GlcNAcylation without overexpressing OGA, we treated the nematodes with an OGT inhibitor (ST045849) that was previously validated specifically in *C. elegans*[21]. Upon imaging the cell body of the DA9 neuron (Fig. 2f), we observed that a reduction in O-GlcNAcylation corresponded to a decrease in mitochondrial HK1 (Fig. 2g,h). These in vivo observations parallel the outcomes seen with OSMI-4 treatments in cultured rodent hippocampal neurons, highlighting the conserved role of O-GlcNAcylation in regulating HK1 positioning across different genera.

HK1 undergoes regulated O-GlcNAcylation

To elucidate whether HK1 is regulated by O-GlcNAcylation directly, we used a CRISPR-based strategy to add a GFP tag to the carboxyl terminus of endogenous HK1 in HEK293T cells (Extended Data Fig. 3a), a tagging strategy known not to hinder HK1 function[17]. We then used immunoprecipitation to isolate HK1 from these genetically engineered cells and resolved proteins on an SDS–PAGE gel (Fig. 3a,b and Extended Data Fig. 3b). To determine whether the extent of HK1 O-GlcNAcylation was susceptible to changes in OGT and OGA activity, we upregulated OGT activity by ectopic expression and applied the OGA inhibitor Thiamet-G. Anti-GlcNAc antibodies detected a band co-migrating with HK1 in anti-GFP immunoprecipitation from the CRISPR-modified HEK293T cells (Fig. 3a). The intensity of the band was amplified when OGT was overexpressed and OGA was concurrently inhibited (Fig. 3a,b). Furthermore, we performed immunoprecipitation on O-GlcNAcylated mitochondrial proteins from rat cortical neurons and compared the samples with and without Thiamet-G-induced OGA inhibition (Extended Data Fig. 3c,d). Significant amplification of O-GlcNAcylated mitochondrial HK1 was observed upon OGA inhibition (Extended Data Fig. 3d) in neurons, suggesting that under basal conditions, the O-GlcNAcylation sites of HK1 are not saturated, and the modification level is probably determined by the dynamic equilibrium between OGT and OGA activity. Overnight inhibition of OGT or OGA activities resulted in an approximately 50% alteration in total neuronal O-GlcNAcylation (Extended Data Fig. 3e,f). We extended our investigation to hexokinase 2 (HK2), examining its O-GlcNAcylation cycling status. Despite the detection of an O-GlcNAcylated HK2 band in anti-GFP immunoprecipitants from HEK293T cells (Extended Data Fig. 3e,f), the intensity of this band did not increase upon Thiamet-G-mediated OGA inhibition or OGT overexpression (Extended Data Fig. 3e,f). These results imply that although HK2 is subject to baseline O-GlcNAcylation, the extent of this modification is unaffected by alterations in OGT or OGA activity.

Nanobody-mediated control HK1 localization

To investigate the role of HK1 O-GlcNAcylation in determining its subcellular localization, we adopted an approach to selectively attenuate HK1 O-GlcNAcylation. In COS-7 cells, we co-expressed GFP-tagged HK1 along with a GFP-nanobody-fused, split O-GlcNAcase (nGFP–OGA)[22–24] (Fig. 3c). The enzymatic activity of OGA was only present when both myc–OGA(1–400) and nGFP–HA–OGA(544–706) were concurrently expressed (Fig. 3c,d). To ensure consistency, we confirmed that the expression levels of split OGA plasmids and HK1 were equal across conditions (Extended Data Fig. 3i–k). Following cell fixation, we performed staining of Tomm20, a protein that serves as a mitochondrial marker (Fig. 3d). The targeted reduction of HK1 O-GlcNAcylation led to a decrease in mitochondrial HK1 within COS-7 cells (Fig. 3d–g). Our findings, therefore, highlight that the level of HK1 O-GlcNAcylation modulates its mitochondrial localization in both neurons and COS-7 cells.

Identification of O-GlcNAcylation site in HK1

To elucidate the presence and location of O-GlcNAcylation sites within HK1, we used immunoprecipitation to isolate this protein from HEK293T cells. The cells were subjected to both basal and enhanced O-GlcNAcylation conditions. The resulting HK1 protein was then resolved on an SDS–PAGE gel and probed with anti-GlcNAc antibodies. This process confirmed that HK1 O-GlcNAcylation levels indeed rise in response to an upregulated O-GlcNAcylation environment (Fig. 4a,b). Proteins with a molecular weight approximating that of HK1 were subsequently extracted from the SDS–PAGE gel. Peptides were isolated from these proteins through trypsin and gluC co-digestion and subsequently analysed using tandem mass spectrometry. This in-depth analysis yielded the identification of a single O-GlcNAc modification site within HK1 (Extended Data Fig. 4a). Notably, the site of this modification, T259, is unique to HK1 among the three HK isoforms. It is, however, conserved across most mammalian HK1 and *C. elegans* (Fig. 4c). This finding underscores the potentially critical role of O-GlcNAcylation at T259 in the functionality of HK1.

Having established the specific O-GlcNAc modification site within HK1, we next sought to understand how this modification might influence the structural conformation of the protein. To determine the effect of T259 O-GlcNAcylation on the structure of HK1, we turned to computational modelling (Fig. 4d). The HK1 structure is composed of amino-terminal and carboxyl-terminal halves: the N-terminal half is the regulatory domain, while the C-terminal half exhibits catalytic activity, participating in glucose binding and glucose phosphorylation via ATP. When G6P binds at the N-terminus of HK1, it impedes the interaction of HK1 with mitochondria, creating a negative feedback loop. A linker region joining the two halves is primarily composed of a 28-residue-long (residues 448–476) alpha helix[25]. This linker region is implicated in regulating the coupling between the G6P-occupancy of the N-terminal with the glucose reactivity of the C-terminal half[25] by perturbing the C-terminal binding pocket through a network of allosteric interactions and altering the conformation of the catalytic binding pocket to favour the binding of G6P over ATP. However, little has been reported on the relevance of N-terminal G6P binding to mitochondrial membrane–HK interactions. Interestingly, the T259 O-GlcNAcylation residue is located near the non-catalytic N-terminal pocket. Through Resolution Exchange Solute Tempering (REST2) molecular dynamics simulations[26,27], we revealed a conformational transition state of the O-GlcNAc modified HK1, which results in a loss of secondary structure and a looser binding pocket than in the unmodified HK1 (Fig. 4d). At the site of O-GlcNAcylation, the single-turn alpha helix (residues 260–264) forms a flexible loop to accommodate the bulky O-GlcNAc. Additionally, key residues (Ser88, Thr232 and Ser415) responsible for coordinating the phosphate and the 2′ hydroxyl (Asp84, Asp413 and Ser449) of G6P are offered more significant conformational flexibility to accommodate the bulky O-GlcNAc moiety without disrupting packing of the pocket. This enhanced conformational freedom of the residues prevents a stable interaction with G6P. Thus, HK1 has a large-scale conformational rearrangement upon O-GlcNAcylation based on our computational modelling (Fig. 4d, right) with an N-terminal root mean squared deviation of 3.5 Å (aligned and calculated with Cα atoms in residues 20–460 using the crystal structure as a reference).

T259 O-GlcNAcylation directs HK1 to mitochondria

To elucidate the significance of T259 O-GlcNAcylation in regulating the mitochondrial localization of HK1, we used site-directed mutagenesis to substitute Thr259 with alanine, thereby abolishing O-GlcNAcylation at this specific residue. Subsequently, we expressed and immunoprecipitated both the wild-type (WT) HK1 and the O-GlcNAc-deficient

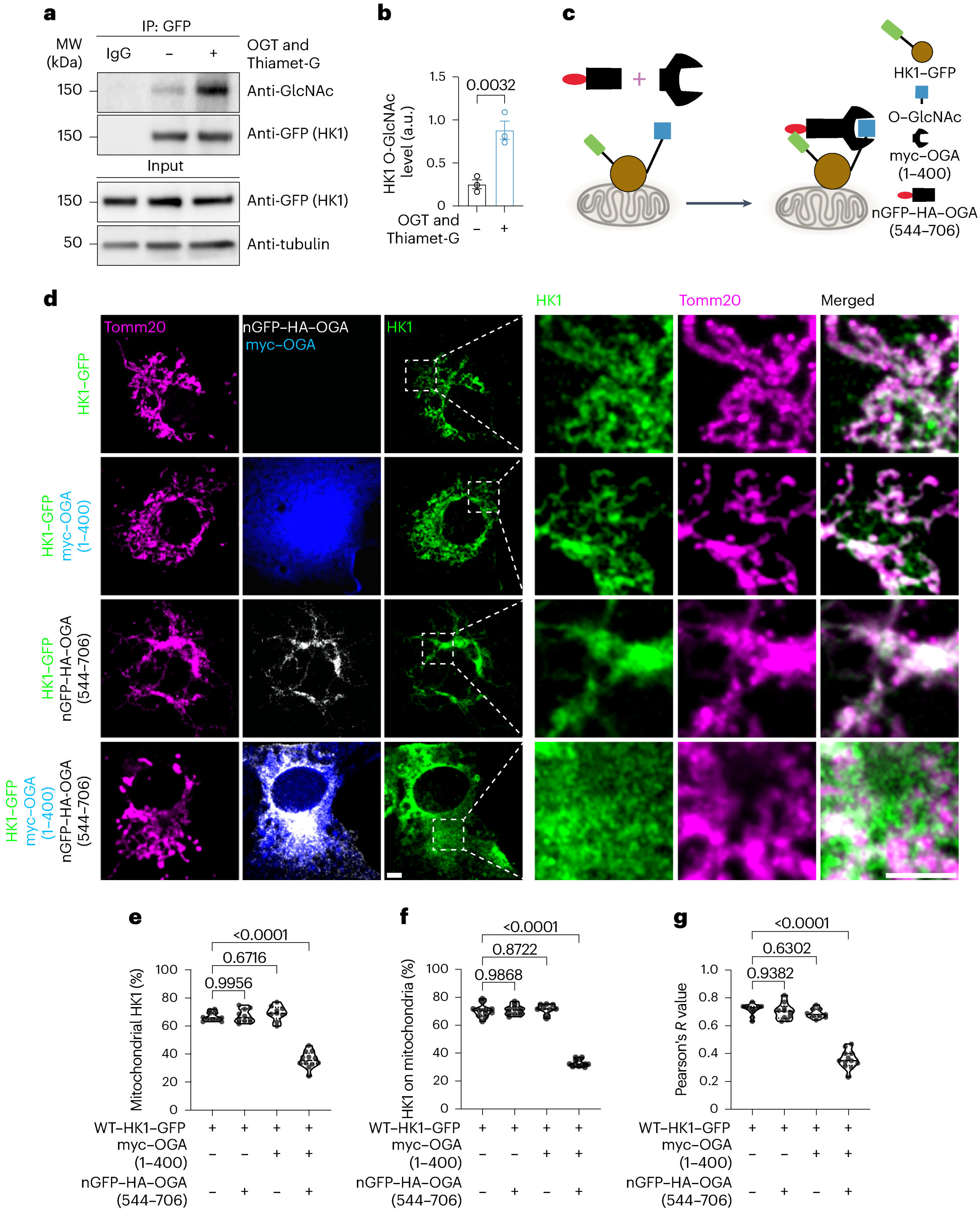

Fig. 3 | OGT and OGA regulate HK1 O-GlcNAcylation. a, The impact of O-GlcNAcylation upregulation on HK1, elicited by ectopic OGT expression and Thiamet-G treatment, was investigated using immunoprecipitation (IP) of endogenous HK1 from HEK293T-eGFP–HK1 cells (CRISPR-edited cells expressing endogenously eGFP-tagged HK1). HK1 was immunoprecipitated using an anti-GFP antibody from cells treated overnight with either vehicle (DMSO) or Thiamet-G, with or without OGT expression. Rabbit IgG served as a negative IP control. Input lanes, which were loaded with 3% of cell lysates used for IP, were also probed with an anti-tubulin antibody to confirm equal loading. **b**, HK1 O-GlcNAcylation was quantified by normalizing the intensity of each GlcNAc band to the corresponding HK1 (GFP) band. OGT overexpression resulted in a significant increase in HK1 O-GlcNAcylation. *n* = 3 independent experiments (mean ± s.e.m.; unpaired one-tailed *t*-test). **c**–**g**, Selective downregulation of HK1 O-GlcNAcylation by a nanobody-fused split OGA eraser and evaluation of subcellular localization. **c**, Schematic illustrating the approach to selectively downregulate HK1 O-GlcNAcylation using eGFP-tagged HK1 (HK1–GFP) and GFP-nanobody (nGFP)-directed split O-GlcNAc eraser (nGFP–HA–OGA(544–706) and myc–OGA(1–400). The OGA enzyme was engineered into a split and truncated form with limited substrate activity. nGFP–HA–OGA(544–706) recognizes HK1–GFP and redirects the catalytic half of OGA myc–OGA(1–400) to remove the O-GlcNAc modification from HK1. **d**, Representative images of COS-7 cells expressing HK1–GFP (green), myc–OGA(1–400) (blue) and nGFP–HA–OGA(544–706) (grey). The subcellular localization of HK1 was examined using immunofluorescence staining with anti-Tomm20 (mitochondrial marker; magenta), anti-myc (myc–OGA(1–400); blue) and anti-HA (nGFP–HA–OGA(544–706); grey) antibodies. The HK1 distribution pattern is highlighted in the enlarged images corresponding to the white dashed boxes in **d**. Scale bars, 5 µm. **e**–**g**, Quantitative analysis of HK1 co-localization to assess the percentage of mitochondrial HK1 intensity (**e**), HK1 intensity on mitochondria (**f**), and Pearson's correlation coefficient (*R*-value) for each condition (**g**). Data are presented as violin plots with individual data points and associated *P* values. *n* = 42 cells from three independent experiments (one-way ANOVA with post hoc Tukey's multiple comparison test). See also Extended Data Fig. 3.

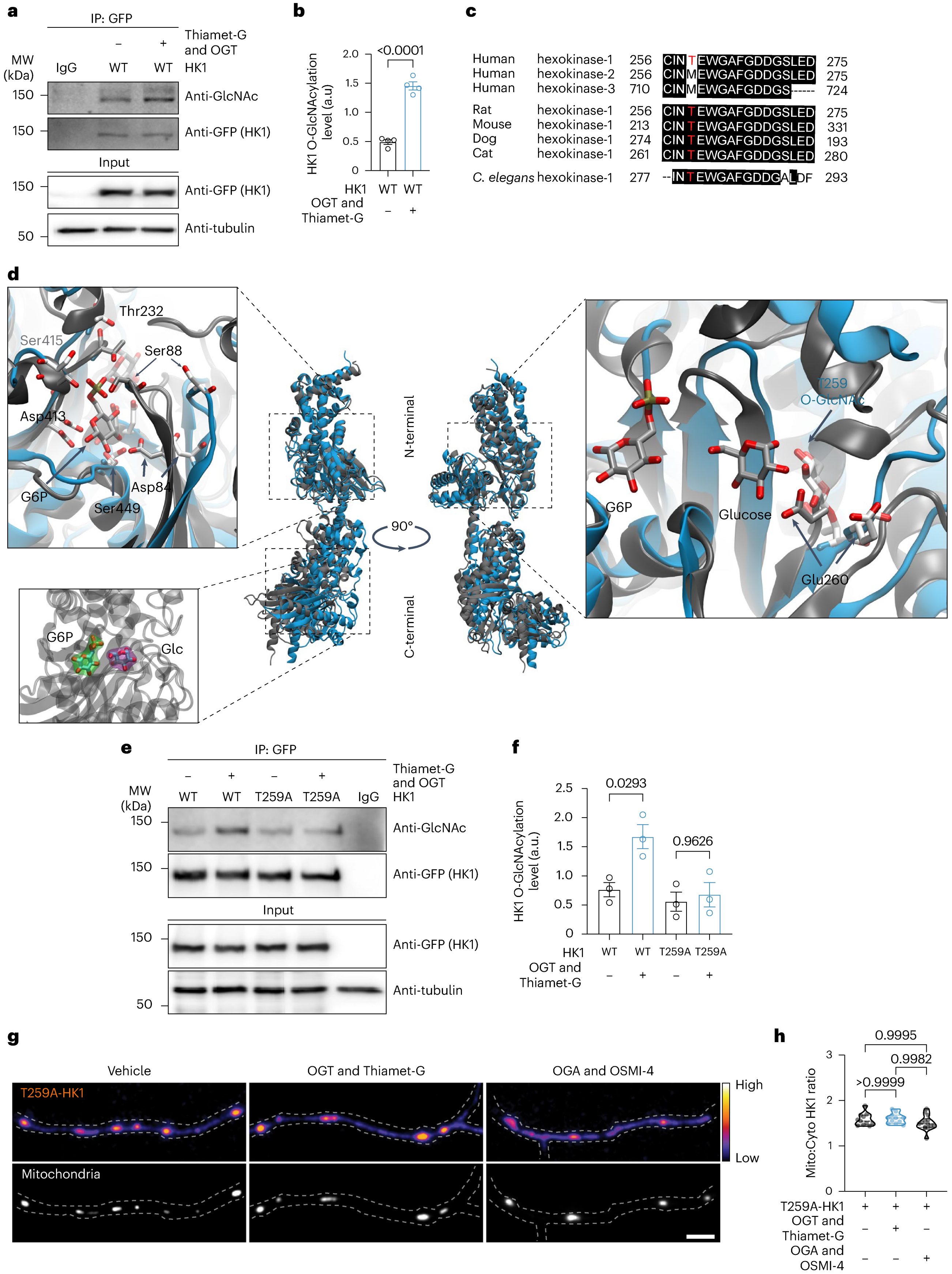
a
IP: GFP
Thiamet-G and OGT
–
+
MW (kDa)
IgG
WT
WT
HK1
150
Anti-GlcNAc
150
Anti-GFP (HK1)
Input
150
Anti-GFP (HK1)
50
Anti-tubulin
b
HK1 O-GlcNAcylation level (a.u)
<0.0001
2.0
1.5
1.0
0.5
0
HK1
WT
WT
OGT and Thiamet-G
–
+
c
Human hexokinase-1 256 CINTEWGAFGDDGSLED 275
Human hexokinase-2 256 CINMEWGAFGDDGSLED 275
Human hexokinase-3 710 CINMEWGAFGDDGS----- 724
Rat hexokinase-1 256 CINTEWGAFGDDGSLED 275
Mouse hexokinase-1 213 CINTEWGAFGDDGSLED 331
Dog hexokinase-1 274 CINTEWGAFGDDGSLED 193
Cat hexokinase-1 261 CINTEWGAFGDDGSLED 280
C. elegans hexokinase-1 277 --INTEWGAFGDDGALDF 293
d
Thr232
Ser415
Ser88
Asp413
G6P
Asp84
Ser449
G6P
Glc
N-terminal
C-terminal
90°
T259 O-GlcNAc
G6P
Glucose
Glu260
e
IP: GFP
Thiamet-G and OGT
–
+
–
+
MW (kDa)
WT
WT
T259A
T259A
IgG
HK1
150
Anti-GlcNAc
150
Anti-GFP (HK1)
Input
150
Anti-GFP (HK1)
50
Anti-tubulin
f
HK1 O-GlcNAcylation level (a.u.)
2.5
2.0
1.5
1.0
0.5
0
0.0293
0.9626
HK1
WT
WT
T259A
T259A
OGT and Thiamet-G
–
+
–
+
g
Vehicle
OGT and Thiamet-G
OGA and OSMI-4
T259A-HK1
Mitochondria
High
Low
h
Mito:Cyto HK1 ratio
3
2
1
0
0.9995
0.9982
>0.9999
T259A-HK1
+
+
+
OGT and Thiamet-G
–
+
–
OGA and OSMI-4
–
–
+

Fig. 4 | OGT-dependent regulation of HK1 localization requires O-GlcNAcylation. **a**–**f**, Characterization of HK1 O-GlcNAcylation. **a**, To identify the O-GlcNAc modification site, eGFP-tagged HK1 (with or without OGT or Thiamet-G) was overexpressed in HEK293T cells and immunoprecipitated. Input lanes contained 3% cell lysates used for IP. Anti-tubulin staining was used as a loading control. **b**, HK1 O-GlcNAcylation levels were quantified by normalizing the intensity of each GlcNAc band to the intensity of HK1–GFP bands (three biological replicas, mean ± s.e.m. and associated *P* values; unpaired one-tailed *t*-test). **c**, Human HK1 (amino acid residues 256–275) sequence alignment with different species. O-GlcNAcylated threonine (T) residue (red), conserved amino acids (black) and HK isoforms are also shown. **d**, Structural differences between the unmodified HK1 (grey) and O-GlcNAcylated HK1 (blue). The Cα atoms in residues 20–460 were used for alignment. Top left inset shows key residues coordinating the phosphate of G6P and the 2′ hydroxyl. Bottom left inset shows the binding pockets for G6P (green) and glucose (purple). Right inset shows T259-HK1 with O-GlcNAcylation; the single-turn alpha helix (residues 260–264) forms a flexible loop to accommodate the O-GlcNAc with the positions of G6P and glucose. **e**, Either WT or O-GlcNAc site mutated (T259A) HK1–GFP immunoprecipitated from HEK293T cells, with or without OGT or Thiamet-G, then analysed with anti-GlcNAc and anti-GFP antibodies to quantify HK1 GlcNAcylation levels. **f**, The intensity of each GlcNAc band was normalized to the GFP band for quantification of O-GlcNAcylation levels (three biological replicas, mean ± s.e.m. and associated *P* values; one-way ANOVA with post hoc Tukey's multiple comparison test). **g**,**h**, Hippocampal neurons cultured in 5 mM glucose, expressing Mito-DsRed (grey), rat shRNA-HK1 and T259A-HK1–GFP (pseudocolour, fire). O-GlcNAcylation levels were upregulated by OGT and Thiamet-G treatment and downregulated by OGA and OSMI-4 treatment. Scale bar, 5 µm. Mitochondrial (Mito) and cytoplasmic (Cyto) HK1 intensity ratios along axons. Data are presented as a violin plot with individual data points and associated *P* values. *n* = 81–86 mitochondria from 10–13 axons, three independent experiments (one-way ANOVA with post hoc Tukey's multiple comparison test). Scale bar, 5 µm. See also Extended Data Fig. 4.

T259A-HK1 variant from HEK239T cells. The immunoprecipitants were subjected to SDS–PAGE analysis and probed with anti-GlcNAc antibodies to validate the successful disruption of O-GlcNAcylation in the T259A-HK1 mutant (Fig. 4e,f). To investigate the impact of O-GlcNAcylation at T259 on HK1's mitochondrial localization, we conducted imaging experiments using HEK293T cells expressing either WT HK1 or the T259A-HK1 mutant, in conjunction with Mito-DsRed. To simulate conditions of heightened glucose flux, we used OGT overexpression and OGA inhibition using Thiamet-G. We observed a pronounced increase in the mitochondrial localization of WT HK1 (Extended Data Fig. 4b,c), whereas no such effect was observed in cells expressing the T259A-HK1 mutant (Extended Data Fig. 4d,e).

Expanding our investigation to hippocampal neurons, we expressed T259A-HK1–GFP using our shRNA approach (Extended Data Fig. 4f,g). By modulating O-GlcNAcylation levels through ectopic OGT expression and OGA inhibition or ectopic OGA expression and OGT inhibition using OSMI-4, we aimed to replicate conditions of increased or decreased glucose flux, respectively, as outlined in Extended Data Fig. 2c. Analysis of the mitochondrial to cytoplasmic HK1 ratio along the axon of the neuron revealed that the absence of O-GlcNAcylation at the T259 site rendered HK1's mitochondrial localization unresponsive to changes in O-GlcNAcylation levels (Fig. 4g,h and see also Fig. 2d,e for control conditions) without affecting mitochondrial size (Extended Data Fig. 4h).

HK1 O-GlcNAcylation alters ATP production rates

Mitochondrial binding allows HK1 to have prime access to mitochondrially generated ATP, thus promoting more effective glucose phosphorylation[28]. To investigate the role of O-GlcNAcylation in modulating HK1 activity, we measured the levels of G6P, which is the product of HK1-mediated glucose phosphorylation (Fig. 5a). We expressed WT HK1 or the T259A-HK1 in HEK239T cells and manipulated O-GlcNAcylation levels by the ectopic expression of OGT and inhibition of OGA using Thiamet-G. Our results revealed that increasing O-GlcNAcylation levels led to elevated G6P levels in cells expressing WT HK1, whereas this effect was absent in cells expressing T259A-HK1 (Fig. 5b). Importantly, the expression levels of both WT HK1 and T259A-HK1 remained constant (Extended Data Fig. 5a,b), indicating that the observed differences in G6P levels were specifically attributed to O-GlcNAcylation of HK1. Upregulation of O-GlcNAcylation in HEK293T cells also enhanced the production of G6P without altering endogenous HK1 expression levels (Extended Data Fig. 5c–e).

To assess the functional consequences of O-GlcNAcylation on HK1 activity and cellular metabolism, we examined glycolytic and mitochondrial oxidative phosphorylation (OXPHOS) ATP production rates using respirometry measurements in HEK293T cells. ATP production rates were empirically calculated based on oxygen consumption and extracellular acidification data obtained using a Seahorse XF analyzer, as previously described[29]. We found that upregulating O-GlcNAcylation levels, either by OGA inhibition or by expressing WT HK1 with Thiamet-G treatment, resulted in increased glycolytic and mitochondrial OXPHOS ATP production rates (Fig. 5c). By contrast, cells expressing the T259A-HK1 mutant showed diminished ATP production rates, indicating the dependence of HK1 activity on O-GlcNAcylation. Moreover, the elevation in oxygen consumption rates (OCR) and extracellular acidification rates (ECAR) observed with O-GlcNAcylation upregulation was consistent with enhanced metabolic activity (Extended Data Fig. 5f). Notably, these effects were specific to O-GlcNAcylation status and were not influenced by changes in endogenous HK1, WT HK1 or T259A-HK1 expression levels (Extended Data Fig. 5g–i). These findings

Fig. 5 | HK1 O-GlcNAcylation enhances metabolic efficiency. **a**, HK catalyses the first step of glucose metabolism, where glucose and ATP are converted into G6P and ADP. **b**, Quantification of G6P levels in HEK239T cells expressing eGFP-tagged WT or T259A-HK1 with or without ectopic OGT expression and Thiamet-G treatment (four biological replicas, mean ± s.e.m. and associated *P* values; one-way ANOVA, post hoc Holm–Šídák's multiple comparison test). **c**, Mitochondrial and glycolytic ATP production rates calculated from HEK293T cells expressing control vector, WT or T259A-HK1, following vehicle or Thiamet-G treatments (three biological replicas, mean ± s.e.m. and associated *P* values; Mann–Whitney *U*-test). **d**, Average fluorescence traces of the intracellular FBP sensor, HYlight, in neuronal axons expressing shRNA-resistant FLAG-tagged WT or T259A-HK1, and rat shRNA-HK1. The arrowhead indicates the application of the glycolysis inhibitor 2-DG and the electrical field stimulation (100 APs, 10 Hz). Data are presented as mean ± s.e.m.; *n* = 10 neurons from three independent experiments. **e**, The strategy for inducing the mitochondrial relocation of truncated cytoplasmic HK1 (Tr-HK1). The dimerization of the FRB domain on Tr-HK1–GFP and the FKBP domain on a mitochondria-targeted mCherry tag upon AP21967 treatment. **f**, Representative HEK293T cell expressing FRB-Tr-HK1–GFP(green) and mCherry-mito-FKBP(magenta) before and 10 min after dimerizer treatment. Scale bars, 5 µm. **g**, Mitochondrial and glycolytic ATP production rates were calculated for HEK293T cells expressing either control Tr-HK1–GFP, FRB-Tr-HK1–GFP or FRB-Tr-HK1-T259A–GFP, with or without AP21967 treatments (three biological replicas, mean ± s.e.m., one-way ANOVA, post hoc Kruskal–Wallis multiple comparison test). **h**, Diagram illustrating glycolysis enzymes. The two steps of glycolysis that generate ATP are indicated by red arrows. **i**,**j**, Analysis of glycolytic enzymes in mitochondrial and cytoplasmic fractions. **i**, HEK293T cells treated with vehicle or Thiamet-G, then mitochondrial and cytoplasmic fractions were subjected to SDS–PAGE and analysed by western blotting using antibodies against HK1, PKM2, Aldo A, PGK, ATP5B (mitochondrial marker) and tubulin (cytoplasmic marker). **j**, Quantification of glycolytic enzymes in mitochondrial, cytoplasmic fractions and total cell lysates (input), normalized to the intensity of ATP5B and tubulin. Data are presented as mean ± s.e.m. from three biological replicas (one-tailed Mann–Whitney *U*-test). See also Extended Data Fig. 5.

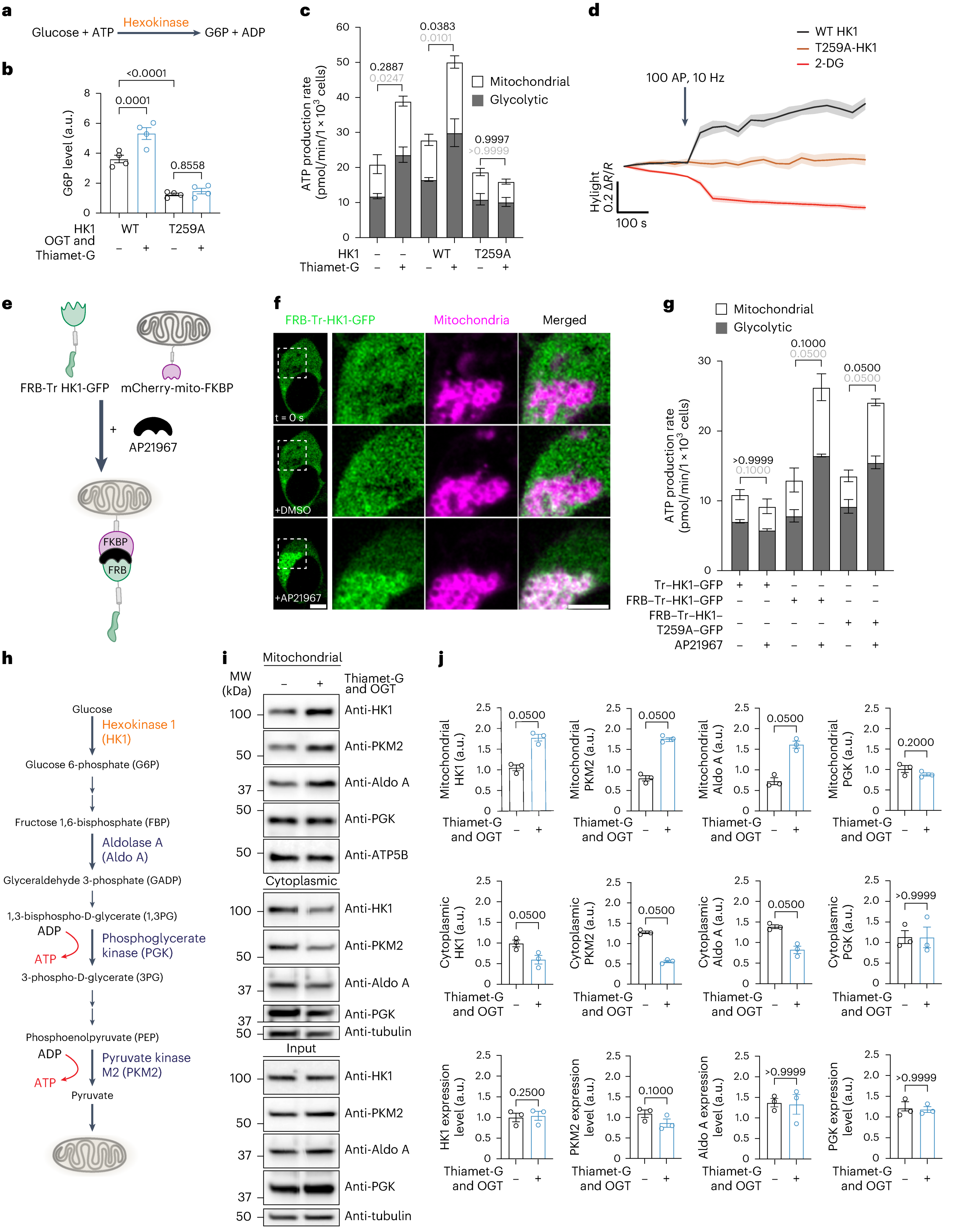
a
Glucose + ATP
Hexokinase
G6P + ADP
b
G6P level (a.u.)
<0.0001
0.0001
0.8558
HK1 WT T259A
OGT and Thiamet-G – + – +
c
ATP production rate (pmol/min/1 × 10³ cells)
0.2887
0.0247
0.0383
0.0101
0.9997
>0.9999
Mitochondrial
Glycolytic
HK1 – – WT T259A
Thiamet-G – + – + – +
d
WT HK1
T259A-HK1
2-DG
100 AP, 10 Hz
Hylight 0.2 ΔR/R
100 s
e
FRB-Tr HK1-GFP
mCherry-mito-FKBP
+
AP21967
FKBP
FRB
f
FRB-Tr-HK1-GFP
Mitochondria
Merged
t = 0 s
+DMSO
+AP21967
g
Mitochondrial
Glycolytic
ATP production rate (pmol/min/1 × 10³ cells)
>0.9999
0.1000
0.1000
0.0500
0.0500
0.0500
Tr–HK1–GFP + + – – – –
FRB–Tr–HK1–GFP – – + + – –
FRB–Tr–HK1–T259A–GFP – – – – + +
AP21967 – + – + – +
h
Glucose
Hexokinase 1 (HK1)
Glucose 6-phosphate (G6P)
Fructose 1,6-bisphosphate (FBP)
Aldolase A (Aldo A)
Glyceraldehyde 3-phosphate (GADP)
1,3-bisphospho-D-glycerate (1,3PG)
ADP
ATP
Phosphoglycerate kinase (PGK)
3-phospho-D-glycerate (3PG)
Phosphoenolpyruvate (PEP)
ADP
ATP
Pyruvate kinase M2 (PKM2)
Pyruvate
i
Mitochondrial
MW (kDa)
Thiamet-G and OGT – +
100 Anti-HK1
50 Anti-PKM2
37 Anti-Aldo A
50 Anti-PGK
50 Anti-ATP5B
Cytoplasmic
100 Anti-HK1
50 Anti-PKM2
37 Anti-Aldo A
37 Anti-PGK
50 Anti-tubulin
Input
100 Anti-HK1
50 Anti-PKM2
37 Anti-Aldo A
37 Anti-PGK
50 Anti-tubulin
j
Mitochondrial HK1 (a.u.) 0.0500
Mitochondrial PKM2 (a.u.) 0.0500
Mitochondrial Aldo A (a.u.) 0.0500
Mitochondrial PGK (a.u.) 0.2000
Cytoplasmic HK1 (a.u.) 0.0500
Cytoplasmic PKM2 (a.u.) 0.0500
Cytoplasmic Aldo A (a.u.) 0.0500
Cytoplasmic PGK (a.u.) >0.9999
HK1 expression level (a.u.) 0.2500
PKM2 expression level (a.u.) 0.1000
Aldo A expression level (a.u.) >0.9999
PGK expression level (a.u.) >0.9999
Thiamet-G and OGT – +

highlight the role of O-GlcNAcylation in modulating HK1-mediated ATP production rates through both glycolytic and mitochondrial pathways. To determine how O-GlcNAcylation of HK1 influences the rate of glycolysis, we assessed fructose 1,6-bisphosphate (FBP) levels in neuronal axons using HYlight[30], a fluorescent sensor that reports glycolytic activity[31]. It is known that neuronal activity transiently augments glucose uptake and glycolysis[32]. Our axonal measurements indicated that action potential (AP) firing (10 Hz, 100 APs) increased cytosolic FBP levels in neurons expressing WT HK1–FLAG. This enhancement was absent in neurons expressing the O-GlcNAc site mutant HK1, T259A-HK1–FLAG. Furthermore, when glucose was replaced with 2-deoxyglucose (2-DG) to inhibit FBP production, we observed a gradual decrease in FBP levels (Fig. 5d) with neuronal activity.

To rescue the impaired functional activity of the T259A-HK1, we used a chemically induced protein dimerization strategy to promote mitochondrial recruitment. We used a dual-tagged construct in which truncated cytoplasmic HK1 (Tr-HK) was tagged with the FKBP-rapamycin-binding (FRB) domain at its N terminus and GFP at its C terminus. By co-expressing FRB-Tr-HK1–GFP and mCherry-mito-FKBP (FK506 binding protein domain), we could selectively recruit cytoplasmic HK1 to the mitochondria upon treatment with the dimerizer AP21967, as confirmed through time-lapse imaging (Fig. 5e,f). To evaluate the functional rescue of T259A-HK1 activity, we measured ATP production rates in cells in which T259A-HK1 was targeted to the mitochondrial outer membrane with the dimerizer. We observed a significant increase in both glycolytic and mitochondrial OXPHOS ATP production rates after recruiting cytoplasmic T259A-HK1 to the mitochondria (Fig. 5g). This phenotypic rescue indicates that the impaired enzymatic activity of T259A-HK1 can be restored by targeted localization to the mitochondria, leading to enhanced ATP production rates. These results further highlight the significance of O-GlcNAcylation in modulating HK1 activity by regulating its mitochondrial localization.

HK1 O-GlcNAcylation seeds glycolytic metabolon

Enzymes involved in glycolysis are generally dispersed throughout the cytoplasm in cells[33]. However, under certain conditions, such as hypoxia[34–37], these enzymes can compartmentalize to form metabolons, specialized microenvironments that enhance the transfer of metabolites from one enzyme to another[38,39]. This process enhances the efficiency of metabolic pathways and increases the overall metabolic output[40]. Given this knowledge, we sought to investigate the potential role of O-GlcNAcylation in recruiting other glycolytic enzymes to mitochondria to form metabolon for metabolic efficiency (Fig. 5h). We upregulated O-GlcNAcylation levels in HEK239T cells by ectopically expressing OGT and inhibiting OGA using Thiamet-G. We isolated whole cell lysate (input), mitochondrial and cytoplasmic fractions, which were then resolved on SDS–PAGE gels. We evaluated the purity of mitochondrial fractions by probing with markers specific to other organelles. The results demonstrated negligible to no contamination from non-mitochondrial sources (Extended Data Fig. 5j). We probed the gels with antibodies against endogenous HK1, pyruvate kinase M2 (PKM2), aldolase A (Aldo A), phosphoglycerate kinase (PGK), ATP5B (a mitochondrial marker) and tubulin alpha-4A (a cytoplasmic marker). Interestingly, our results indicated that enhanced O-GlcNAcylation not only increased the amount of HK1 in the mitochondria but also augmented the levels of PKM2 and Aldo A on the mitochondria, a process that was parallel with their decrease in the cytoplasmic fraction (Fig. 5i,j). However, the increased O-GlcNAcylation levels did not appear to significantly alter the localization of PGK (Fig. 5i,j) in HEK293T cells.

We extended our analysis to cultured primary cortical neurons, probing for the presence of glycolytic enzymes in mitochondrial fractions under conditions of upregulated O-GlcNAcylation. We assessed the purity of neuronal mitochondrial fractions using markers specific to other organelles. The results confirmed a high purity of the mitochondrial preparations (Extended Data Fig. 5k). Intriguingly, a significant portion of glycolytic enzymes are associated with purified mitochondria from cortical neurons. To account for the impact of upregulated O-GlcNAcylation, we normalized mitochondrial and cytoplasmic enzyme levels to the baseline. This showed that upregulated O-GlcNAcylation increased the mitochondrial localization of HK1, Aldo A, PGK, neuron-specific enolase, triosephosphate isomerase and PKM in cortical neurons while decreasing their presence in the cytoplasm (Extended Data Fig. 5l,m). In addition to biochemical methods, we investigated the O-GlcNAcylation-dependent recruitment of glycolytic enzymes to mitochondria using complementary imaging techniques. We transfected neurons with eGFP-tagged PKM2 along with the mitochondrial marker Mito-DsRed and then treated the cells with inhibitors of OGT or OGA (Extended Data Fig. 5n,o). Consistent with our observations for HK1 (Fig. 2d), enhanced O-GlcNAcylation led to the mitochondrial association of PKM2. Conversely, inhibiting OGT activity resulted in a redistribution of PKM2 to the cytoplasm (Extended Data Fig. 5n,o). Our results suggest that O-GlcNAcylation not only intensifies HK1 activity but also promotes the recruitment of rate-limiting glycolytic enzymes to mitochondria, resulting in increased ATP production rates. Collectively, our findings highlight the crucial role of HK1 O-GlcNAcylation in promoting the assembly of a glycolytic metabolon on mitochondria. Overall, these results demonstrate that O-GlcNAcylation has a crucial role in facilitating the formation of a glycolytic metabolon on the mitochondria, where key enzymes involved in glycolysis are recruited, resulting in enhanced ATP production. This mechanism provides insight into the coordination between glycolytic and mitochondrial metabolism and highlights the significance of O-GlcNAcylation in regulating cellular energy metabolism.

O-GlcNAcylation stabilizes HK1 on mitochondria

Mitochondrial localization of HK1 is known to be modulated by G6P concentrations; elevated G6P concentrations can lead to the release of HK1, which acts as an inhibitory feedback mechanism[41]. We reasoned that O-GlcNAcylation stabilizes HK1 on the mitochondria by counteracting this G6P-induced feedback loop. To test our hypothesis, we combined computational simulations and experimental assays. First, we used steered molecular dynamics simulations to understand the mechanism of G6P binding and unbinding from the N-terminal pocket of HK1. Given that traditional molecular dynamics simulations did not fully capture this process, we turned to steered molecular dynamics simulations. These simulations demonstrated that the average work required to unbind G6P from the pocket was 13-fold lower for O-GlcNAc-modified HK1 compared to WT HK1 (Fig. 6a). This suggests that O-GlcNAcylation of the binding pocket reduces the affinity to G6P. To further corroborate our findings, we performed alchemical free-energy perturbation calculations, which indicated a shift in the dissociation constant of G6P from 6.9 nM to 12 mM upon O-GlcNAcylation of the N-terminal binding pocket. The model was further supported by dynamic network analysis (Fig. 6b,c).

To further investigate whether O-GlcNAcylation of HK1 strengthens its mitochondrial association by counteracting G6P-dependent feedback inhibition, we isolated mitochondria from HEK293T cells expressing endogenous HK1, WT HK1–GFP or T259A-HK1–GFP. We then evenly distributed these mitochondrial fractions into three tubes containing 0 μM, 250 μM and 500 μM G6P (Fig. 6d), concentrations that are within the physiological range for G6P[28,42]. After a 30 min incubation at room temperature (20–25 °C), mitochondria were pelleted, separating them from the flowthrough that contains proteins released from the mitochondria (Fig. 6d). We observed that as G6P concentrations increased, more HK1 was released from the mitochondria (Fig. 6e,f). Comparing the released HK1 from mitochondria at baseline and upregulated O-GlcNAcylation levels, we observed that increased O-GlcNAcylation resulted in less HK1 being released from mitochondria at the same G6P concentration (Fig. 6e–h). We found that upregulating O-GlcNAcylation levels would stabilize WT HK1 on mitochondria by

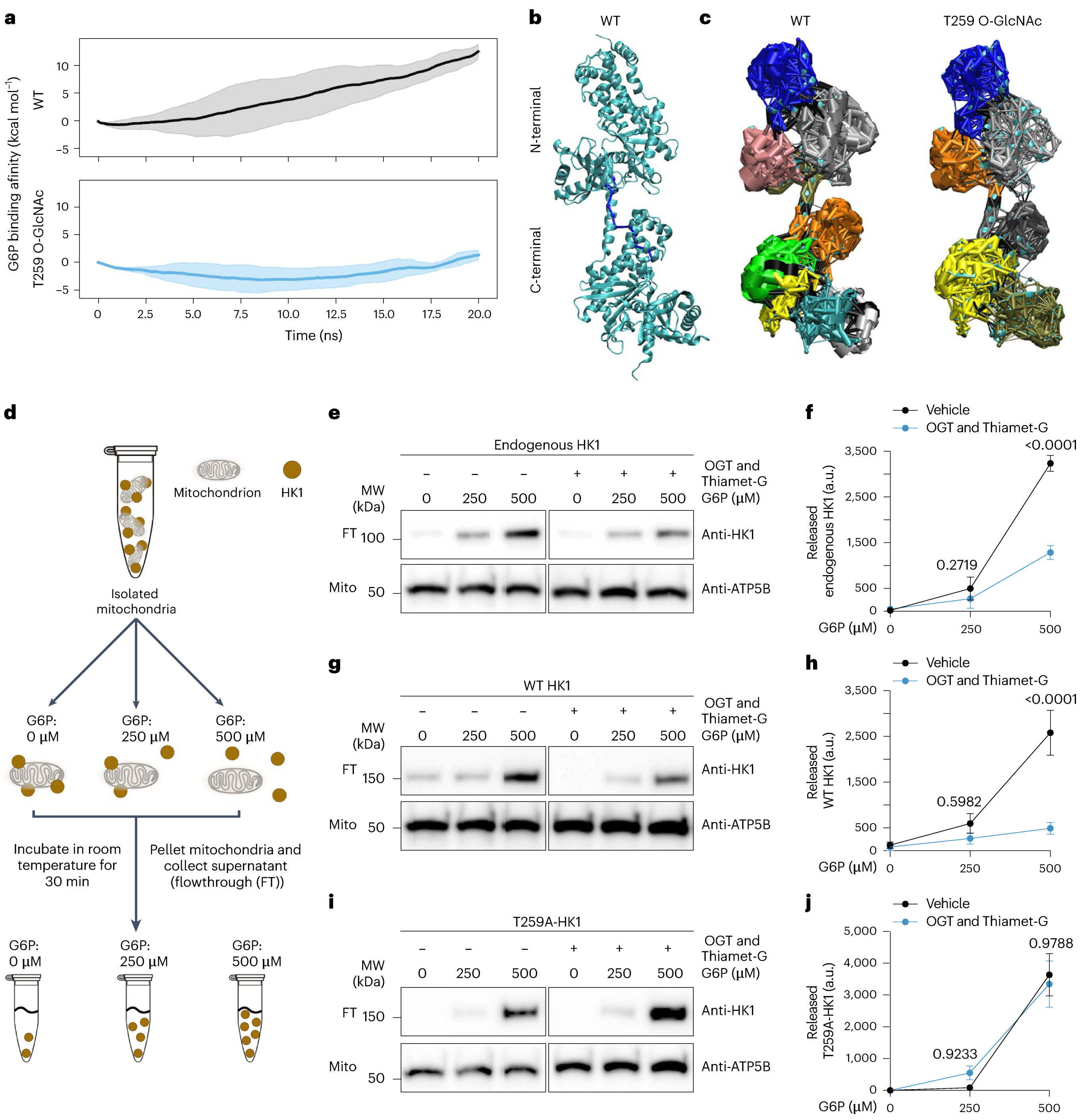

Fig. 6 | O-GlcNAcylation modifies G6P affinity and stabilizes HK1 on mitochondria. a, The average accumulated work profiles computed from steered molecular dynamics simulations in which G6P was pushed out of the N-terminal binding pocket. The line represents the average accumulated work over 20 steered molecular dynamics simulations, and the shading indicates one standard deviation from the mean accumulated work. **b**, Optimal pathway of information transfer from the N-terminal Ser449 to the C-terminal Thr784 for the unmodified HK1. Dark blue nodes (spheres representing Cα atoms) and edges (cylinders representing allosteric interactions) illustrate the optimal pathway of allosteric interactions. **c**, The community substructure for the network of allosteric interactions. Nodes within a community (single colour) represent a network of interactions with more frequent and stronger connections with nodes in a community than with nodes outside of that community. Black edges represent connections between communities. **d**, Schematic diagram illustrating the G6P titration assay for mitochondrial fractions. Isolated mitochondria, containing HK1, were exposed to three different concentrations of G6P for 30 min at room temperature. Following incubation, mitochondria and the supernatant, which contains the released HK1, were separated by centrifugation. Both the pellet (mitochondria) and supernatant (flowthrough containing released HK1) were collected and subsequently analysed. **e**–**j**, Mitochondrial fractions were prepared from HEK239T cells expressing control vector (**e**,**f**), eGFP-tagged WT (**g**,**h**) or T259A-HK1 (**i**,**j**) with or without OGT co-expression and overnight Thiamet-G treatment. Flowthrough (FT) fractions were collected as described in **d** following 0 μM, 250 μM and 500 μM G6P treatments of the mitochondrial pellet (Mito). In **e, g** and **i**, samples were separated by SDS gel electrophoresis and probed with anti-HK1 and anti-ATP5B (mitochondrial marker) antibodies. In **f, h** and **j**, the total intensity of the HK1 band was quantified for each condition. *n* = 3 independent experiments (all values are shown as mean ± s.e.m.; one-way ANOVA with post hoc Holm-Šídák's multiple comparison test). See also Extended Data Fig. 6.

counteracting G6P negative feedback (Fig. 6g,h) but not for T259A-HK1 (Fig. 6i,j). Thus, O-GlcNAcylation is necessary for protecting HK1 from being released from mitochondria by G6P feedback inhibition.

Building on these molecular insights, we next delved into the broader cellular context to understand the implications of HK1 T259 O-GlcNAcylation on glycolytic metabolon formation. We analysed the positioning of other glycolytic enzymes in HEK239T cells after expressing either WT HK1 or T259A-HK1 from mitochondrial and cytoplasmic fractions. When we enhanced O-GlcNAcylation levels in cells overexpressing WT HK1, we observed increased mitochondrial localization of WT HK1 along with other glycolytic enzymes, such as Aldo A, PGK and PKM2. At the same time, their cytoplasmic levels declined without a change in overall expression levels (Extended Data Fig. 6a,b). However, in cells overexpressing T259A-HK1 with increased O-GlcNAcylation levels, we did not detect a significant increase in mitochondrial localization of T259A-HK1, Aldo A, PGK or PKM2. The cytoplasmic levels of these enzymes remained largely unchanged, as did their total expression levels (Extended Data Fig. 6c,d). These results further emphasize the specific role of HK1 O-GlcNAcylation in promoting the recruitment and localization of glycolytic enzymes on mitochondria, supporting the formation of the metabolon for efficient ATP production.

HK1 O-GlcNAcylation supports presynaptic function

Given the role of HK1 O-GlcNAcylation in cellular metabolism, we next questioned how this modification might impact the high energy demands of neurons. Neuronal activity and synaptic vesicle recycling heavily rely on ATP produced at presynaptic sites[43,44]. To investigate the impact of HK1 O-GlcNAcylation on neuronal function, we conducted live-cell imaging in rat hippocampal neurons and measured axonal ATP level and synaptic vesicle recycling rate. To measure ATP level, we expressed the cytoplasmic ATP sensor iATPSnFR1.0-mRuby in neurons with shRNA against HK1, shRNA-resistant WT HK1–BFP or T259A-HK1–BFP (O-GlcNAc silent HK1) and triggered AP firing at 10 Hz, 100 APs. Measurements from neuronal axons in control neurons expressing WT HK1 revealed that a burst of electrical activity resulted in only a small decrease in ATP levels during the post-stimulus period, which was followed by an immediate recovery (Fig. 7a,b). On the contrary, in neurons expressing T259A-HK1, ATP levels never recovered (Fig. 7a,b). When both glycolytic and mitochondrial (2-DG + oligomycin) ATP synthesis pathways were blocked during electrical stimulation, the ATP levels further decreased. We also aimed to measure the recycling kinetics of presynaptic vesicles in response to neuronal activity and evaluate the role of HK1 O-GlcNAcylation in presynaptic function. These neurons expressed either shRNA against HK1, shRNA-resistant WT HK1–BFP or T259A-HK1–BFP (O-GlcNAc silent HK1) along with mCherry as an axon filler and vGLUT1–pH, a pH-sensitive fluorescent probe attached to vesicular glutamate transporter (vGLUT1) (Fig. 7e,f). Under baseline conditions, neurons displayed spontaneous activity, with some vGLUT1–pHluorin on the axonal surface. Neuronal activation with 100 APs at 10 Hz significantly enhanced the fluorescence intensity of vGLUT1–pH, indicating the release of synaptic vesicles. The fluorescence signal quickly returned to baseline levels, reflecting the vesicle retrieval. The addition of NH_4Cl at the end of the experiment allowed visualization of all presynaptic vesicles containing vGLUT1–pH (Fig. 7f,g). Comparing neurons expressing WT HK1 with T259A-HK1 revealed lower baseline vGLUT1–pH signals in neurons expressing the O-GlcNAc silent T259A-HK1 (Fig. 7f,g), independent of protein expression levels (Extended Data Fig. 7a–c). After applying 100 APs at 10 Hz, neurons expressing T259A-HK1 exhibited significantly lower vGLUT1–pH fluorescence intensity than WT HK1-expressing neurons. Notably, there was no difference in the number of presynaptic release sites containing vGLUT1–pH between WT HK1 and T259A-HK1-transfected neurons when treated with NH_4Cl (Fig. 7f). These results suggest that HK1 O-GlcNAcylation has a crucial role in supporting energy-dependent presynaptic vesicle recycling.

We further investigated whether the observed reduction in presynaptic vesicle recycling in neurons expressing T259A-HK1 was a result of chronic energy deficiency. We transfected neurons with either WT HK1 or T259A-HK1–BFP, along with vGLUT1–pH. Under baseline conditions, our primary neuron cultures form spontaneously active networks and fire APs (as shown in Extended Data Fig. 7). To suppress this spontaneous neuronal activity and conserve ATP levels by reducing the energy demand, we added 1 µM tetrodotoxin (TTX)—a blocker of voltage-gated sodium channels—immediately after transfection. Then, 2 h before imaging, we removed TTX to allow the recovery of baseline presynaptic vesicle recycling (Extended Data Fig. 7d). This strategy of preserving ATP levels and preventing chronic metabolic deficiency through TTX treatment enabled neurons expressing T259A-HK1 to restore their presynaptic vesicle recycling to levels comparable to those observed in WT HK1-expressing neurons. Furthermore, following a single round of electrical stimulation, presynaptic vesicle recycling was successfully rescued in T259A-HK1-expressing neurons, demonstrating a similar performance to that of WT HK1-expressing neurons (Extended Data Fig. 7d–g). To evaluate the effect of HK1 O-GlcNAcylation on Ca^{2+} dynamics, we used GCaMP6s, a genetically encoded fluorescent Ca^{2+} indicator, co-expressed shRNA against HK1, WT HK1–BFP or T259A-HK1–BFP in neurons. The GCaMP6s signal provided measurements of calcium fluctuations evoked by neuronal activity (10 Hz, 100 APs). Analysis of calcium dynamics indicated that uptake and clearance mechanisms underlying calcium dynamics were comparable between the two conditions (Extended Data Fig. 8a–f). These results indicate that the regulation of presynaptic vesicle recycling by HK1 O-GlcNAcylation operates independently of Ca^{2+} handling.

Fig. 7 | Presynaptic function relies on HK1 O-GlcNAcylation. a, Representative images of neuronal axons expressing ATP sensor iATPSnFR1.0-mRuby (pseudocolour, fire for iATPSnFR and magenta for mRuby), and shRNA-resistant BFP-tagged WT or T259A-HK1 (grey) with HK1-shRNA. Images were taken before, and 40 s and 490 s after stimulation with 100 APs at 10 Hz, and with indicated pharmacological treatments. Scale bar, 5 µm. **b**, Average fluorescence traces of iATPSnFR, with indicated conditions or pharmacological treatments and field stimulation (10 Hz, 100 APs) (black, WT HK1–BFP with HK1-shRNA; brown, T259A-HK1–BFP with HK1-shRNA; red, 2-DG and oligomycin-treated neurons). **c**, Average fluorescence traces of mRuby (magenta) control under conditions as indicated in **b** before, and 40 s and 490 s following stimulation with 100 APs at 10 Hz. All values are shown as mean ± s.e.m.; *n* = 9–10 neurons, three independent experiments. **d**, Schematic of the pHluorin-tagged vesicular glutamate transporter 1 (vGLUT1–pH), located at the presynaptic release site of a neuron. The pHluorin protein, conjugated to the luminal domain of vGLUT1, exhibits fluorescence quenching at the acidic pH (~5.5) inside synaptic vesicles. Upon neuronal stimulation and vesicle fusion, the luminal tag is exposed to the extracellular pH, leading to a significant increase in fluorescence. Post endocytosis, pHluorin fluorescence is quenched again as the vesicle lumen becomes acidic by the activity of the vacuolar ATPase (v-ATPase). **e**, Schematic demonstrating the experimental design. **f**, Hippocampal neurons expressing either WT or T259A-HK1–BFP. HK1-shRNA with vGLUT1–pH were electrically stimulated with 100 APs at 10 Hz. Representative images display vGLUT1–pH (pseudocolour, fire) and mCherry cell filler (grey) before and after stimulation in neuronal axons expressing either WT or T259A-HK1–BFP. Neutralization of vGLUT1–pH vesicles with NH_4Cl treatment reveals total axonal vesicle pool. Scale bar, 5 µm. **g**, Average trace of vGLUT1–pH with 100 APs 10 Hz stimulation in WT HK1 (black) or T259A-HK1 (orange) expressing neurons. ΔF values were normalized to maximal ΔF obtained from NH_4Cl treatment. **h**, Baseline and maximal (post electrical stimulation) vGLUT1–pH $\Delta F/F$ values. All values are shown as mean ± s.e.m.; *n* = 10–11 neurons and 91–205 presynaptic boutons, four independent experiments (unpaired two-tailed *t*-test). See also Extended Data Figs. 7 and 8.

However, although no differences in calcium dynamics were observed in spiking neurons, the inhibition of HK1 O-GlcNAcylation was found to reduce overall neuronal network activity (Extended Data Fig. 8g,h), as measured by multi-electrode array recordings from neurons expressing endogenous levels of WT or T259A-HK1. Our findings highlight the essential role of O-GlcNAcylation of HK1 in addressing localized energy demands and 'on demand' ATP synthesis in neurons. Specifically, this post-translational modification of HK1 is indispensable for proper vesicle recycling at presynaptic terminals, a compartmentalized ATP-intensive process.

Discussion

Cells operate within a finely tuned signalling network in which metabolism, efficient energy management and nutrient sensing work in unison to ensure optimal cellular function and viability under an ever-changing nutrient environment. Among these intricate mechanisms, O-GlcNAcylation has recently emerged as a key nutrient-sensing post-translational modification[45]. Our study provides critical insights into the regulatory role of O-GlcNAcylation in cellular metabolism and energy homeostasis, specifically through its modulation of the positioning and activity of HK1, an enzyme central to glucose metabolism[28,46].

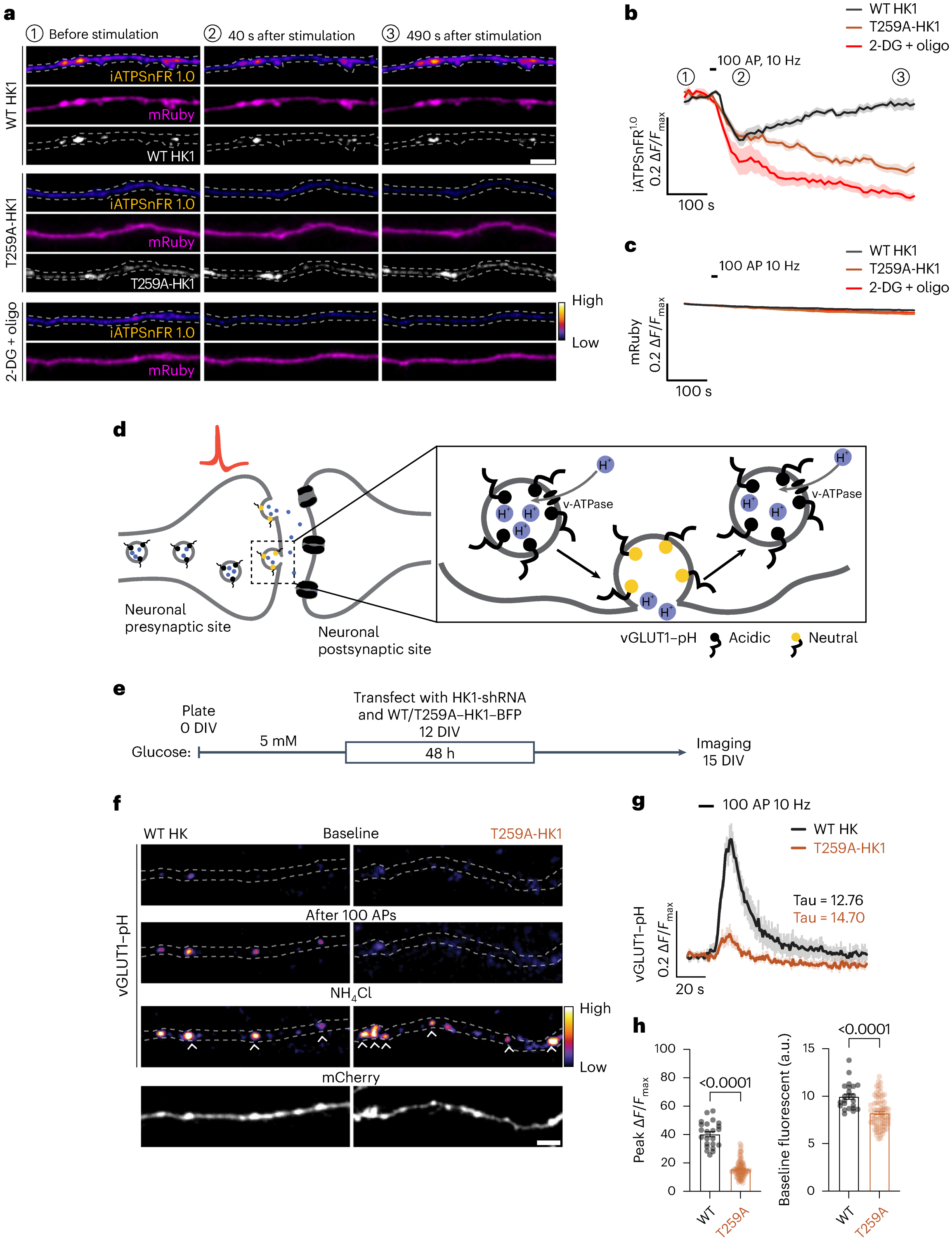

Our findings demonstrate a dynamic regulatory feedback system in which glucose levels, through the mediation of O-GlcNAcylation, orchestrate the positioning of HK1 to mitochondria. This regulatory mechanism involves the O-GlcNAcylation of Thr259 on HK1, which we found to be crucial for HK1 localization and activity. Moreover, our study provides evidence of how HK1 O-GlcNAcylation promotes the formation of a glycolytic metabolon on the mitochondrial outer membrane. Metabolon formation increases the efficiency of glucose metabolism and ATP generation, crucial for high-energy-demanding areas such as the presynaptic sites in neurons.

The O-GlcNAcylation of HK1 is tightly correlated with its positioning on mitochondria, whether the level was manipulated by overexpression of OGT, pharmacological inhibition of OGT and OGA or by nanobody-mediated targeting of O-GlcNAc cycling (Figs. 2 and 3). OGT post-translationally modifies over 8,000 proteins, including several glycolytic enzymes such as PKM2 (ref. 47), PFK[48] and PGK1 (ref. 49), all of which potentially impact cellular metabolism. However, by mapping and mutating the only site of O-GlcNAcylation on HK1 (T259A-HK1), we demonstrated that HK1 is an essential substrate through which OGT can enhance the ATP synthesis rate (Figs. 4 and 5). Although T259A-HK1 does not alter HK1 enzymatic activity, we found that it selectively prevents mitochondrial recruitment of HK1 and the formation of the glycolytic metabolon on mitochondria (Fig. 5 and Extended Data Fig. 6). These findings reveal a previously unappreciated role for HK1 in regulating cellular energy metabolism through glucose and O-GlcNAcylation-dependent mitochondrial localization.

Cells maintain metabolic homeostasis through the precise sensing and regulation of glucose fluctuations. Within this complex regulatory landscape, O-GlcNAcylation emerges as a crucial modulator[45]. In contrast to other forms of protein glycosylation, certain O-GlcNAcylation sites are dynamically regulated, undergoing rapid addition or removal in response to changes in the cellular state, such as excitatory neuronal stimuli[50,51]. Conversely, other sites primarily fulfil structural roles and exhibit slower turnover[52]. Only dynamic and substoichiometric O-GlcNAcylation is highly responsive to glucose concentrations, influx through hexosamine biosynthetic pathway and OGA inhibition (with PUGNAC or Thiamet-G) in neurons and other cell types[18,20,53]. Our study shows that dynamic changes of HK1 O-GlcNAcylation on the highly conserved T259 site allow metabolic sensing (Figs. 2–4). The widely expressed HK isoform HK2, which lacks the T259 O-GlcNAcylation site, does not exhibit similar regulation in response to genetic or pharmacological OGT and OGA manipulations (Extended Data Fig. 3). Notably, HK1 contains an N-terminal regulatory domain instead of two catalytic domains found in HK2. Our study reveals that the affinity of G6P to the N-terminal domain binding pocket is markedly reduced upon T259 O-GlcNAcylation (Fig. 6). Previous studies have suggested an allosteric communication from the non-catalytic N-terminal domain of HK1 to the catalytic C-terminal binding pocket, wherein binding G6P at the N terminus promotes a conformational change at the C terminus[25]. Hence, we postulate that O-GlcNAcylation of HK1 averts allosteric regulation by the N-terminal binding pocket on the C-terminal catalytic pocket, ensuring that HK1 remains catalytically active despite the presence of G6P. Our observations indicate that the binding of G6P to the N-terminal pocket significantly reduces the dipole moment of HK1, causing its N-terminal domain to have a less preferential orientation in the electrostatic field created by the negatively charged outer mitochondrial membrane. The N-terminal domain of HK1 contains the mitochondrial targeting domain[17]. Potentially, an increase in the molecular dipole orients the N-terminal half of HK1 toward the mitochondrial outer membrane, allowing the mitochondrial targeting domain to insert itself into the membrane. Taken together, our study offers a rare and compelling demonstration of how a singular post-translational modification, O-GlcNAcylation, influences the structure and function of HK1, unravelling critical insights into the complex and finely tuned metabolic regulation of this pacemaker enzyme.

Glucose regulates the localization of mitochondria in neurons through OGT and O-GlcNAcylation[18,20], allowing the cell to adjust to spatial heterogeneity in glucose concentration and directing mitochondria to the glucose-rich areas[54,55]. We have now revealed another layer of regulation and elucidated that OGT and O-GlcNAcylation, by altering the HK1 structure and mitochondrial localization, also regulates the spatial organization of glycolytic enzymes, promoting ‘metabolon’ formation on mitochondria to bolster metabolic efficacy (Fig. 5 and Extended Data Fig. 5). Assembling enzymes with their subsequent substrates in close proximity increases reaction rates through substrate channelling[56,57]. Substrate channels between glycolytic enzymes located on the mitochondrial surface in neurons could be a regulatory mechanism to ensure that adequate pyruvate is supplied into mitochondria when respiratory demand increases rather than allowing glycolytic intermediates to be diffused or used for an alternative metabolic pathway. Conversely, the release of HK into the cytoplasm would result in more spatially uniform glucose consumption, negating the metabolic enhancement achieved through mitochondrial localization. The formation of glycolytic metabolon was previously observed in multiple cell types, including yeast[35,37,38,58,59], cancer cells[39,60], *Trypanosoma*[61], pancreatic islet cells[2], red blood cells[5] and muscle cells[3,62,63], and also in response to hypoxia in *C. elegans* neurons[34,36]. Here, we provide a molecular mechanism that promotes glycolytic metabolon formation on mitochondria through post-translational modification of HK1. This mechanism amplifies both glycolytic and mitochondrial ATP synthesis rates. Importantly, this regulation by O-GlcNAcylation of HK1 is dynamic, leading to the redistribution of glycolytic enzymes within minutes. This dynamic rearrangement underscores the existence of a spatially and temporally synchronized system for glucose uptake, processing and ATP production, reinforcing cellular energy homeostasis.

In the context of neurons, a cell type with substantial and localized energy needs, coupling glycolysis to mitochondria through the O-GlcNAcylation mechanism becomes particularly crucial. Despite their significant energy demands, neurons lack stored ATP and predominantly metabolize glucose through glycolysis to meet acute energy requirements[32,43,44,64,65]. Synaptic activity and AP firing also create a rapid and highly dynamic energetic demand for neurons. In response to periods of high activity, neurons increase in both surface glucose transporter levels and glucose uptake, aligning with the intensified demand for ATP[43,44]. This dynamic is underscored by findings that synaptic activity boosts glucose consumption by a median of 1.9-fold[66] and also promotes O-GlcNAcylation[51]. Intriguingly, a previous publication indicated that in a resting adult mouse brain, HK operates at a mere 3% of its maximum capacity, suggesting an available 33-fold increase in activity[36]. Here, we provide a molecular mechanism in which the O-GlcNAcylation of HK1 would increase its activity and ATP production at presynaptic sites, thus supplying the high energy demand during intense synaptic activity (Fig. 7). Dysregulation of HK1 O-GlcNAcylation resulting from the introduction of a T259A mutation causes chronic impairment in glucose metabolism and energy depletion, and likely impairs presynaptic vesicle recycling owing to ATP insufficiency[67]. Moreover, alterations in the cytoplasmic or mitochondrial localization of HK1 could affect the local availability of ATP and ADP pools. The docking, exocytosis and endocytosis of synaptic vesicles at the active zone are ATP-dependent processes[43,67]. Although endocytosis is significantly more sensitive to decreases in energy levels[43,67], exocytosis still requires some ATP to proceed effectively[68]. The synaptic vesicles themselves also demand a significant amount of ATP, especially given their reliance on vesicular v-ATPase activity for filling vesicles with neurotransmitters[69]. Therefore, it is consistent that silencing neurons using TTX—which blocks neuronal activity and conserves ATP levels, and potentially other metabolites—rescues the synaptic vesicle recycling defects observed with the T259A mutation (Fig. 7).

Neurological diseases, including Alzheimer's disease[70,71], depression[72] and schizophrenia[73], have been correlated with metabolic dysfunction, such as the dissociation of HK1 from mitochondria and reduced glucose metabolism[74–76]. The prevalence of O-GlcNAcylation within the brain, coupled with the changes in glucose metabolism in the brains of patients with Alzheimer's disease, suggests that O-GlcNAcylation may have important roles in the progression of Alzheimer's disease[77–81]. The precise regulation of glucose sensing, uptake and processing is fundamental to cellular metabolic adaptability. In this study, we elucidate how nutrient-sensing influences HK1 O-GlcNAcylation and its interaction with neuronal mitochondria, optimizing metabolic efficiency through the post-translational modification mechanism. Disruptions in this metabolic pathway correlate with various neurological disorders, suggesting a previously unidentified involvement in neuropathologies. By unravelling this essential feedback mechanism, which integrates synaptic activity with ATP synthesis, we set the stage for discovering potential therapeutic targets in neuronal dysfunction.

Methods

Mice and rat strains and maintenance

All animal experiments were conducted according to the National Institutes of Health Guide for the Care and Use of Experimental Animals and approved by the University of California San Diego Animal Care and Use Committee. C57BL/6J strain 10–15-week-old WT male and female mice (Jackson Laboratory) were used for fasting–refeeding studies. Mice were singly housed at 22–24 °C in a room with ambient humidity using a 12 h light–dark cycle with ad libitum access to standard chow diet and water. For experiments involving fasting and refeeding, food was removed either for 24 h or 6 h, then replaced for 24 h for refed conditions. Mouse blood glucose levels were measured using an Accu-Chek Aviva Plus Glucose Monitor. Food intake, body weight and blood glucose levels were monitored weekly throughout the experiments as previously described[18]. Sprague Dawley strain WT rats (Envigo) were used for primary neuron cultures. Timed pregnant female rats (embryonic days 13–16) were singly housed in a room with a 12 h light–dark cycle with ad libitum food, water access and environmental enrichment. Primary hippocampal and cortical neuron cultures were generated as described in the section below.

Caenorhabditis elegans strains and maintenance

All strains were maintained at 20 °C on nematode growth medium plates seeded with *E. coli* OP50 as previously described[82]. Hermaphrodites were used for all experiments, and males were only used for crossing. To label mitochondria in cholinergic motor neuron DA9, mitochondria matrix localization signal (as in pPD96.32) was fused with TagRFP expressed as extrachromosomal arrays. The microinjection mix contained Pitr-1pB::mito::TagRFP::let858 3′UTR (pYW217) at 30 ng μl^{-1} to label the mitochondria in DA9 neuron, Podr-1::gfp at 20 ng μl^{-1} to label the AWB/C neurons as the co-injection marker and Promega 1 kb DNA ladder as the filler. The hxk-1::7xgfp11 knock-in was generated by CRISPR–Cas9 using a pre-assembled Cas9 ribonucleoprotein complex[83] (Extended Data Fig. 2f). In brief, the injection mix contained 0.25 μg μl^{-1} *S. pyogenes* Cas9 (IDT), 0.1 μg μl^{-1} tracrRNA (IDT), 0.056 μg μl^{-1} crRNA, 25 ng μl^{-1} pre-melted double-stranded DNA repair template and 40 ng μl^{-1} PRF4 (rol-6 (su1006)) plasmid. The mix was injected into a strain that expresses the GFP1–10 fragment in the DA9 neuron and another neuron in the ventral cord[84]. Non-roller F_1 progeny from P_0 roller jackpot plates were screened by single-worm PCR. Homozygotes from the F_2 generation were verified by Sanger sequencing. The repair template contained 35 bp homology arms on both ends and a GSGGGG liker between hxk-1 and 7xgfp11. The repair template was synthesized as a Gblock by IDT (specific sequences are listed in Supplementary Table 1), amplified by PCR, gel-purified and further cleaned up with the MinElute PCR purification kit.

Primary neuronal culture

Primary neuron cultures were established from rat embryos (E18) as previously described[85]. Hippocampal and cortical neurons were plated at a density of 5–7 × 10^4 cells per cm^2 on round (12 mm diameter) coverslips (Carolina Biological Supplies) for imaging or on 6-well plates at 1–2 × 10^5 cells per cm^2 for biochemical assays. Before plating, coverslips and plates were coated with 20 μg ml^{-1} poly-L-lysine and 3.5 μg ml^{-1} laminin overnight at room temperature. Primary neuron cultures were maintained in Neurobasal medium containing 5 mM glucose, supplemented with B27, GlutaMAX and penicillin–streptomycin unless modified as specified. Glucose levels in neuron culture media were monitored every 24 h to maintain a concentration of 5 mM glucose. For neuron culture media containing 1 mM glucose, glucose levels were monitored every 12 h. Each independent experiment was performed with the preparation of new primary neuron cultures. For biochemical assays, cortical neurons were treated with 1 μM cytarabine (Ara-C) at 3 days in vitro (DIV) to prevent glia proliferation for 2 days. The Ara-C-containing medium was replaced with fresh neuron maintenance medium at 5 DIV. The primary neuron cultures were maintained for 11–17 DIV by replacing one-third of the culture medium with a fresh medium every 3 days. When indicated, hippocampal and cortical neurons were treated with Thiamet-G or OSMI-4 at a final concentration of 5 μM for 16–18 h. Primary neuron cultures were transfected with indicated plasmid DNA constructs using Lipofectamine 2000 for each experiment and imaged 2–3 days later. For each experiment, co-transfection efficiency of 80–90% (up to four plasmids) was confirmed retrospectively. Supplementary Table 1 contains detailed information about the reagents and materials used for primary neuron cultures.

Cell line culture

HEK293T, monkey kidney COS-7 and Neuro-2a cell lines were used to perform indicated experiments. The cell lines were obtained from American Type Culture Collection (ATCC) and were tested every 6 months for mycoplasma contamination using LookOut Mycoplasma PCR Detection Kit. To achieve consistency in cellular metabolic properties, the cell lines were used for no more than 15 passages. HEK293T cells were CRISPR-edited to endogenously tag HK1, as described in the section below. Both WT and CRISPR-edited HEK293T cells were maintained in DMEM containing 5 mM glucose, supplemented with penicillin (100 U ml^{-1})–streptomycin (100 μg ml^{-1})–L-glutamine (2 mM), 10% FBS at 37 °C in a 95% air, 5% CO_2 humidified incubator. For biochemistry experiments and respirometry measurements, HEK293T cells were plated on 6-well plates at a density of 6.3 × 10^4 cells per cm^2. For microscopy experiments, HEK293T cells were plated on round (12 mm diameter) coverslips at a density of 2.6 × 10^4 cells per cm^2. Plasmid DNA transfections were performed with calcium phosphate protocol[86] when HEK293T cells reached at least 30% confluency, using 0.5–1 μg of DNA per well. When indicated, HEK239T cells were treated with Thiamet-G at a final concentration of 10 μM for 16–18 h. COS-7 and Neuro-2a cell lines were maintained in DMEM containing 25 mM glucose, supplemented with penicillin (100 U ml^{-1})–streptomycin (100 μg ml^{-1})–L-glutamine (2 mM) and 10% FBS at 37 °C in a 95% air, 5% CO_2 humidified incubator. For microscopy experiments, COS-7 cells were plated on round (12 mm diameter) coverslips at a density of 2 × 10^4 cells per well and transfected with plasmid DNA (0.4–2.9 μg of DNA per well) confluency using the calcium phosphate protocol[86] when they reached 30%. Neuro-2a cells were transfected with plasmid DNA (2.5 μg DNA per well) at 50% confluency using Lipofectamine 3000 transfection reagent in Opti-MEM medium. Cells were lysed for biochemical analysis or processed for microscopy 2–3 days after transfection, as indicated for each experiment. Supplementary Table 1 contains detailed information about the reagents and materials used for cell line cultures.

Plasmid constructs

The following previously published or commercially available DNA constructs were used: vGLUT1–pHluorin[87] (a gift from Dr. Ghazal Ashrafi), mCherry[88] (a gift from Dr. Gentry Patrick), pRK5–Myc–OGA[89] and nucleocytoplasmic OGT (ncOGT)[90] (a gift from Gerald Hart laboratory, Johns Hopkins and the NHLBI P01HL107153 Core C4), mEGFP–PKM2[39] (a gift from Dr. Songon An), mCherry-mito-FKBP[91] and pDsRed2-Mito[18] (a gift from Thomas Schwarz), pAAV.CAG.GCaMP6s.WPRE.SV40[92] (a gift from Douglas Kim and GENIE Project; Addgene, plasmid 100844), Synapsin-cyto-mRuby3-iATPSnFR1.0[93] (a gift from Baljit Khakh; Addgene, plasmid 102557; http://n2t.net/addgene:102557; RRID: Addgene_102557), CMV-Hylight[30] (a gift from Richard Goodman; Addgene, plasmid 193447; http://n2t.net/addgene:193447; RRID: Addgene_193447), FLHKI-pGFPN3, TrHKI-pGFPN3 and FLHKII-pGFPN3[17] (a gift from Hossein Ardehali; Addgene, plasmids 21917, 21918 and 21920), (294)pcDNA3.1-myc-OGA(1–400) and (344) pcDNA3.1(+)-HA-nLaG6-(EAAAK)4-OGA(544–706)[22] (a gift from Christina Woo; Addgene, plasmids 168095 and 168197). The lentivirus packaging plasmids psPAX2 and pMD2.G were a gift from Didier Trono (Addgene, plasmids 12260 and 12259; http://n2t.net/addgene:12260; RRID: Addgene_12260; http://n2t.net/addgene:12259; RRID: Addgene_12259). Additionally, the shRNA plasmid against mouse HK1 and empty vector control were purchased from Sigma-Aldrich MISSION.

The following plasmids were generated in this study: T259A-HK1–GFP was PCR-amplified from WT HK1–GFP with the Thr259 to alanine mutation by using the In-Fusion HD Cloning Kit. WT T259A-HK1–BFP and FLAG–APEX2 were generated from WT T259A-HK1–GFP by excising GFP using ApaI and NotI digestion and replacing it with gene block containing TagBFP or FLAG–APEX2 (specific sequences are listed in Supplementary Table 1). Furthermore, pEGFP-FRB*:Tr-hHK1 (vector ID VB181221-1086jen), pEGFP-FRB*:Tr-T259A-hHK1 (vector ID VB181221-1158hep), HK1 shRNA-SYN-WT-HK1-mNeonGreen-mCherry (vector ID VB210910-1051quh) and HK1 shRNA-SYN-T259A-HK1-mNeonGreen-T2A-mCherry (vector ID VB210910-1046tmk) used in this study were constructed by VectorBuilder. The vector ID numbers can be used to retrieve detailed information.

CRISPR-mediated EGFP tagging of endogenous HK1 in HEK293T

To generate endogenously fluorescently tagged HK1 (with EGFP) expressing HEK293T cells (HEK293T-EGFP–HK1), single guide RNAs (sgRNAs) were designed to target the region between exon 18 and 3′ UTR of the human transcript HK1-202 (NM_000188). Candidate sgRNAs were designed by the CRISPR design tool from the Wellcome Sanger Institute. To confirm the on-target activity of the designed sgRNAs, we used Universal CRISPR Activity Assay (UCATM), a sgRNA activity detection system developed by Biocytogen. The targeting donor vector used in this study contained a PuroDeltatk-resistant cassette flanked by loxP sites in intron17 and a linker-EGFP cassette inserted before the TAA stop codon of the human HK1 gene. Thus, the fluorescent protein EGFP is fused to and under control of the endogenous HK1 promoter (Extended Data Fig. 3a). To introduce the sgRNA2 and targeting vector into the HEK293T cell line, electroporation was used. After the selection of cells for drug resistance and performing PCR, mixed positive clones were further electroporated with a Cre-expressing vector to remove the antibiotic-resistant cassette. Subsequently, 14 clones were picked and expanded in semisolid media. Finally, two homozygous clones were obtained by further genotyping characterization and PCR product sequencing.

C. elegans imaging and analysis

ST045849 was used to inhibit the OGT in *C. elegans*[21]. A 20 mM stock solution was prepared in DMSO and added to NGM media to achieve a final concentration of 50 µM. The media was poured into 12-well plates at a volume of 2 ml per well. The plate was left to dry overnight at room temperature with a loose cover. The following day, 50 µl of concentrated OP50 bacteria containing 50 µM ST045849 was added to each well. After the plate had dried for approximately 30 min, L2 worms were transferred onto the plate immediately and incubated at 20 °C. Worms at the larval L4 to adult transition stages were imaged the next day (approximately 24 h later). For the control group, the same amount of DMSO was added to both NGM and OP50.

For imaging, L4 animals were immobilized with 50 mM muscimol and mounted on 3% agarose pads. Animals oriented with the ventral side facing the coverslip were selected for imaging the cell body. Images were acquired on a VT-iSIM system (BioVision) built around a Leica Laser Safe DMi8 inverted scope with an HC PL APO ×63/1.40 Oil CS2 objective and an ORCA-Flash 4.0 camera (Hamamatsu). Emission filters 525/50 nm and 605/52 nm were used for 488 nm and 561 nm illumination, respectively. *Z*-stacks were acquired with 0.2 µm step size on an ASI-XYpZ Piezo stage. Images were taken sequentially for 488 nm and 561 nm at each *Z* position, and 400 ms exposure time was used for each channel. Image acquisition was controlled by the MetaMorph Advanced Confocal Acquisition software package. Maximum projections were generated in Fiji[94] from microscopy data. To calculate the ratio of HXK-1::7xSplitGFP intensity on mitochondria versus the cytoplasm in the cell body, all images were blinded and randomized. Mitochondria were traced manually in the TagRFP channel, and average intensities from the GFP channel in areas with mitochondria or without mitochondria were recorded. The auto-fluorescent signal from the surrounding area was selected as background and subtracted from the GFP intensity. The subtracted values were then used to calculate the mitochondrial to cytoplasmic ratio.

Brain slice immunohistochemistry

Immediately after the end of the fasting–refeeding experiments, mice were anaesthetised by inhalation of isoflurane and perfused transcardially first with ice-cold phosphate-buffered saline (PBS, pH 7.4) containing heparin (19.5 U ml^{-1}), followed by freshly prepared 4% paraformaldehyde (PFA) in PBS. Brains were extracted and post-fixed with 4% PFA solution overnight, rinsed with PBS, cryoprotected in 30% sucrose and embedded with Tissue-Tek O.C.T. compound for cryosectioning. Brain sections of 20 µm thickness were obtained using a cryostat. The sections were placed in Mouse-on-Mouse blocking solution (1 drop in 2.5 ml of 1× PBS) for 30 min at room temperature to reduce nonspecific binding. To further prevent nonspecific binding, the sections were incubated in blocking buffer (3% normal goat serum, 1% bovine serum albumin, 1% fish gelatin, 0.1% Triton X-100, 1× PBS, ddH$_2$O) for 1 h at room temperature. The sections were then incubated overnight at 4 °C with the following antibodies (see Supplementary Table 1 for detailed information about the antibodies) in the staining solution (10% blocking buffer, 0.1% Triton X-100, 1× PBS, ddH2O): rabbit anti-HK1 (1:500), mouse anti-pyruvate dehydrogenase (1:500) and chicken anti-NeuN (1:500). After washing with 1× PBS three times, the sections were incubated with secondary antibodies conjugated with Alexa Fluor 488, 568 and 647 (1:500 dilution for each) for 1 h at room temperature. The sections were then washed twice with 1× PBS before incubating with DAPI 4′,6-diamidino-phenyindole (1:1,000 in 1× PBS) for 10 min at room temperature to label nuclei. Lastly, the sections were washed twice with 1× PBS and mounted on Superfrost Plus Microscope slides and no. 1.5 rectangle Platinum Line cover glass using VECTASHIELD Vibrance antifade mounting medium. Images were acquired using both Zeiss Axio Imager Z2 upright microscope with ZEN pro Elements, and the fluorophores were excited using the 385 nm, 475 nm, 555 nm and 630 nm lines of the six-line (385 nm, 430 nm, 475 nm, 511 nm, 555 nm, 630 nm), Plan-Apochromat objective of ×20/0.4 objective, the camera used was AxioCam 712 mono, pixel size 3.45 µm × 3.45 µm, 1,388 × 1,040 pixels and Zeiss LSM 780 confocal laser scanning microscope, Plan-Apochromat ×100/1.40 Oil DIC M27 objective with the highly sensitive low dark noise PMTs (2×) and GaAsP (32×) array. Image acquisition settings were kept constant across different conditions and sections. A total of 27–30 hippocampal CA3 region images were acquired and analysed using Fiji/ImageJ software[94], and linear adjustments of brightness and contrast were made only for visualization purposes. To quantify co-localization between HK1 and mitochondria, first, all images were blinded and randomized, and then the Fiji/ImageJ plugin COLOC2 was used to calculate Manders' coefficients[95]. Indicated regions from mice hippocampus were used for this analysis. The calculated values were extracted, and statistically analysed using GraphPad Prism version 7.0 for Mac OS.

Immunocytochemistry

HEK293T and COS-7 cells were fixed with 4% PFA in 1× PBS for 10 min at room temperature. Fixed cells were washed three times with 1× PBS, followed by blocking with 0.5% saponin and 1% BSA in 1× PBS for 1 h at room temperature. The cells were then immunostained with primary antibodies at 4 °C overnight in blocking buffer. The primary antibodies used were rabbit anti-GFP, mouse anti-GFP, rabbit anti-Tomm20, rat anti-HA and chicken anti-myc (1:500 dilution for each) (see Supplementary Table 1 for detailed information about the antibodies). After washing cells three times with 1× PBS, they were incubated with secondary antibodies conjugated with Alexa Fluor dyes at 1:500 dilution for 1 h at room temperature. The secondary antibodies used were goat anti-rabbit Alexa Fluor 488, goat anti-chicken Alexa Fluor 405, goat anti-mouse Alexa Fluor 488, goat anti-rabbit Alexa Fluor 568 and goat anti-rat Alexa Fluor 647. Following another three washes with 1× PBS, coverslips were mounted using DAPI Fluoromount-G. Images were acquired using a Zeiss LSM 780 confocal laser scanning microscope equipped with Plan-Apochromat ×100/1.40 Oil DIC M27 objective.

Immunocytochemistry of 11–15 DIV disassociated primary neuron cultures was performed as previously described[18]. In brief, neurons expressing indicated plasmids were fixed with 4% PFA and 4% sucrose in 1× PBS for 10 min at room temperature. The fixed neurons were then washed three times in 1× PBS, followed by blocking in 1× GBD (10% goat serum, 1% BSA and 0.1% Triton X-100 in 1× PBS) for 1 h at room temperature. Primary antibodies were diluted in 1× GBD and incubated with the neurons overnight at 4 °C. Secondary antibodies were also diluted in 1× GBD and incubated with the neurons for 1 h at room temperature. The following primary and secondary antibodies were used: rabbit anti-HK1 (Invitrogen, 1:500) or rabbit anti-HK1 (Cell Signaling, 1:250) and goat anti-rabbit Alexa Fluor 647 (1:500). The coverslips were mounted using Fluoromount-G. Images were acquired using a Zeiss LSM 780 confocal laser scanning microscope equipped with a C-Apochromat ×40/1.20 W Korr FCS M27 objective. The image acquisition settings were kept consistent across different conditions and coverslips for HEK293T, COS-7 and primary neuron immunostaining. The acquired images were analysed using Fiji[94], and only linear adjustments of brightness and contrast were made for visualization purposes. All experiments were performed at least three times, and representative images are shown. Quantification of staining intensity and co-localization was performed on Fiji/ImageJ, and statistical analysis was conducted using GraphPad Prism version 7.0 for Mac OS.

Mitochondria isolation

Mitochondrial fractions were prepared from 11–15 DIV primary cortical neuron cultures or HEK293T cells, plated on 6-well plates, by homogenization in mitochondrial isolation buffer (10 mM Tris-HCl (pH 7.4), 10 mM KCl, 250 mM sucrose, 1 mM EDTA (pH 8.0), 1× Protease Inhibitor Cocktail Set III EDTA Free, 0.1 mM phenylmethylsulfonyl fluoride (PMSF), 4 µM Thiamet-G and 2 mM dithiothreitol (DTT)) and differential centrifugation. Each well containing cells (~1.5×10^7 cells per condition) was first washed with 1 ml ice-cold 1× PBS and then incubated with 330 µl of freshly prepared mitochondrial isolation buffer on ice for 10 min with gentle agitation. Cells were detached with a cell scraper and homogenized with 20–30 strokes using a tight-fitting B pestle in a 1 ml Dounce homogenizer. The homogenate was centrifuged at 700*g* for 10 min at 4 °C to pellet nuclei and large cell debris. Then, 20 µl of the first supernatant (input, containing mitochondria) was saved for western blot analysis as whole cell lysate. The supernatant was centrifuged again at 10,000*g* for 10 min at 4 °C to pellet the crude mitochondrial fraction. The second supernatant (cytoplasmic fraction) was collected and concentrated using 0.5 ml Centrifugal Filters, Ultracel-10K. Then, 50% of the mitochondrial fraction (20% for Extended Data Fig. 5k) and 50% of the cytoplasmic fraction (5% for Extended Data Fig. 5k) were loaded in SDS–PAGE and analysed by western blotting. For western blot analysis, samples were resuspended in 1× Laemmli sample buffer and denatured at 95 °C for 5 min before loading onto an SDS–PAGE. After separation, the proteins were transferred to nitrocellulose membranes and stained with primary or secondary antibodies as previously described[18]. Stripping buffer was used to reprobe the western blots with different antibodies, and blots were only reprobed after confirming the absence of the previous signal. Chemiluminescent detection was performed with SuperSignal West Dura Extended Duration Substrate. For quantitative western blot measurements, image exposure times were optimized for the linear range of detection using the Azure C600 Biosystem gel documentation system. All experiments were performed at least three times. The images were further analysed using Fiji gel analyser[94], using only linear adjustments of brightness and contrast for visualization.

The following antibodies (see Supplementary Table 1 for detailed information about the antibodies) were used for probing blots to analyse mitochondrial and cytoplasmic fractions: rabbit anti-HK1 (Invitrogen) at 1:500; rabbit anti-PKM2 at 1:500; mouse anti-PKM at 1:250; rabbit anti-Aldolase A at 1:250; mouse anti-Aldolase A at 1:500; mouse anti-PGK at 1:250; rabbit anti-GPI at 1:500; mouse anti-PFKM at 1:500; mouse anti-GAPDH at 1:1,000; mouse anti-PGAM1 at 1:500; mouse anti-NSE at 1:500, mouse anti-TPI at 1:500; rabbit anti-ATP5B at 1:1,000; mouse anti-tubulin alpha-4A chain at 1:1,000; mouse anti-actin at 1:2,000; mouse and rabbit anti-LAMP2 at 1:1,000; rabbit anti-Golgin-97 at 1:1,000; mouse anti-KDEL at 1:1,000; rabbit anti-PEX19 at 1:1,000; mouse anti-Lamin A at 1:1,000; rabbit anti-CKAP4 at 1:1,000; goat anti-mouse horseradish peroxidase at 1:2,000 and goat anti-rabbit horseradish peroxidase-conjugated peroxidase at 1:2,000.

HK1 release assay

To evaluate the release of HK1 from mitochondria as a function of G6P concentration, mitochondria were isolated from HEK239T cells (expressing WT or T259A-HK1–GFP together with OGT overexpression and 10 µM Thiamet-G treatment or under control conditions) using modified mitochondria isolation buffer (5 mM HEPES (pH 7.4), 250 mM sucrose, 5 mM D-glucose, 1× Protease Inhibitor Cocktail Set III EDTA Free, 0.1 mM PMSF, 2 mM DTT, 10 µM Thiamet-G, 40 mM *N*-acetyl-D-glucosamine), as described above. To perform the HK1 release assay, equal amounts of purified mitochondria were resuspended in a release buffer (5 mM $MgCl_2 \cdot 6H_2O$ added into modified mitochondria isolation buffer) containing 0 µM, 250 µM or 500 µM G6P (Fig. 6d). The samples were incubated for 30 min at room temperature. The mitochondria were pelleted by centrifugation at 10,000*g* for 10 min at 4 °C. The supernatant containing the HK1 fraction released by various concentrations of G6P (flowthrough) was collected. The mitochondrial pellet was resuspended in modified mitochondria isolation buffer and centrifuged again. The mitochondria and flowthrough samples were loaded into SDS–PAGE for western blot analysis and evaluated with indicated antibodies.

O-GlcNAcylation measurements

HEK293T or HEK293T-EGFP–HK1 cells were plated in a 6-well plate as mentioned above and transfected with the indicated plasmid constructs the next day. Then, 3 days after reaching confluency, cells were washed once with ice-cold 1× PBS containing 8 µM Thiamet-G and lysed in 500 µl buffer containing 2% NP-40 alternative, 50 mM Tris-HCl (pH 7.5), 150 mM NaCl, 1 mM EDTA, 40 mM *N*-acetyl-D-glucosamine, 8 mM Thiamet-G, 2 mM DTT, 0.1 mg ml^{-1} PMSF and protease inhibitor cocktail at 1:1,000. Lysates were centrifuged 10 min at 13,000*g* at 4 °C and the supernatants were collected. For immunoprecipitations of HK2–GFP, and HK1–GFP WT or GlcNAc site mutant (T259A), 2 µg of anti-GFP was incubated for 2 h at 4 °C with 500 µl of whole-cell lysates, then for 1 h at 4 °C with Protein A Sepharose beads. Beads were washed three times with lysis buffer and resuspended with 1× Laemmli buffer. Next, 80–90% of the immunoprecipitants were separated by SDS–PAGE and transferred to nitrocellulose membranes. For O-GlcNAcylation measurements, blots were first incubated with blocking buffer containing 3% BSA in 1× TBST, then probed with anti-O-GlcNAc antibody (RL2) overnight[96]. To demonstrate O-GlcNAc modification of endogenous HK1 in neurons, we immunoprecipitated O-GlcNAcylated proteins from mitochondrial fractions using 5 µg anti-O-GlcNAc (RL2) antibody and probed with Anti-HK1 antibody (Extended Data Fig. 3c,d). All buffers have to be made or added fresh and all steps mentioned above have to be done in the same day to preserve O-GlcNAcylation. The same blot was re-probed with rabbit anti-GFP used at 1:1,000, rabbit anti-HK1 (Invitrogen) used at 1:500 or rabbit anti-OGT antibody used at 1:1,000 after washing thoroughly and blocking with 5% non-fat milk in 1× PBST (1× PBS with 0.1% Tween20) for 1–2 h at room temperature. For quantitative western blot measurements, image exposure times were optimized for the linear range of detection using the Azure C600 Biosystem gel documentation system. The images were further analysed using the Fiji gel analyser function to quantify the intensity of each band.

Mass spectrometry analysis

HK1–GFP was immunoprecipitated from HEK293T cells as described above. HEK293T cells were treated either with 5 µM Thiamet-G or vehicle overnight. Then, 80–90% of each sample was separated by 7.5% Mini-PROTEAN TGX precast gel. The SimpleBlue-stained gel band corresponding to HK1–GFP as well as the control lane were excised, minced and prepared for mass spectrometry analysis as previously described[97]. In brief, the gel was cut into 1 mm × 1 mm cubes and destained three times by first washing with 100 µl of 100 mM ammonium bicarbonate for 15 min, followed by addition of the same volume of acetonitrile (ACN) for 15 min. The supernatant was removed and samples were dried in a speedvac. Samples were then reduced by mixing with 200 µl of 100 mM ammonium bicarbonate and 10 mM DTT and incubated at 56 °C for 30 min. The liquid was removed and 200 µl of 100 mM ammonium bicarbonate and 55 mM iodoacetamide was added to gel pieces and incubated at room temperature in the dark for 20 min. After the removal of the supernatant and one wash with 100 mM ammonium bicarbonate for 15 min, the same volume of ACN was added to dehydrate the gel pieces. The solution was then removed and samples were dried in a speedvac. For digestion, enough solution of ice-cold trypsin (0.01 µg µl^{-1}) in 50 mM ammonium bicarbonate was added to cover the gel pieces and set on ice for 30 min. After complete rehydration, the excess trypsin solution was removed, replaced with fresh 50 mM ammonium bicarbonate and left overnight at 37 °C. The peptides were extracted twice by the addition of 50 µl of 0.2% formic acid and 5% ACN with vortex mixing at room temperature for 30 min. The supernatant was removed and saved. A total of 50 µl of 50% ACN and 0.2% formic acid was added to the sample, which was vortexed again at room temperature for 30 min. The supernatant was removed and combined with the supernatant from the first extraction[97]. The combined extractions were analysed directly by liquid chromatography in combination with tandem mass spectroscopy using electrospray ionization.

Trypsin and gluc-digested peptides were analysed by ultra-high-pressure liquid chromatography coupled with tandem mass spectroscopy using nanospray ionization. The nanospray ionization experiments were performed using an Orbitrap fusion Lumos hybrid mass spectrometer (Thermo) interfaced with nano-scale reversed-phase ultra-high-pressure liquid chromatography machine (Thermo Dionex UltiMate 3000 RSLC nano System) using a 25 cm, 75 µm ID glass capillary packed with 1.7 µm C18 (130) BEHTM beads (Waters corporation). Peptides were eluted from the C18 column into the mass spectrometer using a linear gradient (5–80%) of ACN at a flow rate of 375 µl min^{-1} for 1 h. The buffers used to create the ACN gradient included buffer A (98% H_2O, 2% ACN, 0.1% formic acid) and buffer B (100% ACN, 0.1% formic acid). Mass spectrometry (MS1 survey scan using the orbitrap detector (mass range (m/z): 400–1,500 (using quadrupole isolation)), 60,000 resolution setting, spray voltage of 2,400 V, ion transfer tube temperature of 285 °C, AGC target of 400,000 and maximum injection time of 50 ms) was followed by data-dependent scans (top speed for most intense ions, with charge state set to only include +2–5 ions, and 5 s exclusion time, while selecting ions with minimal intensities of 50,000 at in which the collision event was carried out with high energy collision cell dissociation (HCD collision energy of 30%), and the fragment masses where analysed in the ion trap mass analyser (with ion trap scan rate of turbo, first mass m/z was 100, AGC target 5,000 and maximum injection time of 35 ms), followed by electron transfer dissociation (ETD collision energy of 25%, and EThcD setting active (SA collision energy of 25%)), and the fragment masses where analysed in the ion trap mass analyser (with ion trap scan rate of turbo, first mass m/z was 100, AGC target of 5,000 and maximum injection time of 35 ms). Data analyses were carried out using Byonic (Protein Metrics) or Peaks v.8.5 (Bioinformatics Solutions).

Structural analysis of HK1 using computational modelling

An X-ray crystallography structure of HK1 (PDB 1CZA) was used for the structural analysis[25]. The secondary structure of the unmodelled portion of HK1 (amino acid residues 1–15) was predicted with Iterative Threading Assembly Refinement[98] and manually appended to the crystal structure using Visual Molecular Dynamics. The full-length structure was then minimized using stochastic gradient descent and equilibrated for 200 ns in explicit water. The equilibrated HK1 structure was then used to construct a variant with the T259 O-GlcNAc post-translational modification using Charmm-GUI's standard procedures[99]. The O-GlcNAc modified variant of HK1 was minimized using stochastic gradient descent and equilibrated for 200 ns in water and counter ions at a concentration of 0.15 M. Finally, a conformational search was performed using REST2 in Nanoscale Molecular Dynamics[27,100]. The REST2 simulations were performed with 30 replicas over a linear temperature range from 300 K to 500 K. The number of exchange attempts was 5,000, with 20,000 integration steps between each exchange for 200 ns for each of the 30 replicas, totalling 6 µs of sampling.

To determine how T259 O-GlcNAcylation alters HK1 function, Poisson–Boltzmann calculations were performed using the APBS software suite[101] with the following parameters. First, the linearized Poisson–Boltzmann equation was solved with the single Debye–Huckel boundary condition and the *smol* option for representation of the molecular surface. The *cglen* and *fglen* options were chosen to ensure a 1 Å resolution electrostatic potential grid. Temperature and ion concentrations were set at 300 K and 0.15 M. The protein and solvent dielectric constants were set to 12.0 and 78, respectively. The radius of the solvent was set to that of water, 1.4 Å. Finally, the atomic radii and charges were set as defined in the CHARMM36 force field[102].

G6P measurements

To measure G6P levels, HEK293T cells were transfected with indicated constructs and detached from 6-well plates with a cell scraper. Cell lysates were prepared in 500 µl ice-cold 1× PBS using 25G 5/8 inch and 30G 1/2 inch syringe needles. Lysates were centrifuged for 5 min at 13,000*g* and 4 °C, and the supernatants were collected. The supernatant was filtered through Amicon Ultra-0.5 ml centrifugal filters (Ultracel-10K) and centrifuged for 15 min at 14,000*g* and 4 °C. The concentrated samples were used to measure total protein concentrations with a BCA Protein Assay and the deproteinized samples were used to measure G6P levels following the protocol provided in the G6P Assay

Kit. Colorimetric measurements were made at room temperature using a Spark 20M reader. Expression levels of WT or GlcNAc site mutant (T259A) HK1–GFP were analysed by western blotting from cell lysates.

Respirometry measurements with HEK293T

OCR and ECAR were measured using an Agilent Seahorse XFe96 Analyzer with a Seahorse XF Mito Stress Test and Seahorse XF Real-Time ATP Rate protocol from HEK293T cells. HEK239T cells were initially cultured on 6-well plates as described above; after 16–18 h of transfection, cells were re-plated on XF96e plates at 2.5×10^3 mm^{-2} density. After 2–3 h of replating, cells were treated with 10 µM OGA inhibitor Thiamet-G or vehicle control (DMSO) overnight. For respirometry measurements, the DMEM was exchanged with XF DMEM base medium (pH 7.4) with no phenol red supplemented with 5 mM glucose and 1 mM pyruvate. NucBlue Live Cell Stain was included to stain nuclei for cell counting immediately after the assay. Respiration was measured under basal conditions as well as after injections of 2 µM (for ATP production rate assay) or 0.5 µM (for mitochondria stress test) oligomycin, 0.5 µM FCCP and 0.5 µM rotenone/antimycin A. To recruit HK1 to the mitochondria surface using a chemically induced dimerization strategy[91] (Fig. 5e,f), AP21967 was applied at a final concentration of 500 nM to HEK239T cells for 15–20 min before respirometry measurements. ATP production rates were calculated according to the protocol provided by Agilent. Basal and maximal OCR as well as ECAR values were plotted after cell count normalization with FluxNorm Normalization, with cell counts done by FluxNorm[51].

Verification of HK1 knockdown with shRNA and rescue

For the HK1 knockdown experiments, 14 shRNA constructs from the Sigma MISSION shRNA library were screened. The most effective shRNA construct (TRCN0000297076) was selected and subsequently used to examine the HK1 knockdown efficiency. Given that the target sequence was conserved between mouse and rat HK1, the knockdown efficiency was first validated in Neuro-2a cells. The specificity of the HK1-shRNA construct was verified by co-expressing shRNA-resistant human WT or T259A-HK1–GFP for 3 days and then measuring the level of GFP signal from cell lysates (Extended Data Fig. 1b,c). After confirming the mouse HK1 knockdown efficiency, the HK1-shRNA construct was further characterized in rat primary neuron cultures. Rat hippocampal neurons were transfected with either TRC2 pLKO.5-puro empty vector control plasmid DNA or HK1-shRNA construct together and Mito-DsRed. Given the half-life of HK1 protein was estimated to be ~72 h[103], the shRNA construct was expressed in rat neurons for 3 days, allowing efficient knockdown of endogenous HK1 to be achieved. The efficiency of rat HK1 knockdown was verified retrospectively for each transfection by immunocytochemistry using an antibody against endogenous HK1 (Extended Data Fig. 4f,g). shRNA-resistant human GFP or BFP-tagged WT HK1 and T259A O-GlcNAc silent base mutation constructs were used together with the shRNA construct to maintain endogenous HK1 levels for all experiments (Extended Data Fig. 4f,g).

Live HEK293T cell imaging and analysis

HEK293T cells were transfected with a plasmid expressing Tom20–mCherry–FKBP[91] and FRB-Tr-HK1–GFP. After 24 h, cells were imaged using a Zeiss LSM 780 confocal laser scanning microscope equipped with a C-Apochromat ×40/1.20 W Korr FCS M27 objective with excitation at 488 nm and 561 nm separately. To investigate the time course of rapalog (AP21967)-induced dimerization, cells were treated with 500 nM AP21967 or DMSO as a vehicle control, and live-cell imaging was performed for 20 min. It was found that 10–15 min of AP21967 treatment was sufficient to induce HK1 recruitment to mitochondria. HEK293T cells were continuously perfused at 0.2–0.25 ml min^{-1} with Hibernate E low fluorescent, 5 mM glucose during image acquisition at 37 °C. Time-lapse images were acquired every 5 s at <1.5% laser power for each channel to minimize phototoxicity.

Live neuron imaging and analysis

vGLUT1–pH, iATPSnFR, HYlight and GCaMP live imaging with electrical stimulation. Primary hippocampal neurons were transfected with indicated DNA constructs using Lipofectamine 2000. Live-cell imaging of neurons was performed 2–3 days after transfections, at 11–14 DIV. Coverslips were mounted on a stimulation chamber with laminar flow for perfusion and imaged at 37 °C using a Zeiss LSM 780 laser scanning confocal microscope equipped with a heated stage and C-Apochromat ×40/1.20 W Korr FCS M27 objective with a highly sensitive low dark noise PMTs (2×) and GaAsP (32×) array. Laser power was set to <1% for each channel to minimize phototoxicity during time-lapse image acquisition. For all experiments, neurons were continuously perfused at 0.2–0.25 ml min^{-1} with modified Tyrode buffer (50 mM HEPES (pH 7.4), 119 mM NaCl, 2.5 mM KCl, 2 mM $CaCl_2$, 2 mM $MgCl_2$, 5 mM D-glucose, 2 mM pyruvate and 2 mM lactate, supplemented with 0.01 mM CNQX, 0.05 mM APV to suppress postsynaptic responses), pH measured at 37 °C. Trains of APs were evoked by current pulses of 100 mA, at 10 Hz for 10 s with 5 min of recovery between runs for live-cell imaging to measure synaptic vesicle recycling rates with vGLUT1–pH (pHluorin-tagged vesicular glutamate transporter 1)[104], calcium dynamics with GCaMP6s, ATP levels with iATPSnFR[93] and FBP levels with HYlight[30] sensors. For these measurements, endogenous HK1 was knocked down with shRNA and rescued with BFP-tagged or FLAG-tagged WT HK1 and T259A-HK1 to avoid overexpression. The stimulus pattern was generated with an Arduino connected to an isolated bipolar stimulator.

For vGLUT1–pH imaging, time-lapse movies were acquired from 11–14 DIV neurons for a total of 120 s at 10 Hz. For each imaging session, the first pre-stimulus fluorescence baseline (F_0) measurements were performed for 20 s in the absence of electrical activity, and then APs were evoked by electrical field stimulation (100 mA, 10 Hz, 100 APs). At the end of experiments, neurons were perfused with Tyrode buffer containing 50 mM NH_4Cl at pH 7.4, which rapidly equilibrates pH and increases the vGLUT1–pH signal, and imaging continued at 1 s intervals to obtain an F_{max} value for each imaged axonal segment. When indicated, 1 µM TTX was added to the neuron maintenance media right after transfection with WT or T259A-HK1–BFP constructs to preserve ATP use owing to spontaneous neuronal activity. Then, 2 h before live imaging, TTX was removed and washed off twice using culture media.

For calcium imaging, time-lapse movies were acquired from 11–12 DIV neurons expressing GCaMP6s[92] and the indicated HK1 constructs for a total of 30 s at 10 Hz. For each imaging session, first, pre-stimulus fluorescence baseline (F_0) measurements were performed for 5 s in the absence of electrical activity and then APs were evoked by electrical field stimulation (100 mA, 10 Hz, 100 APs). At the end of each experiment, the neurons were perfused with Tyrode buffer containing 50 mM KCl to achieve a maximal response (F_{max}) for each imaged axonal segment. Neurons that did not respond to KCl stimulation were excluded from the analysis.

Images were analysed using the Fiji plugin Time Series Analyzer (v.3.0). Approximately 2 µm regions of interest from 8–11 neurons corresponding to presynaptic boutons were selected for image analysis. ΔF values for vGLUT1–pH and GCaMP6s images were calculated as previously described after background substructions[87]. F_0 values were defined by averaging data points from the pre-stimulus period, and F_{max} values were determined by averaging data points following NH_4Cl application for vGLUT1–pH and KCl application for GCaMP6s images. Endocytic time constants were calculated by fitting the fluorescent change after the electrical stimulus to a single exponential decay[104].

For cytoplasmic ATP level measurements, single-wavelength genetically encoded fluorescent sensor mRuby-iATPSnFR$^{1.0}$ was used (Synapsin-cyto-mRuby3-iATPSnFR$^{1.0}$)[93]. Neurons were transfected with shRNA-resistant BFP-tagged WT or T259A-HK1, shRNA-HK1 and mRuby-iATPSnFR$^{1.0}$ plasmids. Time-lapse movies were acquired from 13–14 DIV neurons for a total of 10–15 min at 0.1–0.2 Hz using 488 nm, 568 nm and 405 nm lasers for excitation. In 2-DG and oligomycin experiments, 5 mM glucose in the Tyrode buffer (50 mM HEPES (pH 7.4), 119 mM NaCl, 2.5 mM KCl, 2 mM $CaCl_2$, 2 mM $MgCl_2$, 5 mM D-glucose, 2 mM pyruvate and 2 mM lactate) was replaced with 5 mM 2-DG, and 2 µM oligomycin was added during live-cell imaging. For each imaging session, first, pre-stimulus fluorescence baseline (F_0) measurements were performed for 2 min in the absence of electrical activity as a control and then APs were evoked by field stimulation (100 mA,10 Hz, 100 AP as indicated). Changes in mRuby-iATPSnFR$^{1.0}$ fluorescence ($\Delta F/F_0$) were calculated by dividing the fluorescent intensity differences between frames with pre-stimulus intensity for each stimulation. For each neuron, axonal processes (<150 µm away from the soma) were selected for image analysis. $\Delta F/F_0$ for mRuby and iATPSnFR$^{1.0}$ channels were plotted independently without the ratiometric calculations for each condition for the mRuby-iATPSnFR$^{1.0}$ sensor data.

For FBP level measurements with the HYlight sensor, hippocampal neurons were transfected with shRNA-resistant FLAG-tagged WT or T259A-HK1, HK1-shRNA and HYlight, and imaged 2 days after transfection at 11–12 DIV. Before the beginning of image acquisition, the neurons were pre-equilibrated with Tyrode buffer perfusion for 5 min in the stimulation chamber. Then, 5 mM glucose in the Tyrode buffer was replaced with 5 mM of 2-DG for the indicated condition in Fig. 5d. For each imaging session, first pre-stimulus fluorescence baseline (R_0) measurements were performed for 3 min in the absence of electrical activity as a control and then APs were evoked by field stimulation (100 mA, 10 Hz, 100 APs). Time-lapse movies from neurons expressing HYlight were acquired as described previously[30] for 10 min. In brief, the neuron images were acquired for each time point by using 488 nm and 405 nm lasers for excitation and emission detection ranges at 498–551 nm. The HYlight fluorescence ratio was calculated from individual axons. Then the normalized HYlight emission induced by 488 nm and 405 nm excitations ($\Delta R/R_0$) was calculated as a readout of temporal changes in FBP level by dividing the HYlight intensity data points by the pre-stimulus intensity (R_0).

Glucose level-dependent cytoplasmic and mitochondrial HK1 imaging. For live-cell imaging, endogenous HK1 was knocked down with shRNA, and then rescued with GFP-tagged WT and T259A-HK1 to avoid overexpression. Primary hippocampal neurons were transfected with indicated DNA constructs using Lipofectamine 2000. Live-cell imaging of neurons was performed 2–3 days after transfections at 11–14 DIV. The Yokogawa W1 SoRa scan head on a Nikon Ti-2E microscope equipped with NIS Elements software and a Photometrics Prime 95B camera was used in SoRa mode with a ×2.8 zoom lens. The fluorophores were excited using the 488 nm and 561 nm lines of a six-line (405 nm, 445 nm, 488 nm, 515 nm, 561 nm, and 640 nm) LUN-F-XL laser engine. For simultaneous acquisition, a quad bandpass filter (Chroma ZET405/488/561/640mv2) was placed in the emission path of the W1 scan head, and the emission was split with a Cairn TwinCam with a 580LP filter. The GFP emission was reflected and passed through a 514/30 BP filter onto camera two. The mCherry fluorescence was passed through a 617/73 and an additional 600/50 filter to camera one. Camera alignment was carried out by parking the W1 disk and projecting transmitted light through the pinholes of the disk onto both cameras. The image from camera two of the pinholes was shifted relative to camera one until the patterns matched at 1.200% zoom. An Okolab Bold Line stage-top incubator that was designed to fit in the piezo *Z*-stage (MadCity Labs) was used to maintain 37 °C and 5% CO_2. For all the experiments, neurons were continuously perfused with 0 mM (also containing 1 mM lactate and pyruvate), 1 mM (also containing 1 mM lactate and pyruvate), 2 mM or 5 mM glucose (when indicated with 5 µM OSMI-4) containing Hibernate E low fluorescent imaging media as indicated. Distal axons were selected for live-cell imaging. Images were analysed using the Fiji intensity plot function.

Multi-electrode array recordings and analysis

Rat cortical neurons were cultured at a density of 85,000 neurons per well on CytoView 24-well MEA plates (Axion Biosystems) for 14–17 DIV. Before cell plating, each well was prepared by coating with a 0.1% poly(ethyleneimine) solution (Polyscience) in borate buffer (pH 8.4) for 1 h at room temperature. After coating, wells were washed four times with water and left to air dry overnight. Additionally, 2 h before neuron plating, wells were coated with 20 µg ml^{-1} laminin. Lentiviral transduction was used to deliver HK1-shRNA and either WT HK1–GFP or T259A-HK1–GFP into cells, along with a cell filler mCherry under the control of the human synapsin promoter to ensure neuron-specific expression. To produce lentiviruses, cDNA encoding the gene of interest was co-transfected with the envelope plasmid pMD2.G and the packaging plasmid psPAX2 into HEK293T cells using TransIT-LT1 transfection reagent in Opti-MEM medium. Then, 18 h after transfection, the medium was replaced with complete DMEM HEK293T cell culture medium and the virus supernatants were collected after 48 h. The neurons were transduced with indicated lentiviral particles at a concentration of 7×10^5 IFU ml^{-1} for 3 days, achieving a transduction efficiency of >95%. Recordings were carried out on the Maestro MEA platform using AxIS navigator (Axion Biosystems) with a 200 Hz to 3 kHz bandpass filter. Spike detection was performed using an adaptive threshold set to six times the standard deviation of the estimated noise on each electrode. Each plate was allowed to acclimate to the Maestro instrument for 3–5 min before recordings. Following acclimatization, a 10–15 min recording session was conducted to assess the mean firing rates and network burst frequencies. Multi-electrode data analysis was performed using the Neural Metrics Tool (Axion Biosystems), and an active electrode was considered once five spikes occurred over a 1 min period (five spikes per min). Network bursts were identified in the data recorded from each individual electrode using an inter-spike interval threshold requiring a minimum number of five spikes with a maximum inter-spike interval of 100 ms. Network bursts were defined as having a minimum number of 50 spikes across an entire well with a maximum inter-spike interval of 100 ms and a minimum percentage of participating electrodes of 35%.

Statistics and reproducibility

Throughout the paper, data are expressed as mean ± s.e.m. unless otherwise noted. All *P* values and number of replicas are indicated in the figure legends for each experiment. Data collection and analysis were performed blind to the conditions of the experiments. The order of data acquisition was randomized to prevent bias. No data were excluded from the analyses. All experiments were replicated with three biological replicates. No statistical methods were used to pre-determine sample sizes but our sample sizes are similar to those reported in previous publications[18,43,44,69]. Statistical analysis was performed with GraphPad Prism v.7.0 for Mac OS. Data were tested for normality, and appropriate statistical tests were subsequently chosen based on the results. The Mann–Whitney *U*-test was used to determine the significance of differences between two unpaired conditions. Multiple conditions were compared by Kruskal–Wallis nonparametric ANOVA test, which was followed by Dunn's multiple comparisons test or by one-way ANOVA with post hoc Tukey's test as appropriate to determine the significance of differences across every condition relative to the control condition.

Resource availability

All biological resources and tools are either available from commercial sources (see Supplementary Table 1 for detailed information) or the lead contact. Further information and requests for resources should be directed and will be fulfilled by the lead contact.

Reporting summary

Further information on research design is available in the Nature Portfolio Reporting Summary linked to this article.

Data availability

Source data are provided with this paper.

Code availability

Agilent Seahorse XF96e Metabolic Flux Analyzer data normalization is performed with the custom-written macro 'FluxNormalyzer', available at https://doi.org/10.5281/zenodo.11111133 (ref. 105). The electrical field stimulation code is available at https://doi.org/10.5281/zenodo.11462693 (ref. 106). HK1 structure simulation data are available at https://doi.org/10.5281/zenodo.11462797 (ref. 107). Any additional information required to reanalyze the data reported in this paper is available from the lead contact upon request.

References

1. Herrero Martin, J. C. et al. An ETFDH-driven metabolon supports OXPHOS efficiency in skeletal muscle by regulating coenzyme Q homeostasis. *Nat. Metab.* **6**, 209–225 (2024).
2. Ho, T., Potapenko, E., Davis, D. B. & Merrins, M. J. A plasma membrane-associated glycolytic metabolon is functionally coupled to K_{ATP} channels in pancreatic α and β cells from humans and mice. *Cell Rep.* **42**, 112394 (2023).
3. Hong, M. et al. Cardiac ATP-sensitive K^+ channel associates with the glycolytic enzyme complex. *FASEB J.* **25**, 2456–2467 (2011).
4. Patrick, M. et al. Metabolon formation regulates branched-chain amino acid oxidation and homeostasis. *Nat. Metab.* **4**, 1775–1791 (2022).
5. Puchulu-Campanella, E. et al. Identification of the components of a glycolytic enzyme metabolon on the human red blood cell membrane. *J. Biol. Chem.* **288**, 848–858 (2013).
6. Welch, G. R. The living cell as an ecosystem: hierarchical analog and symmetry. *Trends. Ecol. Evol.* **2**, 305–309 (1987).
7. Pedley, A. M., Pareek, V. & Benkovic, S. J. The purinosome: a case study for a mammalian metabolon. *Annu. Rev. Biochem.* **91**, 89–106 (2022).
8. Alam, M. T. et al. The self-inhibitory nature of metabolic networks and its alleviation through compartmentalization. *Nat. Commun.* **8**, 16018 (2017).
9. Srere, P. A. The metabolon. *Trends Biochem. Sci.* **10**, 109–110 (1985).
10. Crane, R. K. & Sols, A. The association of hexokinase with particulate fractions of brain and other tissue homogenates. *J. Biol. Chem.* **203**, 273–292 (1953).
11. Tuttle, J. P. & Wilson, J. E. Brain hexokinase: a kinetic comparison of soluble and particulate forms. *Biochim. Biophys. Acta* **212**, 185–188 (1970).
12. Wilson, J. E. Brain hexokinase. A proposed relation between soluble-particulate distribution and activity in vivo. *J. Biol. Chem.* **243**, 3640–3647 (1968).
13. Wilson, J. E. Isozymes of mammalian hexokinase: structure, subcellular localization and metabolic function. *J. Exp. Biol.* **206**, 2049–2057 (2003).
14. Vaidyanathan, K., Durning, S. & Wells, L. Functional O-GlcNAc modifications: implications in molecular regulation and pathophysiology. *Crit. Rev. Biochem. Mol. Biol.* **49**, 140–163 (2014).
15. Lagerlof, O. et al. The nutrient sensor OGT in PVN neurons regulates feeding. *Science* **351**, 1293–1296 (2016).
16. Harwood, K. R. & Hanover, J. A. Nutrient-driven O-GlcNAc cycling—think globally but act locally. *J. Cell Sci.* **127**, 1857–1867 (2014).
17. Sun, L., Shukair, S., Naik, T. J., Moazed, F. & Ardehali, H. Glucose phosphorylation and mitochondrial binding are required for the protective effects of hexokinases I and II. *Mol. Cell. Biol.* **28**, 1007–1017 (2008).
18. Pekkurnaz, G., Trinidad, J. C., Wang, X., Kong, D. & Schwarz, T. L. Glucose regulates mitochondrial motility via Milton modification by O-GlcNAc transferase. *Cell* **158**, 54–68 (2014).
19. Silver, I. A. & Erecinska, M. Extracellular glucose concentration in mammalian brain: continuous monitoring of changes during increased neuronal activity and upon limitation in oxygen supply in normo-, hypo-, and hyperglycemic animals. *J. Neurosci.* **14**, 5068–5076 (1994).
20. Basu, H. et al. FHL2 anchors mitochondria to actin and adapts mitochondrial dynamics to glucose supply. *J. Cell Biol.* **220**, e201912077 (2021).
21. Taub, D. G., Awal, M. R. & Gabel, C. V. O-GlcNAc signaling orchestrates the regenerative response to neuronal injury in *Caenorhabditis elegans*. *Cell Rep.* **24**, 1931–1938.e3 (2018).
22. Ge, Y. et al. Target protein deglycosylation in living cells by a nanobody-fused split O-GlcNAcase. *Nat. Chem. Biol.* **17**, 593–600 (2021).
23. Ramirez, D. H. et al. Engineering a proximity-directed O-GlcNAc transferase for selective protein O-GlcNAcylation in cells. *ACS Chem. Biol.* **15**, 1059–1066 (2020).
24. Ramirez, D. H., Ge, Y. & Woo, C. M. O-GlcNAc engineering on a target protein in cells with nanobody-OGT and nanobody-splitOGA. *Curr. Protoc.* **1**, e117 (2021).
25. Aleshin, A. E. et al. Crystal structures of mutant monomeric hexokinase I reveal multiple ADP binding sites and conformational changes relevant to allosteric regulation. *J. Mol. Biol.* **296**, 1001–1015 (2000).
26. Jo, S. & Jiang, W. A generic implementation of replica exchange with solute tempering (REST2) algorithm in NAMD for complex biophysical simulations. *Comput. Phys. Commun.* **197**, 304–311 (2015).
27. Wang, L., Friesner, R. A. & Berne, B. J. Replica exchange with solute scaling: a more efficient version of replica exchange with solute tempering (REST2). *J. Phys. Chem. B* **115**, 9431–9438 (2011).
28. Rose, I. A. & Warms, J. V. Mitochondrial hexokinase. Release, rebinding, and location. *J. Biol. Chem.* **242**, 1635–1645 (1967).
29. Desousa, B. R. et al. Calculation of ATP production rates using the Seahorse XF Analyzer. *EMBO Rep.* **24**, e56380 (2023).
30. Koberstein, J. N. et al. Monitoring glycolytic dynamics in single cells using a fluorescent biosensor for fructose 1,6-bisphosphate. *Proc. Natl Acad. Sci. USA* **119**, e2204407119 (2022).
31. Wolfe, A. D. et al. Local and dynamic regulation of neuronal glycolysis in vivo. *Proc. Natl Acad. Sci. USA* **121**, e2314699121 (2024).
32. Diaz-Garcia, C. M. et al. Neuronal stimulation triggers neuronal glycolysis and not lactate uptake. *Cell Metab.* **26**, 361–374.e4 (2017).
33. Huh, W. K. et al. Global analysis of protein localization in budding yeast. *Nature* **425**, 686–691 (2003).
34. Jang, S. et al. Phosphofructokinase relocalizes into subcellular compartments with liquid-like properties in vivo. *Biophys. J.* **120**, 1170–1186 (2021).
35. Jin, M. et al. Glycolytic enzymes coalesce in G bodies under hypoxic stress. *Cell Rep.* **20**, 895–908 (2017).
36. Jang, S. et al. Glycolytic enzymes localize to synapses under energy stress to support synaptic function. *Neuron* **90**, 278–291 (2016).
37. Miura, N. et al. Spatial reorganization of *Saccharomyces cerevisiae* enolase to alter carbon metabolism under hypoxia. *Eukaryot. Cell* **12**, 1106–1119 (2013).
38. Noree, C. et al. A quantitative screen for metabolic enzyme structures reveals patterns of assembly across the yeast metabolic network. *Mol. Biol. Cell* **30**, 2721–2736 (2019).
39. Kohnhorst, C. L. et al. Identification of a multienzyme complex for glucose metabolism in living cells. *J. Biol. Chem.* **292**, 9191–9203 (2017).
40. Schmitt, D. L. & An, S. Spatial organization of metabolic enzyme complexes in cells. *Biochemistry* **56**, 3184–3196 (2017).

41. Ehsani-Zonouz, A., Golestani, A. & Nemat-Gorgani, M. Interaction of hexokinase with the outer mitochondrial membrane and a hydrophobic matrix. *Mol. Cell. Biochem.* **223**, 81–87 (2001).
42. Skaff, D. A., Kim, C. S., Tsai, H. J., Honzatko, R. B. & Fromm, H. J. Glucose 6-phosphate release of wild-type and mutant human brain hexokinases from mitochondria. *J. Biol. Chem.* **280**, 38403–38409 (2005).
43. Rangaraju, V., Calloway, N. & Ryan, T. A. Activity-driven local ATP synthesis is required for synaptic function. *Cell* **156**, 825–835 (2014).
44. Ashrafi, G., Wu, Z., Farrell, R. J. & Ryan, T. A. GLUT4 mobilization supports energetic demands of active synapses. *Neuron* **93**, 606–615.e3 (2017).
45. Yang, X. & Qian, K. Protein *O*-GlcNAcylation: emerging mechanisms and functions. *Nat. Rev. Mol. Cell Biol.* **18**, 452–465 (2017).
46. De Jesus, A. et al. Hexokinase 1 cellular localization regulates the metabolic fate of glucose. *Mol. Cell* **82**, 1261–1277.e9 (2022).
47. Singh, J. P. et al. O-GlcNAcase targets pyruvate kinase M2 to regulate tumor growth. *Oncogene* **39**, 560–573 (2020).
48. Yi, W. et al. Phosphofructokinase 1 glycosylation regulates cell growth and metabolism. *Science* **337**, 975–980 (2012).
49. Nie, H. et al. O-GlcNAcylation of PGK1 coordinates glycolysis and TCA cycle to promote tumor growth. *Nat. Commun.* **11**, 36 (2020).
50. Rexach, J. E. et al. Dynamic *O*-GlcNAc modification regulates CREB-mediated gene expression and memory formation. *Nat. Chem. Biol.* **8**, 253–261 (2012).
51. Yu, S. B., et al. Neuronal activity-driven O-GlcNAcylation promotes mitochondrial plasticity. *Dev. Cell* **59**, 2143–2157 (2024).
52. Khidekel, N. et al. Probing the dynamics of *O*-GlcNAc glycosylation in the brain using quantitative proteomics. *Nat. Chem. Biol.* **3**, 339–348 (2007).
53. Rexach, J. E., Clark, P. M. & Hsieh-Wilson, L. C. Chemical approaches to understanding *O*-GlcNAc glycosylation in the brain. *Nat. Chem. Biol.* **4**, 97–106 (2008).
54. Agrawal, A., Pekkurnaz, G. & Koslover, E. F. Spatial control of neuronal metabolism through glucose-mediated mitochondrial transport regulation. *eLife* **7**, e40986 (2018).
55. Garde, A. et al. Localized glucose import, glycolytic processing, and mitochondria generate a focused ATP burst to power basement-membrane invasion. *Dev. Cell* **57**, 732–749.e7 (2022).
56. Castellana, M. et al. Enzyme clustering accelerates processing of intermediates through metabolic channeling. *Nat. Biotechnol.* **32**, 1011–1018 (2014).
57. Conrado, R. J., Varner, J. D. & DeLisa, M. P. Engineering the spatial organization of metabolic enzymes: mimicking nature's synergy. *Curr. Opin. Biotechnol.* **19**, 492–499 (2008).
58. Brandina, I. et al. Enolase takes part in a macromolecular complex associated to mitochondria in yeast. *Biochim. Biophys. Acta* **1757**, 1217–1228 (2006).
59. Araiza-Olivera, D. et al. A glycolytic metabolon in *Saccharomyces cerevisiae* is stabilized by F-actin. *FEBS J.* **280**, 3887–3905 (2013).
60. An, S., Parajuli, P., Kennedy, E. L. & Kyoung, M. Multi-dimensional fluorescence live-cell imaging for glucosome dynamics in living human cells. *Methods Mol. Biol.* **2487**, 15–26 (2022).
61. Opperdoes, F. R. & Borst, P. Localization of nine glycolytic enzymes in a microbody-like organelle in *Trypanosoma brucei*: the glycosome. *FEBS Lett.* **80**, 360–364 (1977).
62. Wojtas, K., Slepecky, N., von Kalm, L. & Sullivan, D. Flight muscle function in *Drosophila* requires colocalization of glycolytic enzymes. *Mol. Biol. Cell* **8**, 1665–1675 (1997).
63. Sullivan, D. T. et al. Analysis of glycolytic enzyme co-localization in *Drosophila* flight muscle. *J. Exp. Biol.* **206**, 2031–2038 (2003).
64. Diaz-Garcia, C. M. & Yellen, G. Neurons rely on glucose rather than astrocytic lactate during stimulation. *J. Neurosci. Res.* **97**, 883–889 (2019).
65. Li, H. et al. Neurons require glucose uptake and glycolysis in vivo. *Cell Rep.* **42**, 112335 (2023).
66. Baeza-Lehnert, F. et al. Non-canonical control of neuronal energy status by the Na^+ pump. *Cell Metab.* **29**, 668–680.e4 (2019).
67. Pathak, D. et al. The role of mitochondrially derived ATP in synaptic vesicle recycling. *J. Biol. Chem.* **290**, 22325–22336 (2015).
68. Kuner, T., Li, Y., Gee, K. R., Bonewald, L. F. & Augustine, G. J. Photolysis of a caged peptide reveals rapid action of *N*-ethylmaleimide sensitive factor before neurotransmitter release. *Proc. Natl Acad. Sci. USA* **105**, 347–352 (2008).
69. Pulido, C. & Ryan, T. A. Synaptic vesicle pools are a major hidden resting metabolic burden of nerve terminals. *Sci. Adv.* **7**, eabi9027 (2021).
70. Rossi, A. et al. Defective mitochondrial pyruvate flux affects cell bioenergetics in Alzheimer's disease-related models. *Cell Rep.* **30**, 2332–2348.e10 (2020).
71. Han, S. et al. Effect of increased IL-1β on expression of HK in Alzheimer's disease. *Int. J. Mol. Sci.* **22**, 1306 (2021).
72. Regenold, W. T. et al. Mitochondrial detachment of hexokinase 1 in mood and psychotic disorders: implications for brain energy metabolism and neurotrophic signaling. *J. Psychiatr. Res.* **46**, 95–104 (2012).
73. Shan, D. et al. Abnormal partitioning of hexokinase 1 suggests disruption of a glutamate transport protein complex in schizophrenia. *Schizophr. Res.* **154**, 1–13 (2014).
74. Chen, Z. & Zhong, C. Decoding Alzheimer's disease from perturbed cerebral glucose metabolism: implications for diagnostic and therapeutic strategies. *Prog. Neurobiol.* **108**, 21–43 (2013).
75. Huang, C. W. et al. Low glucose induced Alzheimer's disease-like biochemical changes in human induced pluripotent stem cell-derived neurons is due to dysregulated O-GlcNAcylation. *Alzheimers Dement.* **19**, 4872–4885 (2023).
76. Lauretti, E., Li, J. G., Di Meco, A. & Pratico, D. Glucose deficit triggers tau pathology and synaptic dysfunction in a tauopathy mouse model. *Transl. Psychiatry* **7**, e1020 (2017).
77. Liu, F. et al. Reduced O-GlcNAcylation links lower brain glucose metabolism and tau pathology in Alzheimer's disease. *Brain* **132**, 1820–1832 (2009).
78. Zhu, Y., Shan, X., Yuzwa, S. A. & Vocadlo, D. J. The emerging link between O-GlcNAc and Alzheimer disease. *J. Biol. Chem.* **289**, 34472–34481 (2014).
79. Lagerlöf, O. O-GlcNAc cycling in the developing, adult and geriatric brain. *J. Bioenerg. Biomembr.* **50**, 241–261 (2018).
80. Wang, A. C., Jensen, E. H., Rexach, J. E., Vinters, H. V. & Hsieh-Wilson, L. C. Loss of *O*-GlcNAc glycosylation in forebrain excitatory neurons induces neurodegeneration. *Proc. Natl Acad. Sci. USA* **113**, 15120–15125 (2016).
81. Balana, A. T. & Pratt, M. R. Mechanistic roles for altered O-GlcNAcylation in neurodegenerative disorders. *Biochem. J.* **478**, 2733–2758 (2021).
82. Brenner, S. The genetics of *Caenorhabditis elegans*. *Genetics* **77**, 71–94 (1974).
83. Ghanta, K. S. & Mello, C. C. Melting dsDNA donor molecules greatly improves precision genome editing in *Caenorhabditis elegans*. *Genetics* **216**, 643–650 (2020).
84. Glomb, O. et al. A kinesin-1 adaptor complex controls bimodal slow axonal transport of spectrin in Caenorhabditis elegans. *Dev. Cell* **58**, 1847–1863 (2023).
85. Nie, D. & Sahin, M. A genetic model to dissect the role of Tsc-mTORC1 in neuronal cultures. *Methods Mol. Biol.* **821**, 393–405 (2012).
86. Kingston, R. E., Chen, C. A. & Okayama, H. Calcium phosphate transfection. *Curr. Protoc. Immunol.* **10**, 10.13 (2001).

87. Ashrafi, G., de Juan-Sanz, J., Farrell, R. J. & Ryan, T. A. Molecular tuning of the axonal mitochondrial Ca^{2+} uniporter ensures metabolic flexibility of neurotransmission. *Neuron* **105**, 678–687.e5 (2020).
88. Djakovic, S. N., Schwarz, L. A., Barylko, B., DeMartino, G. N. & Patrick, G. N. Regulation of the proteasome by neuronal activity and calcium/calmodulin-dependent protein kinase II. *J. Biol. Chem.* **284**, 26655–26665 (2009).
89. Allison, D. F. et al. Modification of RelA by O-linked *N*-acetylglucosamine links glucose metabolism to NF-κB acetylation and transcription. *Proc. Natl Acad. Sci. USA* **109**, 16888–16893 (2012).
90. Kreppel, L. K., Blomberg, M. A. & Hart, G. W. Dynamic glycosylation of nuclear and cytosolic proteins. Cloning and characterization of a unique *O*-GlcNAc transferase with multiple tetratricopeptide repeats. *J. Biol. Chem.* **272**, 9308–9315 (1997).
91. Chung, J. Y., Steen, J. A. & Schwarz, T. L. Phosphorylation-induced motor shedding is required at mitosis for proper distribution and passive inheritance of mitochondria. *Cell Rep.* **16**, 2142–2155 (2016).
92. Chen, T. W. et al. Ultrasensitive fluorescent proteins for imaging neuronal activity. *Nature* **499**, 295–300 (2013).
93. Lobas, M. A. et al. A genetically encoded single-wavelength sensor for imaging cytosolic and cell surface ATP. *Nat. Commun.* **10**, 711 (2019).
94. Schindelin, J. et al. Fiji: an open-source platform for biological-image analysis. *Nat. Methods* **9**, 676–682 (2012).
95. Manders, E. M. M., Verbeek, F. J. & Aten, J. A. Measurement of co-localization of objects in dual-colour confocal images. *J. Microsc.* **169**, 375–382 (1993).
96. Whelan, S. A., Lane, M. D. & Hart, G. W. Regulation of the *O*-linked β-*N*-acetylglucosamine transferase by insulin signaling. *J. Biol. Chem.* **283**, 21411–21417 (2008).
97. Shevchenko, A., Wilm, M., Vorm, O. & Mann, M. Mass spectrometric sequencing of proteins silver-stained polyacrylamide gels. *Anal. Chem.* **68**, 850–858 (1996).
98. Roy, A., Kucukural, A. & Zhang, Y. I-TASSER: a unified platform for automated protein structure and function prediction. *Nat. Protoc.* **5**, 725–738 (2010).
99. Jo, S., Kim, T., Iyer, V. G. & Im, W. CHARMM-GUI: a web-based graphical user interface for CHARMM. *J. Comput. Chem.* **29**, 1859–1865 (2008).
100. Terakawa, T., Kameda, T. & Takada, S. On easy implementation of a variant of the replica exchange with solute tempering in GROMACS. *J. Comput. Chem.* **32**, 1228–1234 (2011).
101. Jurrus, E. et al. Improvements to the APBS biomolecular solvation software suite. *Protein Sci.* **27**, 112–128 (2018).
102. Huang, J. & MacKerell, A. D. Jr. CHARMM36 all-atom additive protein force field: validation based on comparison to NMR data. *J. Comput. Chem.* **34**, 2135–2145 (2013).
103. Heo, S. et al. Identification of long-lived synaptic proteins by proteomic analysis of synaptosome protein turnover. *Proc. Natl Acad. Sci. USA* **115**, E3827–E3836 (2018).
104. Armbruster, M. & Ryan, T. A. Synaptic vesicle retrieval time is a cell-wide rather than individual-synapse property. *Nat. Neurosci.* **14**, 824–826 (2011).
105. Gulcin Pekkurnaz Laboratory. Pekkurnazlab/FluxNormalyzer: FluxNormalyzer-v1.0.0. *Zenodo* https://doi.org/10.5281/zenodo.11111124 (2024).
106. Gulcin Pekkurnaz Laboratory. Pekkurnazlab/fieldstimulation-: FieldStimulation. *Zenodo* https://doi.org/10.5281/zenodo.11462692 (2024).
107. John V. Pekkurnazlab/hk1structure: HK1 structure. *Zenodo* https://doi.org/10.5281/zenodo.11462796 (2024).

Acknowledgements

We gratefully acknowledge the invaluable contributions of the Pekkurnaz laboratory members, as well as the generous sharing of key instrument resources by E. Hui. We also extend our appreciation to the technical team members of the University of California San Diego Biomolecular/Proteomics Mass Spectrometry Facility and Nikon Imaging Center for their expert assistance, and Arizona State University Research Computing for providing High Performance Computing resources. This project was made possible by the support of a grant from the National Institutes of Health (NIH) to G.P. (R35GM128823), NIH (2T32GM007240) to S.B.Y., NIH (5T32GM133351) to A.A.A., NIH to M.H. (R01NS094219), University of California San Diego TRELS fellowship to A.Z., NIH (5T32NS007220) to V.L., NIH (5T32NS007220-40) to Z.W., NIH (5T32EB009380-15) to N.M.C, the San Diego IRACDA Scholars Program (K12GM068524) to R.S., URS Ledell Family Research Scholarship for Science and Engineering to A.Z., NSF Graduate Research Fellowship (2020298734) to J.W.V and NSF (MCB-1942763) to A.S. We also acknowledge the Gordon and Betty Moore Foundation (7555.04) and the Chan Zuckerberg Initiative DAF, an advised fund of Silicon Valley Community Foundation (2020-222005) for their contributions to this project.

Author contributions

G.P. and H.W. designed the experiments, with technical contributions from H.W., R.S., M.L.M., A.Z., S.B.Y., S.Y., Z.W., N.M.C., V.L., M.J., Q.G., S.W. and A.A.A. J.W.V. and A.S. contributed structural data and performed molecular simulations, and *C. elegans* experiments were carried out by Y.W. and M.H. T.M. contributed lentiviral particle production. M.G. performed mass spectrometry experiments and analysis, and E.G. provided expert technical assistance for microscopy. H.W. and G.P. wrote the manuscript with input from all co-authors.

Competing interests

The authors declare no competing interests.

Additional information

Extended data is available for this paper at https://doi.org/10.1038/s42255-024-01121-9.

Supplementary information The online version contains supplementary material available at https://doi.org/10.1038/s42255-024-01121-9.

Correspondence and requests for materials should be addressed to Gulcin Pekkurnaz.

Peer review information *Nature Metabolism* thanks Matthew Merrins, Matthew Pratt and the other, anonymous, reviewer(s) for their contribution to the peer review of this work. Primary Handling Editor: Alfredo Giménez-Cassina, in collaboration with the *Nature Metabolism* team.

[1]Neurobiology Department, School of Biological Sciences, University of California San Diego, La Jolla, CA, USA. [2]Biodesign Institute, The School of Molecular Sciences, Arizona State University, Tempe, AZ, USA. [3]Department of Genetics and Department of Neuroscience, Yale University School of Medicine, New Haven, CT, USA. [4]Biomolecular and Proteomics Mass Spectrometry Facility, University of California San Diego, La Jolla, CA, USA. [5]Cell and Developmental Biology Department, School of Biological Sciences, University of California San Diego, La Jolla, CA, USA. [6]Department of Cell Biology, Solomon H. Snyder Department of Neuroscience, Johns Hopkins University, Baltimore, MD, USA. [7]Nikon Imaging Center, University of California San Diego, La Jolla, CA, USA. [8]Present address: Thomas Jefferson University, Philadelphia, PA, USA. [9]Present address: Neurocrine Biosciences, San Diego, CA, USA. [10]Present address: Denali Therapeutics Inc., South San Francisco, CA, USA. [11]Present address: University of Southern California, Los Angeles, CA, USA. [12]Present address: Altos Labs, San Diego, CA, USA. ✉e-mail: gpekkurnaz@ucsd.edu

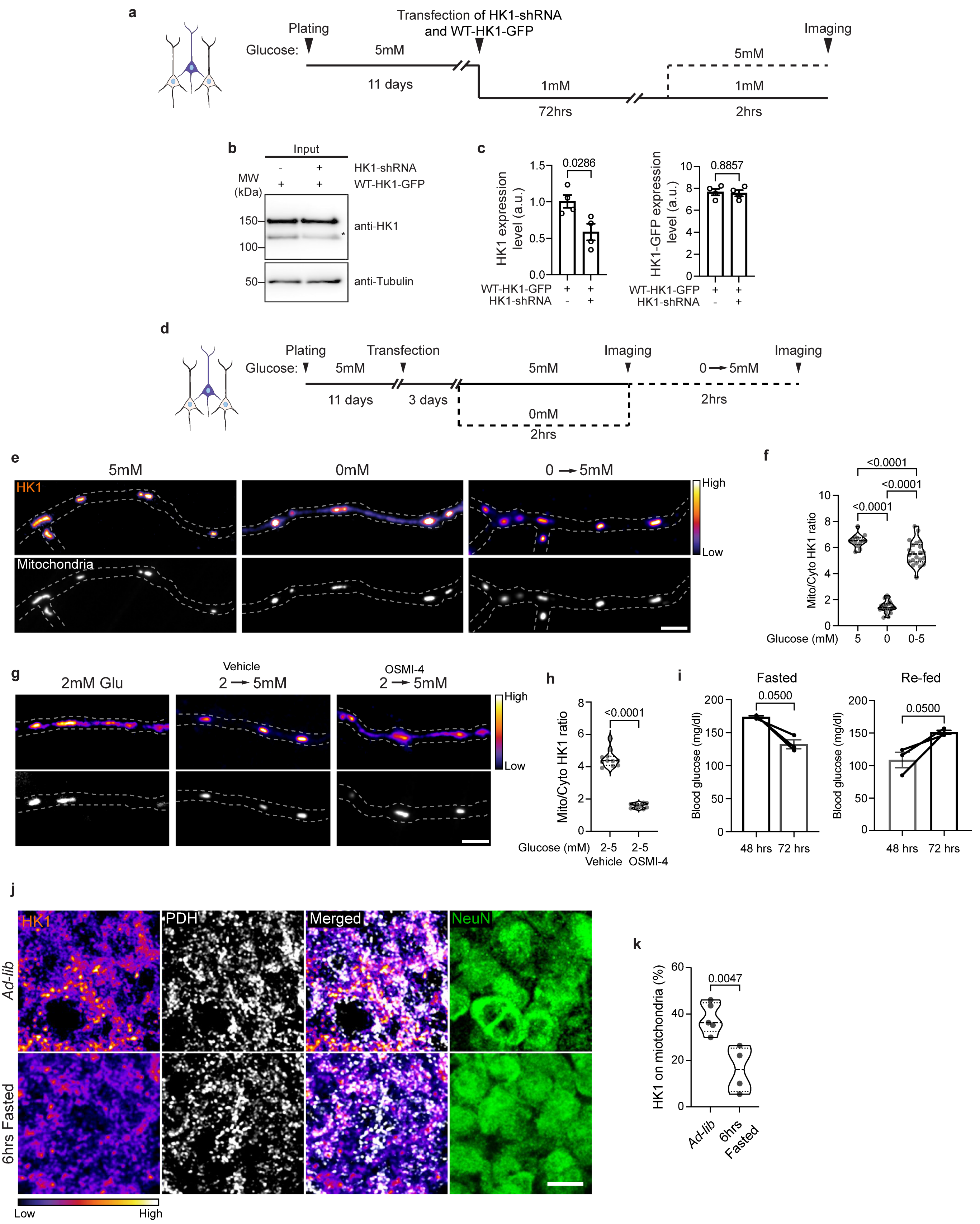

Extended Data Fig. 1 | See next page for caption.

Extended Data Fig. 1 | The mitochondrial localization of Hexokinase 1 depends on glucose metabolism. a, Experimental scheme detailing the sequence of plating, transfection, imaging, and alteration of extracellular glucose levels in cultured rat hippocampal neurons. **b**, Evaluation of HK1-shRNA knock-down efficiency in Neuro-2a cells. HK1-shRNA and shRNA resistant eGFP tagged HK1 (HK1-GFP) were expressed for 48–72 hrs, and whole cell lysate (Input) were probed with anti-HK1 and anti-Tubulin (loading control) antibodies. Asterisk indicates endogenous HK1. **c**, Quantification of endogenous HK1 (left) and eGFP-tagged HK1 (WT-HK1-GFP) (right) expression levels as shown in (**b**). All values are shown as mean ± SEM. n = 4 (two-tailed Mann-Whitney U test). **d**, Experimental scheme detailing the sequence of plating, transfection, and imaging conditions for the 0 mM glucose experiments in cultured rat hippocampal neurons. **e**, Axonal localization of HK1 in cultured rat hippocampal neurons transfected with HK1-shRNA, shRNA-resistant eGFP-tagged HK1 (pseudo-color, fire), and Mito-DsRed (gray). Representative axonal images were captured at 5 mM glucose, following a 2-hour exposure to 0 mM glucose, and at 5 mM glucose after 2 hours exposure to 0 mM glucose (1 mM lactate and pyruvate), as depicted in (**d**). Scale bar represents 5 µm. **f**, The mitochondrial (Mito) and cytoplasmic (Cyto) HK1 intensity ratios were quantified along axons. Data are presented as a violin plot with individual data points and associated p-value. n = 94–117 mitochondria, 9-10 axons from three biological replica (one-way ANOVA with post hoc Tukey's multiple comparison test). **g**, Axonal localization of HK1 in cultured rat hippocampal neurons transfected with HK1-shRNA, shRNA-resistant eGFP-tagged HK1 (pseudo-color, fire), and Mito-DsRed (gray). Representative images of axons were captured after 2 hours in 2 mM glucose, and subsequently following 2 hours in 5 mM glucose after initial exposure to 2 mM glucose. The switch from 2 mM to 5 mM glucose was performed in the presence of either vehicle or OSMI-4 treatments. Scale bar represents 5 µm. **h**, Quantification of mitochondrial (Mito) and cytoplasmic (Cyto) HK1 intensity ratios along axons. Data are presented as a violin plot with individual data points and associated p-value. n = 65–79 mitochondria, 10, 11 axons (unpaired two-tailed t-test). **i**, Blood glucose measurements from the Fasted and Re-fed mice used for comparing subcellular localization of Hexokinase 1 as shown in Fig. 1. n = 3 mice for each condition, three biological replicas. All values are shown as mean ± SEM (Mann-Whitney U test). **j**, HK1 distribution pattern in the CA3 region of the hippocampus in Ad-lib, and after 6 hours fasting (6hrs Fasted) states. Scale bar represents 10 µm. **k**, Co-localization analysis to measure the percent intensity of HK1 on mitochondria for each condition. Data are presented as violin plots with individual data points and associated p-values. n = 9 hippocampal CA3 regions, 9 mice from three biological replica (unpaired two-tailed t-test).

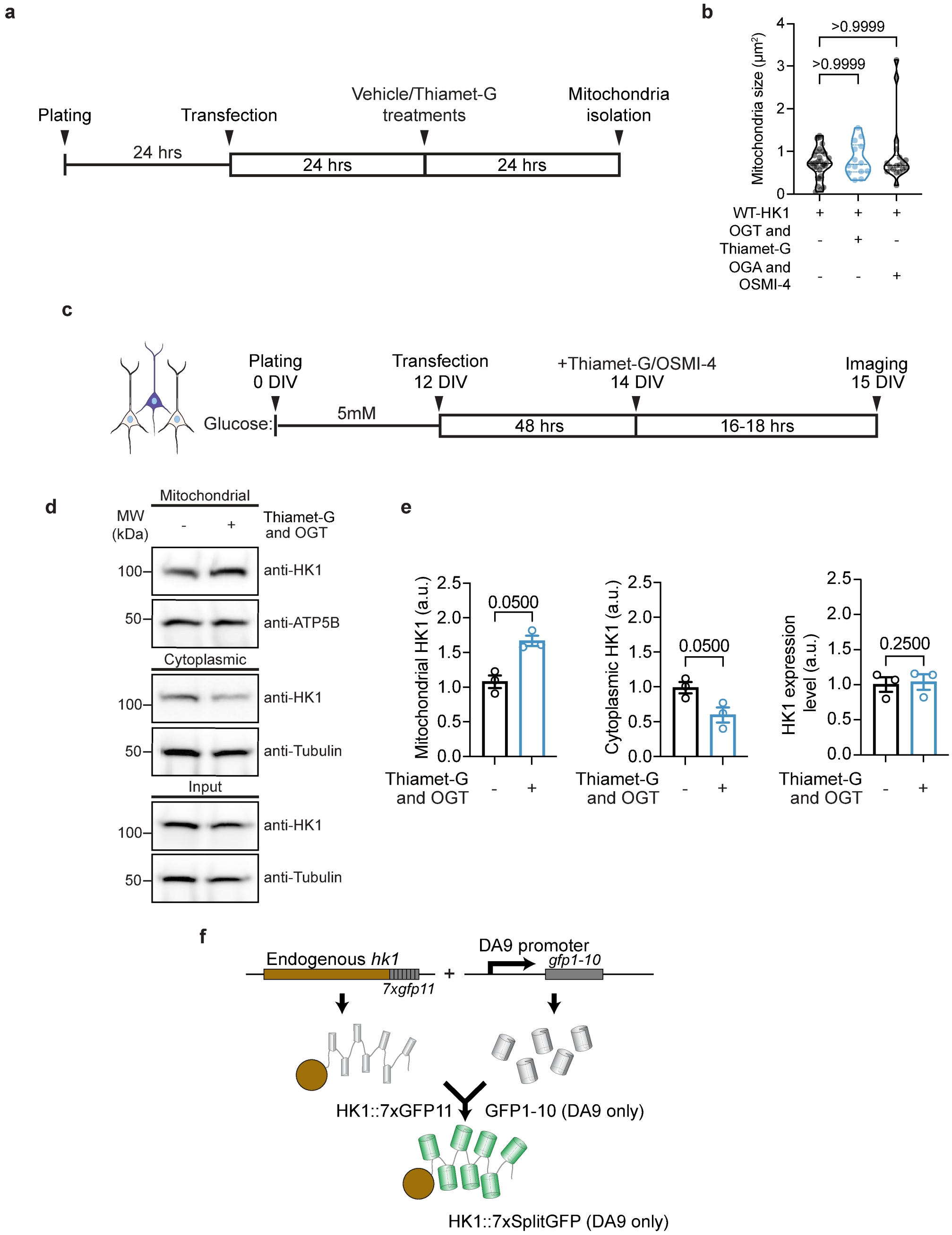

Extended Data Fig. 2 | O-GlcNAcylation promotes mitochondrial enrichment of Hexokinase 1 in various cell types. a, The experimental timeline illustrating the sequence of HEK293T cell plating, OGT transfection, administration of vehicle or Thiamet-G, and mitochondrial isolation. **b**, Analysis of mitochondrial size in cultured rat hippocampal neurons co-transfected with HK1-shRNA and eGFP-tagged HK1 to achieve endogenous HK1 levels. O-GlcNAcylation level was upregulated by ectopic OGT expression and Thiamet-G treatment, and downregulated by OGA expression and OSMI-4 treatment. Data are presented as a violin plot with individual data points and associated p-values. n = 83–120 mitochondria, 11–13 neurons, three biological replicas (one-way ANOVA with post hoc Kruskal-Wallis multiple comparison test). **c**, Experimental timeline outlining the sequence of plating, transfection, Thiamet-G and OSMI-4 treatments, and imaging of cultured rat hippocampal neurons in 5 mM glucose for experiments illustrated in Fig. 2d. **d**, Western blot analysis of whole cell lysate (Input), isolated mitochondrial and cytoplasmic fractions from HEK293T. The samples were probed with antibodies against HK1, ATP5B (mitochondrial marker), and Tubulin (cytoplasmic marker) with or without ectopic OGT expression and Thiamet-G or vehicle treatments. **e**, Quantification of HK1 levels in mitochondrial (left), cytoplasmic (middle), and whole cell lysate (right) under indicated different conditions. n = 3 (all values are shown as mean ± SEM, one-tailed Mann-Whitney U test). **f**, A schematic illustration of Native and Tissue-specific Fluorescence (NATF) method used for endogenous labeling of HK1 in *C. elegans* DA9 neuron.

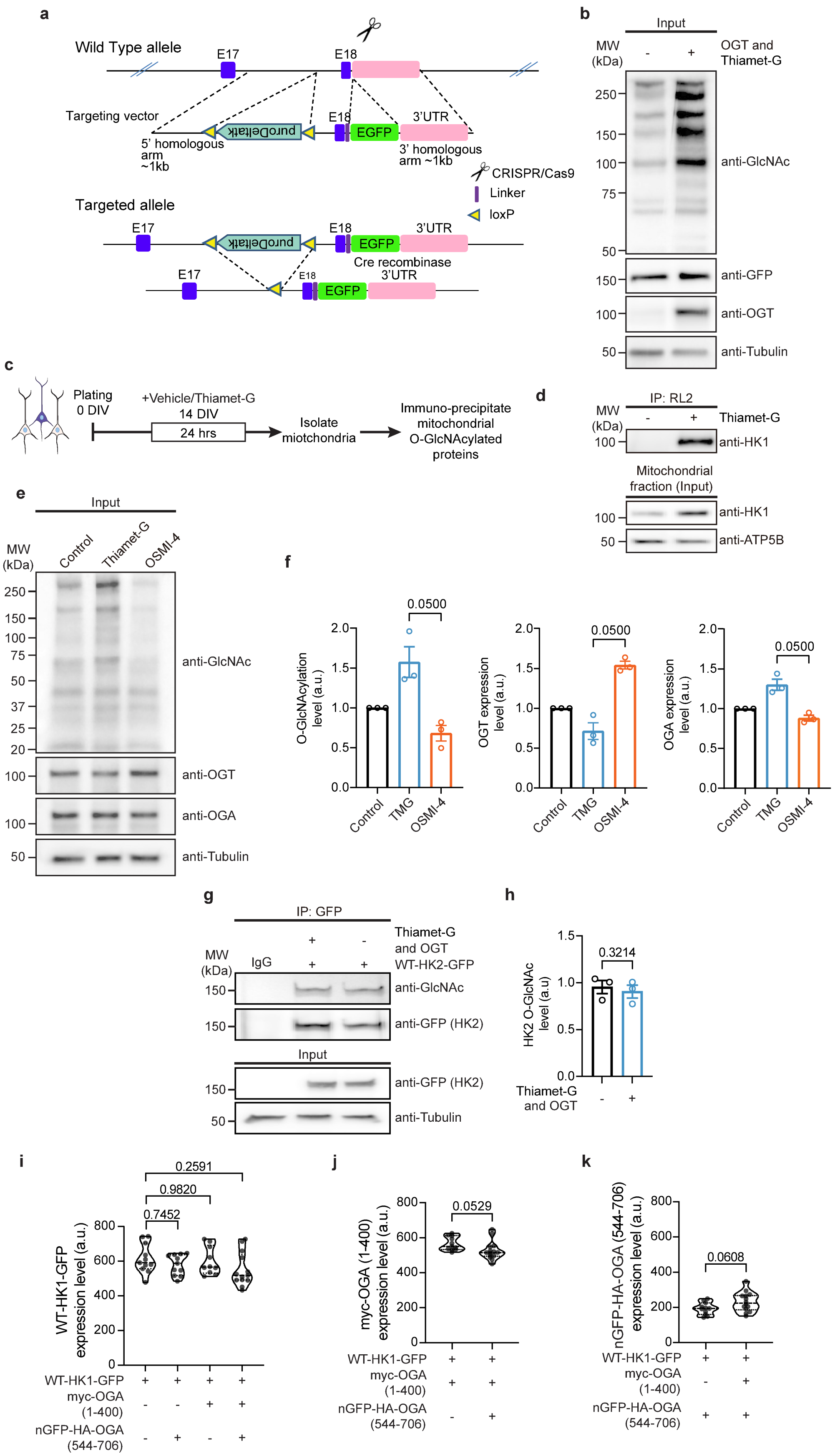

Extended Data Fig. 3 | See next page for caption.

Extended Data Fig. 3 | Elucidating the O-GlcNAc modification of Hexokinase 1 and 2. a, Illustration of CRISPR-based approach to add eGFP tag at the C-terminal of HK1 in HEK293T cells. The strategy is based on transcript-202 (NM_000188.2) and was implemented by BioCytogen. **b**, Western blot analysis of the whole cell lysate (Input), used for the generation of mitochondrial and cytoplasmic fractions as shown in Fig. 3, from HEK293T cells. The whole cell lysate (Input) from CRISPR edited HEK293T cells was probed with antibodies against O-GlcNAc (RL2), GFP (HK1), OGT and tubulin (loading control), with or without OGT overexpression and Thiamet-G treatments. **c**, Schematic demonstrating the sequence of mitochondrial isolation and O-GlcNAc immunoprecipitation (IP) using the anti-O-GlcNAc antibody RL2 from cultured rat hippocampal neurons. **d**, Western blot analysis of mitochondrial fraction (Input) and O-GlcNAc IP using antibody against HK1 and ATP5B (mitochondrial marker). **e, f**, Western blot analysis of whole cell lysate from cortical neuron cultures. The lysate was probed with antibodies against O-GlcNAc (RL2), OGT, OGA, and tubulin (as a loading control), following treatments with Thiamet-G or OSMI-4. (**f**) Quantification of O-GlcNAcylation levels, normalized to tubulin. All values are presented as mean ± SEM. n = 3 independent experiments (one-tailed Mann-Whitney U test). **g**, eGFP tagged Hexokinase 2 (HK2) was expressed in HEK293T cells. GFP antibody was used to immunoprecipitate (IP) HK2, with or without OGT overexpression and Thiamet-G treatments. The IPs were probed with anti-GlcNAc (RL2) and anti-GFP antibodies. Whole cell lysates (Input) were probed with anti-GFP and anti-tubulin antibodies. Rabbit IgG serves as an IP control. **h**, Quantification of HK2 O-GlcNAcylation levels. All values are shown as mean ± SEM, unpaired one-tailed t-test. n = 3. **i-k**, Quantification of the expression levels of HK1-GFP (**i**), myc-OGA (1–400) (**j**) and nGFP-HA-OGA (544–706) (**k**) in COS-7 cells, as shown in Fig. 3d. Data are presented as a violin plot with individual data points and associated p-value. n = 42 cells, three independent experiments (Unpaired two-tailed t-test, and one-way ANOVA with post hoc Tukey's multiple comparison test).

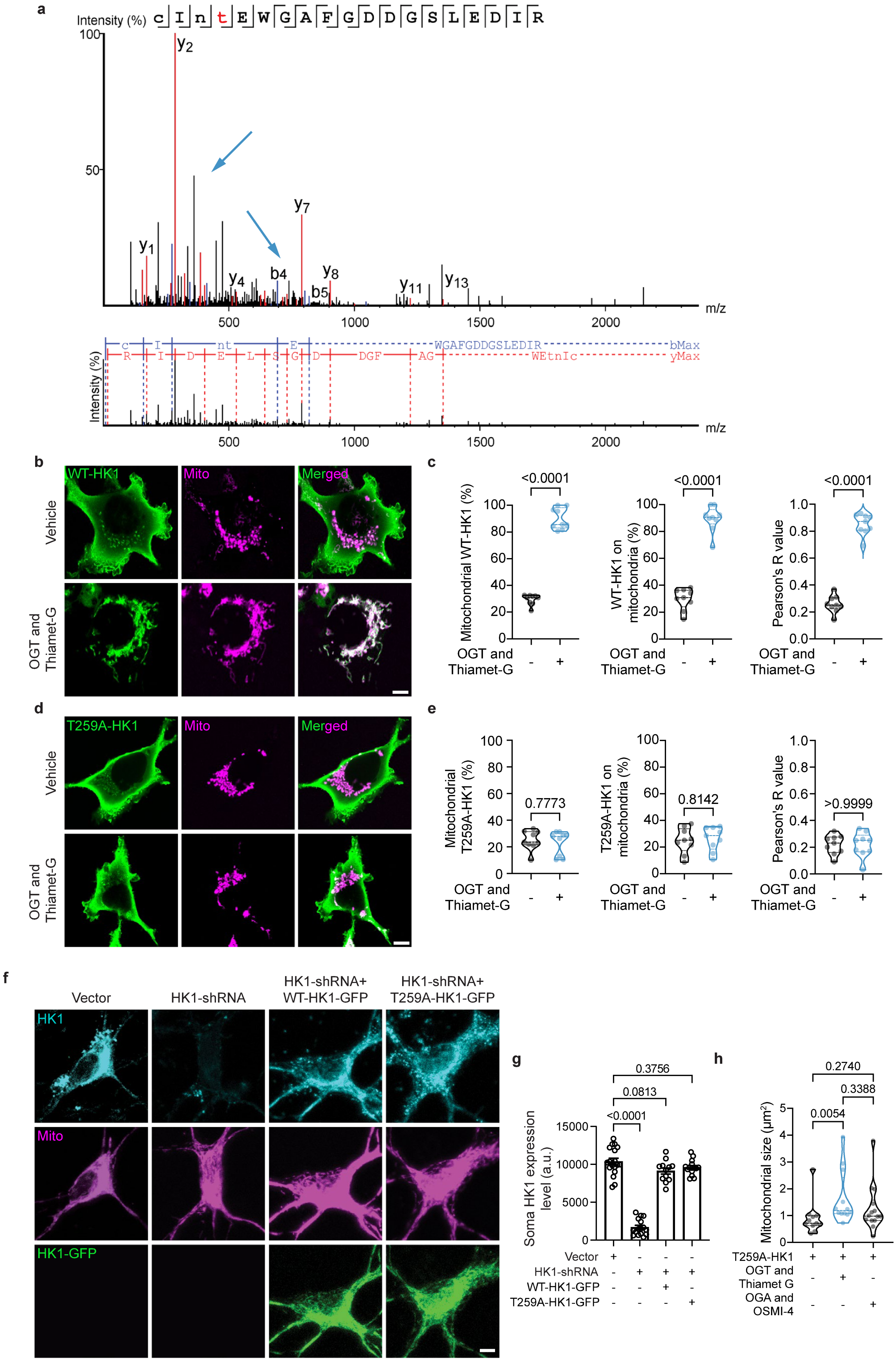

Extended Data Fig. 4 | See next page for caption.

Extended Data Fig. 4 | Identification and functional analysis of Hexokinase 1 T259 O-GlcNAcylation Site. a, Tandem mass spectra showing O-GlcNAc on peptides derived from human Hexokinase 1. Data were acquired using HCD fragmentation and prominent y and b-type ions are labeled. Blue arrow indicates the O-GlcNAc modified threonine (T). Bottom figure demonstrating the survey scan and prominent y/b-type ions. **b**–**e**, Quantitative analysis of HK1 co-localization to measure the percentage of mitochondrial HK1 intensity in HEK293T cells, cultured in 5 mM glucose containing media. (**b** and **d**) Representative images of HEK293T cells expressing WT-HK1-GFP or T259A-HK1-GFP (green) and Mito-DsRed (magenta) with or without OGT overexpression and Thiamet-G treatments. Scale bars represent 10 µm (**c** and **e**) WT and T259A HK1 intensity on mitochondria, percentage of total WT and T259A HK1 on mitochondria and the Pearson's correlation coefficient (R value) for each condition. Data are presented as violin plots with individual data points and associated p-values. n = 9 cells, three biological replicas (two-tailed Mann-Whitney U test). **f**, Representative images of hippocampal neurons expressing HK1-shRNA, WT-HK1-GFP, and the O-GlcNAc mutant T259A HK1-GFP (T259-HK1-GFP) are shown in green, along with Mito-DsRed in magenta. These images were stained with an HK1 antibody (in cyan) to visualize the total HK1 expression. Scale bar represents 5 µm. **g**, Quantification of HK1 expression levels was performed retrospectively for all experiments by analyzing the anti-HK1 staining to ensure consistent endogenous HK1 levels throughout all experiments. All values are shown as mean ± SEM (one-way ANOVA with post hoc Tukey's multiple comparison test). **h**, Quantification of the size of the mitochondria along the axons as depicted in Fig. 4g. n = 81–86 mitochondria from 10–13 axons from three biological replica (one-way ANOVA with post hoc Kruskal-Wallis multiple comparison test).

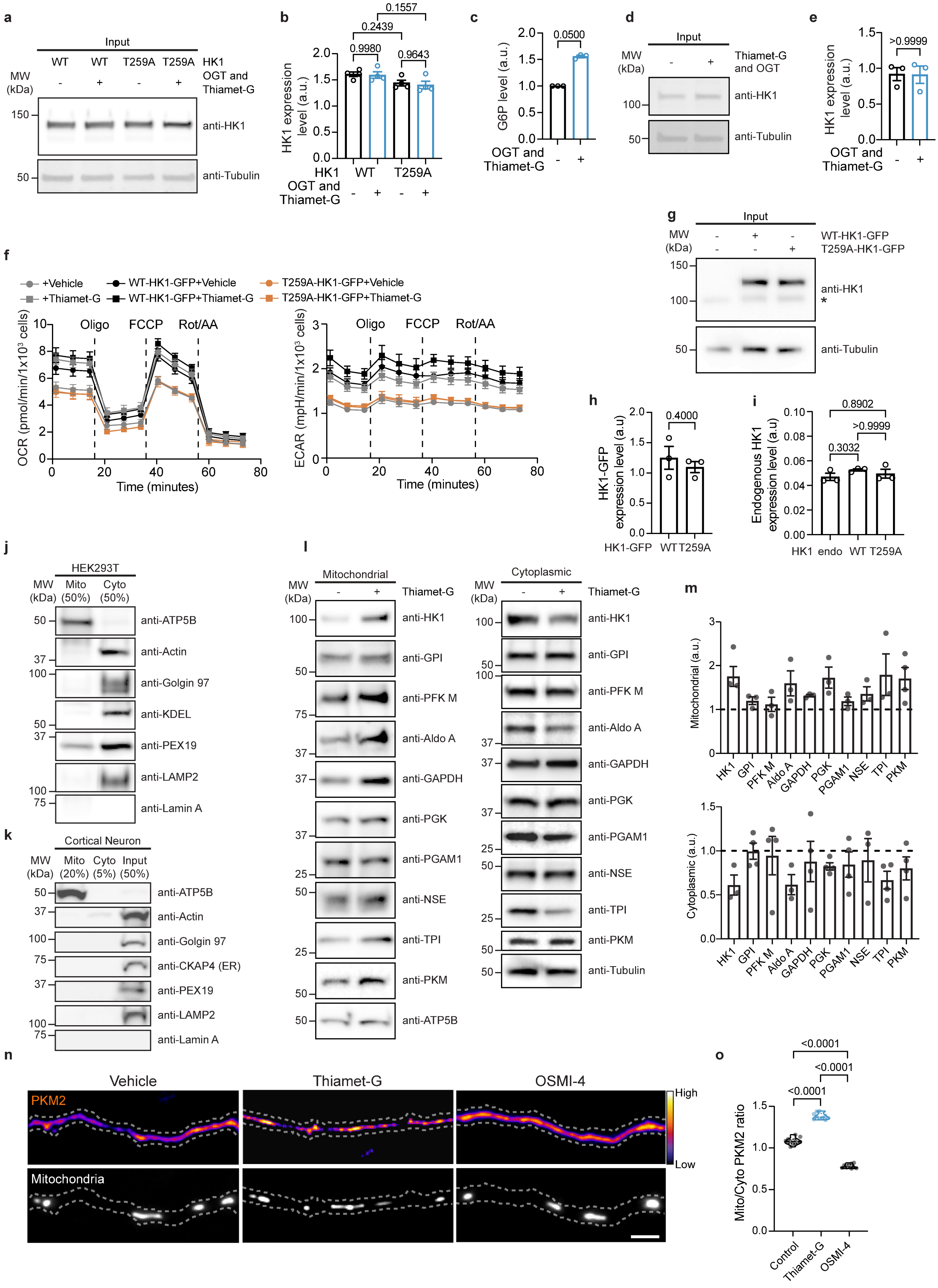

Extended Data Fig. 5 | See next page for caption.

Extended Data Fig. 5 | O-GlcNAcylation modifies Hexokinase 1 activity and contributes to the formation of mitochondrial glycolytic metabolon. **a, b**, Quantification of WT and T259A-HK1 expression levels in HEK293T cells, corresponding to the Fig. 5b. Whole cell lysates (Input) were probed with anti-HK1 and anti-tubulin (loading control) antibodies. All values are shown as mean ± SEM. n = 4 (one-way ANOVA with post hoc Tukey's multiple comparison test). **c**–**e**, Glucose-6-phosphate (G6P) levels were measured in HEK293T cells (maintaining endogenous HK1 levels) following OGT overexpression and treatment with either Thiamet-G or vehicle. G6P levels in untreated cells were set as 1, and fold changes in response to Thiamet-G treatment and OGT overexpression were calculated (mean ± SEM, one-tailed Mann-Whitney U test). (**d** and **e**) Endogenous HK1 levels were quantified from whole cell lysates (Input) using anti-HK1 and anti-tubulin (loading control) antibodies (mean ± SEM, Kruskal-Wallis test). **f**, Mitochondrial oxygen consumption rates (left) and extracellular acidification rates (right) were measured in HEK293T cells expressing control vector, eGFP-tagged WT, or T259A HK1, following treatment with either vehicle (DMSO) or overnight Thiamet-G treatment. The subsequent injections of Oligomycin (Oligo, 2 μM), FCCP (2 μM), and a combination of rotenone (Rot, 0.5 μM) and antimycin A (AA, 0.5 μM) were used to calculate ATP production rates. All values are presented as the mean ± SEM. **g**–**i**, HK1 levels in HEK293T cells used for metabolic measurements were quantified using western blot analysis of whole cell lysates, probed with antibodies against HK1 and tubulin (serving as a loading control). The asterisk indicates the presence of endogenous HK1. All values are shown as mean ± SEM. n = 3 (Mann-Whitney U test and and post hoc Kruskal-Wallis multiple comparison test). **j, k**, Western blot analysis of mitochondrial (Mito) and cytoplasmic (Cyto) fractions from HEK293T (**j**) and Cortical neurons (**k**) using antibodies against ATP5B (mitochondrial marker), Actin (cytosolic marker), Golgin 97 (Golgi Marker), KDEL and CKAP4 (endoplasmic reticulum marker), PEX19 (peroxisome marker), LAMP2 (lysosome marker) and Lamin A (nuclear marker). Input indicates whole cell lysate from Cortical neurons. Total loading amount per lane is indicated as percentage for each fraction. **l, m**, Analysis of glycolytic enzymes in mitochondrial and cytoplasmic fractions from rat cortical neurons. Mitochondrial (left) and cytoplasmic fractions (right) from rat cortical neurons, treated overnight with vehicle or Thiamet-G to upregulate O-GlcNAcylation, were analyzed for all glycolytic enzymes using the following antibodies: HK1, Glucose-6-phosphate isomerase (GPI), Phosphofructokinase muscle isoform (PFK M), Aldolase A (Aldo A), Glyceraldehyde 3-phosphate dehydrogenase (GAPDH), Phosphoglycerate kinase (PGK), Phosphoglycerate mutase 1 (PGAM1), Neuron-specific enolase (NSE), Triosephosphate isomerase (TPI), Pyruvate kinase (PKM), ATP5B (mitochondrial loading control), and Tubulin (cytoplasmic loading control) (**l**). Quantified enzyme levels under baseline conditions (**m**) were normalized to 1 (dashed line), and fold changes in response to Thiamet-G treatment were calculated. All values are shown as mean ± SEM. n = 3-4 biological replica. **n, o**, Axonal segments of hippocampal neurons cultured in 5 mM glucose, co-transfected with Mito-DsRed (gray), and human PKM2 tagged with mEGFP (pseudocolor, fire). O-GlcNAcylation level was upregulated by Thiamet-G treatment, and downregulated by OSMI-4 treatment. Scale bar represents 5 μm. (**o**) Quantification of mitochondrial (Mito) and cytoplasmic (Cyto) PKM2-mEGFP intensity ratios along axons. Data are presented as a violin plot with individual data points and associated p-values. n = 93–110 mitochondria from 9–12 axons, three biological replicas (one-way ANOVA with post hoc Tukey's multiple comparison test).

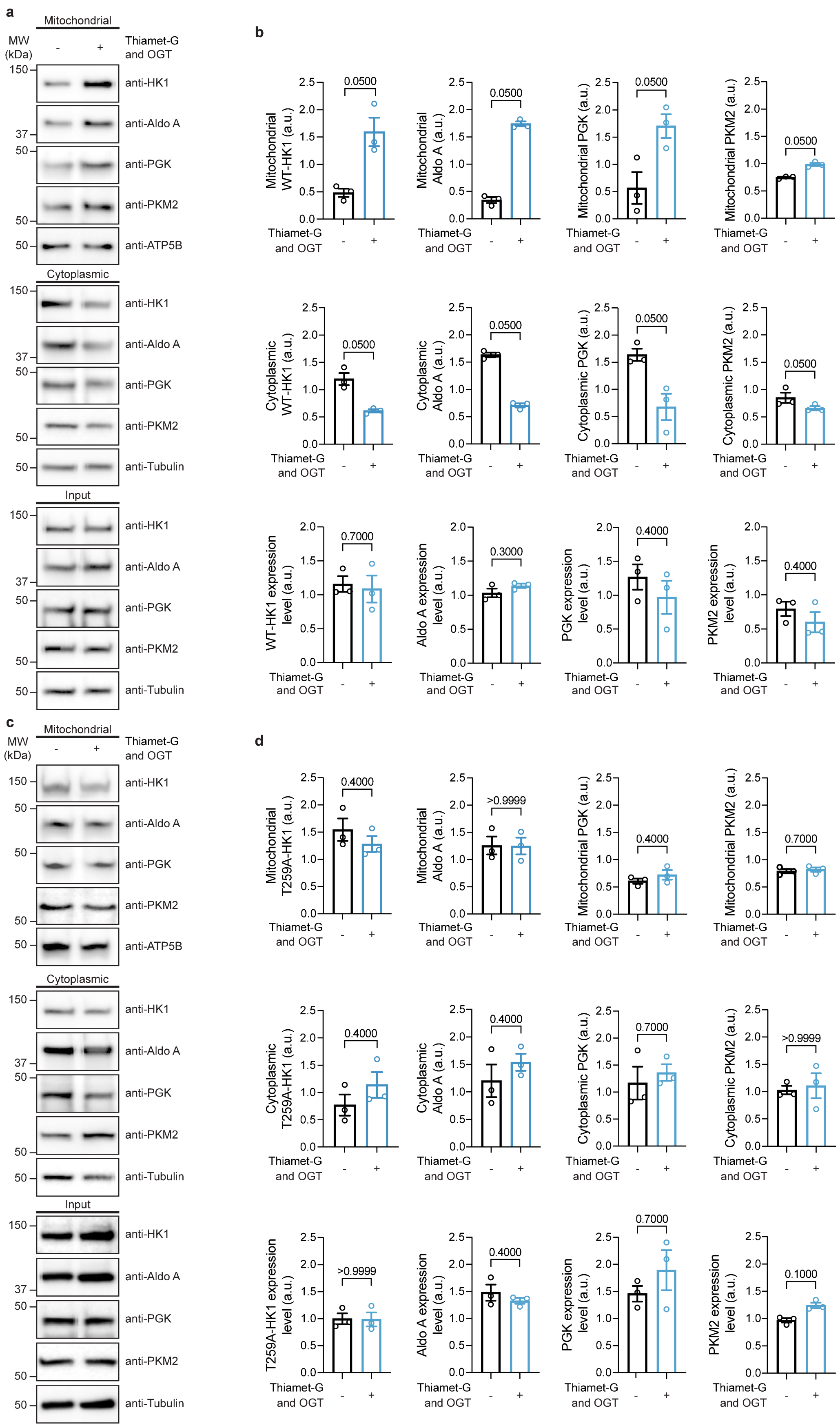

Extended Data Fig. 6 | See next page for caption.

Extended Data Fig. 6 | Hexokinase 1 O-GlcNAcylation is required for glycosome formation. a-d, Analysis of glycolytic enzymes in mitochondrial and cytoplasmic fractions from HEK293T cells expressing WT-HK1-GFP or T259-HK1-GFP. Whole cell lysates, as well as mitochondrial and cytoplasmic fractions from HEK293T cells expressing WT (**a** and **b**) and T259A HK1 (**c** and **d**) with or without ectopic OGT expression and overnight vehicle (DMSO) or Thiamet-G treatment, were analyzed to quantify the glycolytic enzyme levels. The following antibodies were used: HK1, Aldolase A (Aldo A), Phosphoglycerate kinase (PGK), Pyruvate kinase 2 (PKM2), ATP5B (mitochondrial loading control), and Tubulin (cytoplasmic loading control). Quantified enzyme levels under baseline conditions were normalized to 1, and fold changes in response to OGT overexpression and Thiamet-G treatment were calculated. All values are shown as mean ± SEM. n = 3 biological replica (one-tailed Mann-Whitney U test).

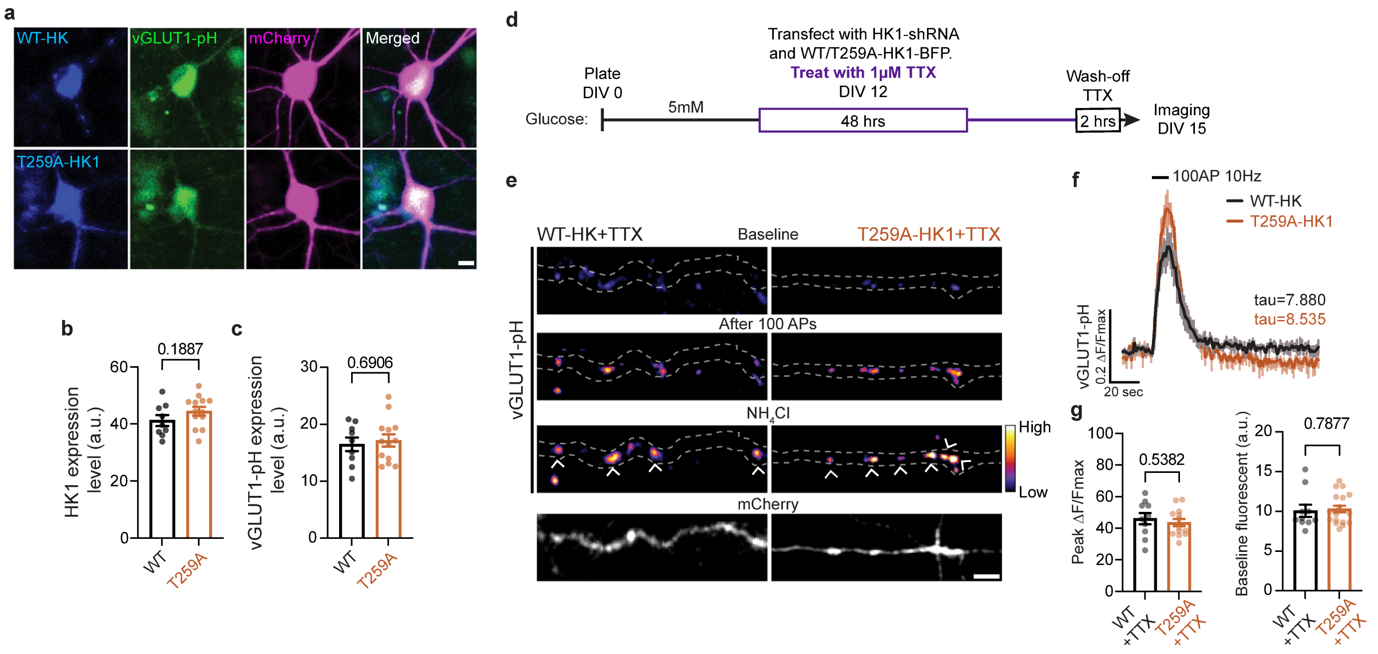

Extended Data Fig. 7 | Hexokinase 1 O-GlcNAcylation and neuronal functional measurements. a, Representative images of neuronal soma expressing shRNA-resistant BFP tagged WT or T259A-HK1 (blue) with HK1-shRNA, mCherry cell filler (magenta), and vGLUT1-pH (green). **b-c**, Retrospective quantification of WT-HK1 and T259A-HK1-BFP, and vGLUT1-pH (**c**) in rat hippocampal neurons used for imaging experiments depicted in Fig. 7. Scale bar represents 5 µm. All values are presented as mean ± SEM. n = 12–13 neurons from three biological replica (unpaired two-tailed t-test). **d-g**, The experimental design outlines the timeline for the plating, transfection, Tetrodotoxin (TTX) treatment, and imaging of cultured rat hippocampal neurons. (**e**) Hippocampal neurons were transfected with shRNA-resistant BFP-tagged WT or T259A-HK1-BFP, HK1-shRNA, and vGLUT1-pH. Following transfection, 1 µM TTX was added to neuronal culture. Two hours before imaging, TTX was washed-off as shown in (**d**). Neurons were electrically stimulated with 100 APs 10 Hz. Images showing vGLUT1-pH (pseudo-color, fire) and the cell filler mCherry (gray) before and after stimulation with WT-HK1 or T259A-HK1-BFP expressing neurons. Neutralization of vGLUT1-pH vesicles with NH4Cl reveals total axonal vesicle pool. (**f**) Average traces of vGLUT1-pH with 100 APs 10 Hz stimulation in WT-HK1 (black) or T259A-HK1 (orange) expressing neurons, previously TTX treated. ΔF values were normalized to maximal ΔF obtained from NH4Cl treatment. Error bars represent SEM. n = 8-9 neurons and 20–55 presynaptic boutons from four biological replicas. (**g**) Baseline and maximal (after electrical stimulation) vGLUT1-pH ΔF/F values. All values are shown as mean ± SEM (unpaired two-tailed t-test).

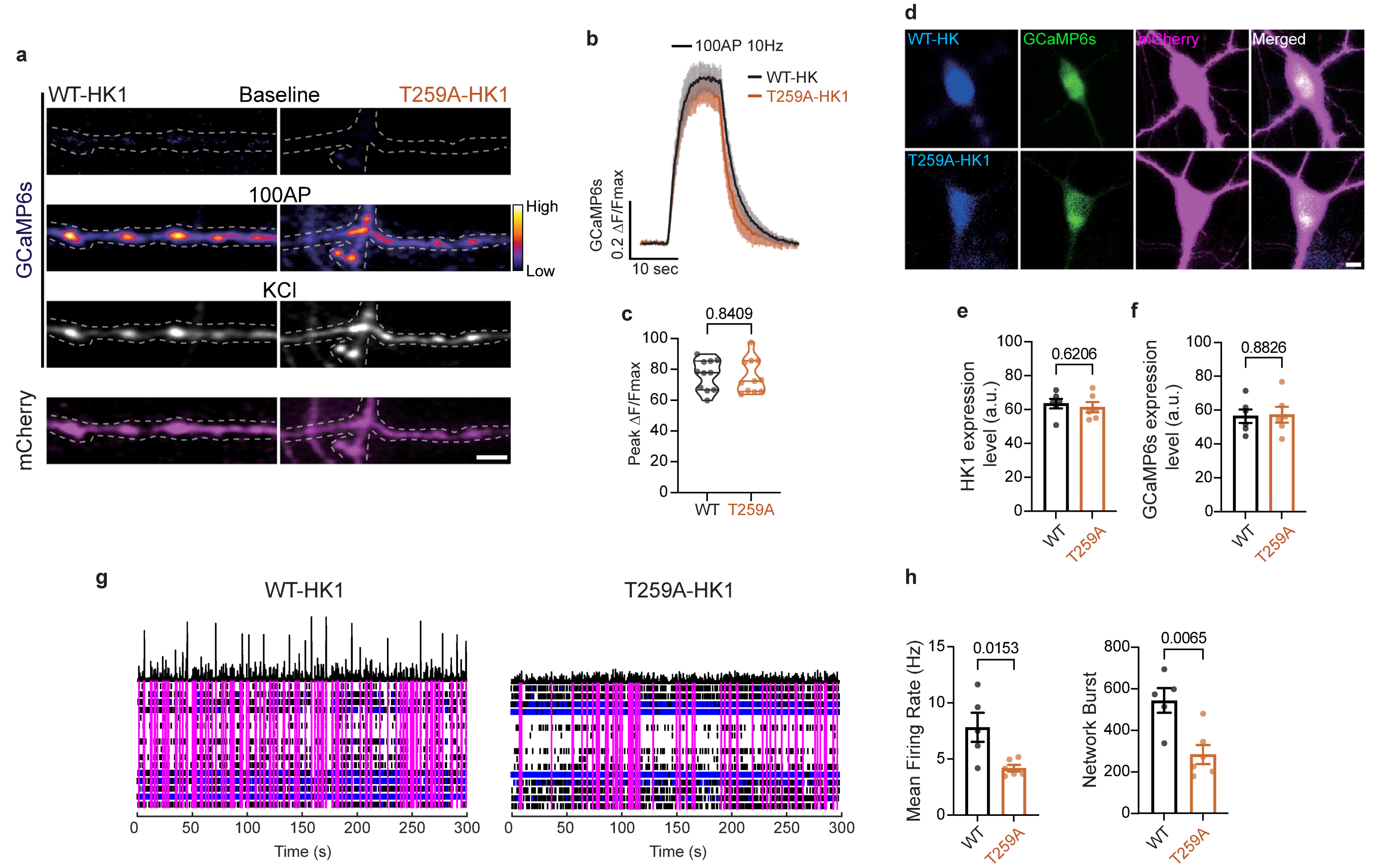

Extended Data Fig. 8 | Impact of Hexokinase 1 O-GlcNAcylation on Presynaptic Calcium Dynamics. a, Hippocampal neurons were transfected with shRNA-resistant BFP-tagged WT or T259A-HK1-BFP, HK1-shRNA, and GCaMP6s. The displayed images illustrate the GCaMP6s signal (pseudo-colored, fire) and the cell filler mCherry (magenta) prior to and following stimulation with 100 APs at 10 Hz. in neurons expressing either WT-HK1 or T259A-HK1-BFP. The peak of the Ca2+ response elicited by KCl defines the maximum GCaMP6s intensity. The scale bar represents 5 µm. **b**, The average trace of GCaMP6s during the 100 APs at 10 Hz stimulation in neurons expressing either WT-HK1 or T259A-HK1. ΔF values were normalized to the maximal ΔF observed during KCl treatment. All values are presented as mean ± SEM. n = 132 ROIs, 12 neurons from three biological replica. **c**, Maximum GCaMP6s ΔF/Fmax values. Data are presented as a violin plot with individual data points and associated p-value (unpaired two-tailed t-test). **d-f**, Retrospective quantification of WT-HK1 and T259A-HK1-BFP (blue), GCaMP6s, and mCherry cell filler (magenta) in rat hippocampal neurons used for imaging experiments depicted in (**d-f**). Scale bar represents 10 µm. All values are presented as mean ± SEM. n = 12-13 neurons from three biological replica (unpaired two-tailed t-test). **g**, Representative raster plots of demonstrating the firing patterns of rat cortical neurons (cultured on microelectrode array plates) across 64 electrodes at different time points, following transduction with lentiviral particles containing shRNA-resistant GFP-tagged WT or T259A-HK1, and HK1-shRNA. Each black line indicates a detected spike (action potentials), while blue lines represent a single-channel burst, defined as a sequence of at least five spikes with an inter-spike interval not exceeding 100 milliseconds. Each magenta line indicates coordinated bursts across the electrodes, known as network bursts. **h**, Mean firing rate (Hz) and network bursts were calculated from MEA recordings of neurons expressing WT or T259A-HK1. Data are shown as mean values ± SEM with associated p-values (unpaired two-tailed t-test), n = 5-6 MEA recordings across conditions, from two independent primary neuron preparation.

nature portfolio

Corresponding author(s): Gulcin Pekkurnaz

Last updated by author(s): Jul 10, 2024

Reporting Summary

Nature Portfolio wishes to improve the reproducibility of the work that we publish. This form provides structure for consistency and transparency in reporting. For further information on Nature Portfolio policies, see our Editorial Policies and the Editorial Policy Checklist.

Statistics

For all statistical analyses, confirm that the following items are present in the figure legend, table legend, main text, or Methods section.

n/a	Confirmed	
☐	☒	The exact sample size (*n*) for each experimental group/condition, given as a discrete number and unit of measurement
☐	☒	A statement on whether measurements were taken from distinct samples or whether the same sample was measured repeatedly
☐	☒	The statistical test(s) used AND whether they are one- or two-sided *Only common tests should be described solely by name; describe more complex techniques in the Methods section.*
☐	☒	A description of all covariates tested
☐	☒	A description of any assumptions or corrections, such as tests of normality and adjustment for multiple comparisons
☐	☒	A full description of the statistical parameters including central tendency (e.g. means) or other basic estimates (e.g. regression coefficient) AND variation (e.g. standard deviation) or associated estimates of uncertainty (e.g. confidence intervals)
☐	☒	For null hypothesis testing, the test statistic (e.g. *F*, *t*, *r*) with confidence intervals, effect sizes, degrees of freedom and *P* value noted *Give P values as exact values whenever suitable.*
☒	☐	For Bayesian analysis, information on the choice of priors and Markov chain Monte Carlo settings
☒	☐	For hierarchical and complex designs, identification of the appropriate level for tests and full reporting of outcomes
☐	☒	Estimates of effect sizes (e.g. Cohen's *d*, Pearson's *r*), indicating how they were calculated

Our web collection on statistics for biologists contains articles on many of the points above.

Software and code

Policy information about availability of computer code

Data collection	Axion Neural Metrics V4.0.5, AxIS Navigator V3.7.3.2, Peaks (version 8.5), Spark Control (version 2.1), SnapGene (version 4.1.6), details for the custom written codes are provided in the method section.
Data analysis	Fiji/ImageJ2 version 2.3.0/1.54h, Wave Desktop 2.6, GraphPad Prism version 7.0, Peaks 8.5, Byonic™ (the details are also listed in the Supplementary Table 1).

For manuscripts utilizing custom algorithms or software that are central to the research but not yet described in published literature, software must be made available to editors and reviewers. We strongly encourage code deposition in a community repository (e.g. GitHub). See the Nature Portfolio guidelines for submitting code & software for further information.

Data

Policy information about availability of data

All manuscripts must include a data availability statement. This statement should provide the following information, where applicable:

- Accession codes, unique identifiers, or web links for publicly available datasets
- A description of any restrictions on data availability
- For clinical datasets or third party data, please ensure that the statement adheres to our policy

Source data are provided with this paper. Any additional information required to reanalyze the data reported in this paper is available from the lead contact upon request.

Research involving human participants, their data, or biological material

Policy information about studies with human participants or human data. See also policy information about sex, gender (identity/presentation), and sexual orientation and race, ethnicity and racism.

Reporting on sex and gender	N/A
Reporting on race, ethnicity, or other socially relevant groupings	N/A
Population characteristics	N/A
Recruitment	N/A
Ethics oversight	N/A

Note that full information on the approval of the study protocol must also be provided in the manuscript.

Field-specific reporting

Please select the one below that is the best fit for your research. If you are not sure, read the appropriate sections before making your selection.

☒ Life sciences ☐ Behavioural & social sciences ☐ Ecological, evolutionary & environmental sciences

For a reference copy of the document with all sections, see nature.com/documents/nr-reporting-summary-flat.pdf

Life sciences study design

All studies must disclose on these points even when the disclosure is negative.

Sample size	All experiments were conducted using sample sizes consistent with standard protocols in the field. We made every effort to avoid unnecessary or excessive use of animals. No statistical tests were employed to predetermine these sizes, but instead, we based our determinations on what is commonly cited in the literature within our field as indicated in the method section. The statistical analyses were tailored to each experiment's sample size, and we found that the sample sizes used in our study provided sufficient statistical power.
Data exclusions	No data exclusions.
Replication	All experimental data were consistently reproduced in minimum three independent experiments, as detailed in the figure legends. For in vivo studies, we used three independent cohorts to guarantee reproducibility.
Randomization	Randomization was accomplished by changing the sample order for every experiment.
Blinding	Experimenters were not blinded during the sample preparation, as groups were distinguished based on treated cells and varying conditions. Data collection (i.e. image acquisition) and analysis were performed blind to the conditions of the experiments. For feeding/fasting experiment, the experimenter mounted the brain slices onto slides and was thus aware of the order. However, the experimenter was blinded during image analysis to prevent any bias in the interpretation of the results.

Reporting for specific materials, systems and methods

We require information from authors about some types of materials, experimental systems and methods used in many studies. Here, indicate whether each material, system or method listed is relevant to your study. If you are not sure if a list item applies to your research, read the appropriate section before selecting a response.

Materials & experimental systems

n/a	Involved in the study	
☐	☒	Antibodies
☐	☒	Eukaryotic cell lines
☒	☐	Palaeontology and archaeology
☐	☒	Animals and other organisms
☒	☐	Clinical data
☒	☐	Dual use research of concern
☒	☐	Plants

Methods

n/a	Involved in the study	
☒	☐	ChIP-seq
☒	☐	Flow cytometry
☒	☐	MRI-based neuroimaging

Antibodies

Antibodies used	All primary and secondary antibodies used in this study are listed in the Supplementary Table 1 with their Research Resource Identifier codes.
Validation	In this study, we used only antibodies that have been previously validated through knock-down/knock-out studies or overexpression of tagged versions. Citations are provided throughout the manuscript and are also listed alongside their associated Research Resource Identifier codes in the Supplementary Table 1.

Eukaryotic cell lines

Policy information about cell lines and Sex and Gender in Research

Cell line source(s)	HEK293T, Neuro-2a and COS7 cells were sourced from ATCC and were used only within 10-15 passages.
Authentication	Authenticated by ATCC, and by users for each passage based on cellular morphology.
Mycoplasma contamination	Mycoplasma contamination was tested every four weeks using PCR. Test results were always negative.
Commonly misidentified lines (See ICLAC register)	N/A

Animals and other research organisms

Policy information about studies involving animals; ARRIVE guidelines recommended for reporting animal research, and Sex and Gender in Research

Laboratory animals	C57BL/6J strain wild-type male and female mice , Sprague-Dawley strain wild-type rats , Caenorhabditis elegans
Wild animals	N/A
Reporting on sex	Both male and female 10-15 weeks old mice/rat were used throughout the study.
Field-collected samples	N/A
Ethics oversight	All animal experiments were conducted according to the NIH Guide for the Care and Use of Experimental Animals and approved by the University of California San Diego Animal Care and Use Committee.

Note that full information on the approval of the study protocol must also be provided in the manuscript.